FABRICATION OF CARBON NANOFIBER THIN FILM COMPOSITE MEMBRANE FOR FORWARD OSMOSIS AND PRESSURE RETARDED OSMOSIS PROCESSES WITH GLYCEROL DRAW SOLUTION

GOH EU-NICE

A project report submitted in partial fulfilment of the requirements for the award of the degree of Bachelor (Hons.) of Chemical Engineering

Lee Kong Chian Faculty of Engineering and Science
Universiti Tunku Abdul Rahman

September 2017

DECLARATION

I hereby declare that this project report is based on my original work except for citations and quotations which have been duly acknowledged. I also declare that it has not been previously and concurrently submitted for any other degree or award at UTAR or other institutions.

Signature :

Name : Goh Eu-Nice

ID No. : 12UEB02279

Date :

APPROVAL FOR SUBMISSION

I certify that this project report entitled **"FABRICATION OF CARBON NANOFIBER THIN FILM COMPOSITE MEMBRANE FOR FORWARD OSMOSIS AND PRESSURE RETARDED OSMOSIS PROCESSES WITH GLYCEROL DRAW SOLUTION"** was prepared by **GOH EU-NICE** has met the required standard for submission in partial fulfilment of the requirements for the award of Bachelor of Engineering (Hons.) Chemical Engineering at Universiti Tunku Abdul Rahman.

Approved by,

Signature :

Supervisor : Dr. Mah Shee Keat

Date :

Specially dedicated to
every single breathing soul that contributed
to the smiles I made in my life.

ACKNOWLEDGEMENTS

The completion of this project would not have been an astonishing success if it wasn't for the participation, assistance and support of many individuals.

First and foremost, I would like to express my unconditional gratitude to the university, Universiti Tunku Abdul Rahman (UTAR). Without the provision of this remarkable opportunity as a requirement for the Bachelor of Engineering (Hons) Chemical Engineering, I would not have been able to accomplish this project.

Next, I am also exceedingly grateful to be blessed with the guidance and encouragement from my supervisor, Dr. Mah Shee Keat. I have gotten endless support from him which was what motivated me to perform better in the completion of this research. I would also love to express my gratitude to Lim Su Wei for not only guiding me in the completion of the research but also being my motivation to perform beyond my own expectations.

Last but not least, I would like to express my deep sense of thanks to my family and friends for the consistent encouragement in this amazing venture. I would not have been able to make it this far without their endless love and support.

ABSTRACT

In this review, polyetherimide (PEI) TFC membranes with the incorporation of carbon nanofiber (CNF) were fabricated for the means of forward osmosis (FO) as well as its power generation capability in pressure retarded osmosis (PRO) applications. This study focuses on the effect of CNF on membrane performance. Before preparing the membrane casting solution for fabrication, the pristine CNF was functionalized to increase its dispersity and to produce a more efficient membrane. Morphology, surface chemistry, elemental analysis, thermal stability, phase structure as well as dispersion tests were conducted for the characterization of pristine CNF and functionalized CNF (f-CNF). The membranes were fabricated via phase inversion with incorporating the f-CNF powder into the membranes based on increasing loadings with the addition of a polyamide (PA) rejection layer formed on top to increase its salt rejection. The fabricated TFC membranes were characterized under two conditions; before and after the formation of the PA rejection layer. After the membrane fabrication, the performance of each membrane was tested under FO and PRO processes with deionized water as the feed solution. The membrane performance testing was conducted with a cross-flow membrane unit setup. To increase the novelty of the performance study, glycerol of different concentrations was used as the draw solution instead of the common salt water. The second parameter to this study was the concentration of glycerol draw solution. The FO processes were analysed based on its water flux whereas PRO was evaluated based on its generated power density. The findings in this review has shown that the membranes displayed a higher water flux with increasing glycerol concentration FO. The reverse solute flux of the system was also studied. TFC membrane 1.0 wt. % f-CNF loading produced the highest water flux followed by 0.1, 0.0 and 0.5 wt. %. On the other hand, the power density could not be generated in the PRO system due to the low sensitivity of the pressure gauge used in the setup. However, TFC membrane with 0.0 wt. % f-CNF showed significant potential in generating acceptable power density.

TABLE OF CONTENTS

LIST OF TABLES

LIST OF FIGURES

LIST OF SYMBOLS / ABBREVIATIONS

A	Permeability Constant
i	Van't Hoff Factor
J_w	Water Flux (LMH)
m	Mass of solution (kg)
n	Number of Solute Molecules
P	Hydraulic Pressure (Pa)
R	Gas Constant
T	Temperature (K)
V_M	Volume of Solvent (m^3)
W	Power Density (W/m^2)
σ	Reflection Coefficient
π	Osmotic Pressure
ρ	Density (kg/m^3)
ε	Membrane Volume Porosity
CNF	Carbon Nanofiber
CNT	Carbon Nanotube
CP	Concentration Polarization
DI	Deionized
ES	Electrospinning
ECP	External Concentration Polarization
EIPS	Evaporation-Induced Phase Separation
F-CNF	Functionalized Carbon Nanofiber
FO	Forward Osmosis
FTIR	Fourier Transform Infrared
GO	Graphene Oxide
ICP	Internal Concentration Polarization
IP	Interfacial Polymerization

KCl	Potassium Chloride
MD	Membrane Distillation
MF	Microfiltration
$MgCl_2$	Magnesium Chloride
MMM	Mixed Matrix Membrane
MPD	M-Phenylene Diamine
NaCl	Sodium Chloride
NF	Nanofiltration
NIPS	Non-Solvent Induced Phase Separation
NMP	N-Methyl-2-Pyrrolidinone
PA	Polyamide
PEI	Polyetherimide
PES	Polyethersulfone
PI	Phase Inversion
PRO	Pressure Retarded Osmosis
PSf	Polysulfone
PVDF	Polyvinylidene Fluoride
PVP	Polyvinylpyrrolidone
RO	Reverse Osmosis
SDS	Sodium Dodecyl Sulfate
SEM	Scanning Electron Microscopy
TFC	Thin Film Composite
TFN	Thin Film Nanocomposite
TGA	Thermogravimetric Analysis
TIPS	Thermal-Induced Phase Separation
TMC	Trimesoyl Chloride
UF	Ultrafiltration
VG	Vapour Growth
VIPS	Vapour-Induced Phase Separation
XRD	X-Ray Diffractometer

LIST OF APPENDICES

CHAPTER 1

INTRODUCTION

1.1 Background

Osmotic processes such as forward osmosis (FO) and pressure retarded osmosis (PRO) provides a very bright future to the world of renewable energy. Solar panels only work when the sun shines and wind turbines functions only when the wind blows. However, osmosis can practically be used in anywhere with rivers where fresh water meets seawater. This osmotic power could potentially work all the time; by the means of harnessing osmotic power.

To enhance the purpose of this research, in this section of the chapter, the crucial need for renewable energy and the need for the advancing technologies in our ever-developing world will be thoroughly elaborated. Aside from that, additional discussion on the biodiesel production industry will also be made to further strengthen the validity of this research.

1.1.1 The World Energy and Osmotic Power

In this rising era of technological evolution, the compelling situation of non-renewable energy depletion has brought the world to begin to consider the availability of other energy resource options. Hence, there is a demand to sought after clean and cost effective renewable energy to drive the daily lives of people around the world. Alternative energies such as solar, biomass, tidal and wind have been extensively researched and implemented globally to replace the available yet depleting non-renewable energy resources.

However, with the increase in global energy consumption each year, the need to look for a cleaner and better alternative energy option is required immediately. This phenomenon is the result of the increase in world population and development of developing countries around the world. The world population has been increasing from 4.4 billion people to 7.4 billion people from year 1980 to 2015 and it is estimated that

the world population will continue to increase from 0.2 % to 1 % for years to come (Roser and Ospina, 2017).

The energy consumptions in developing countries, such as China and India, have been increasing every year (Enerdata, 2015). The reason behind this is because these advancing countries they rely heavily on the country's industrial development to grow and expand their economy.

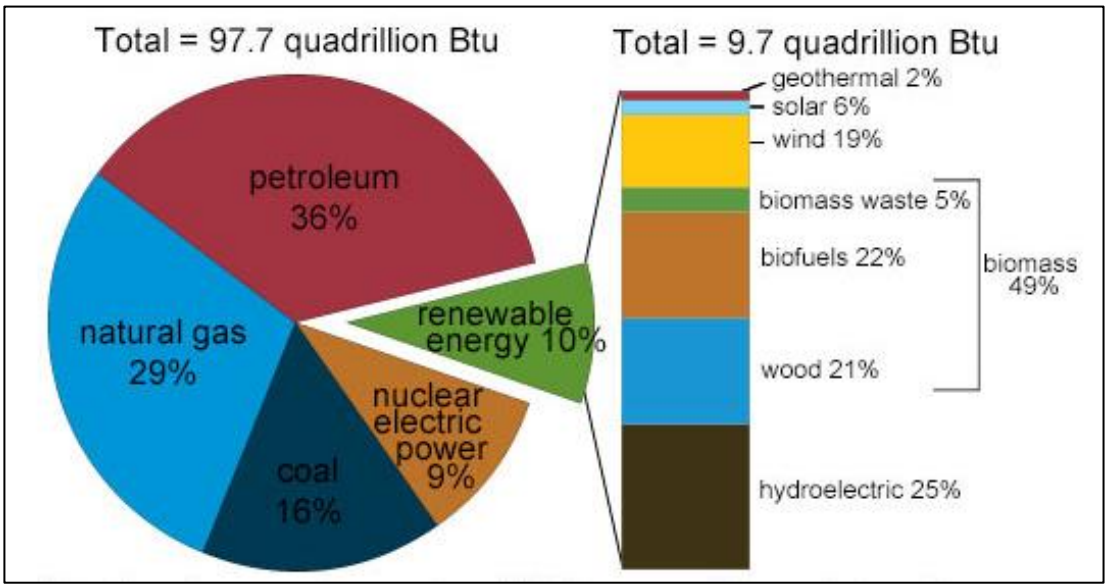

Figure 1.1: Chart of Energy Usage in the World (U.S. Energy Information Administration, 2017)

As depicted in Figure 1.1, it can be observed that we gather most of our energies from coal, oil and natural gas. These three falls under the category of fossil fuel. Additionally, we also gather energies from nuclear and renewables. Fossil fuels cost more than we pay at the pump (Wong, 2013) and it also impacts our environment in many ways. Aside from the well-known global warming problem, it also affects and deteriorates air quality, causes oil spills and even acid rains. It is also projected that fossil fuel resources will be depleted in the next 50 to 100 years (Kathryn, 2016).

Renewable energy comes from resources that replenishes by nature in our lifetime whereas fossil fuels are a one-time use in the human time scale. The upside

about renewable energy usage is that we do not need to compromise our planet to harness it, nor do we need to rely on other nations for these resources.

Due to the constraining reduction situation our planet is currently facing, people are focusing on developing and improving technology to get rid of unsustainable energies such as coal and oil. Osmotic power exploits the process of osmosis and is also termed as “blue energy” (Ball, 2015). The establishment of the world’s pioneer osmotic power plant was completed back in 2009 located in Tofte, Norway (Clark, 2013). Although osmosis is still considerably unknown to the public, it is indeed an indisputably powerful energy resource option as the others. This is because they are able to generate power no matter how the weather conditions are like (Sharif, et al., 2011).

The root way to exploit the idea of blue energy into the industry is by building osmotic power plants that uses presure retarded osmosis (PRO) technology to harness these valuable energy. These osmotic power plants are built at places where freshwater comes into contact with seawater with a semi-permeable membrane fixed in between. As the freshwater biologically migrates over to the seawater side, the water flowing through the membrane will then produce build-up pressure (Touati, et al., 2014) to drive turbines and conclusively, generate power. One of the examples of the locations to build osmotic power plants are at river run-off points (Sharif, et al., 2011).

In conclusion, the world is in desperate need of other energy resources due to the growing population fuelling the demand. With renewable energy paving the way, people can harness everything that mother nature has to offer with the added benefit of not compromising our only home. With renewable energies such as osmotic power introduced into the picture, we not only do not need to rely on other nations to harness these energies, factors like weather conditions would not influence or delay the process of reining in these energies either.

1.1.2 Biodiesel Production and Glycerol

In response to the non-renewable resources depletion situation, people all over the world are beginning to support the movement of synthesizing new ideas in order to

minimize the severity of the issue. With this, to overcome the diminishing source for fossil fuels, alternatives fuel options such as the biodiesel industry has been swiftly growing to reduce the world's dependency on petroleum (Valerio, et al., 2015).

According to the Monthly Biodiesel Production report from the United States Energy Information Administration, the consumption and production of biodiesel fuels has been gradually escalating at an annual rate of 40% per year from the year 2006 to 2012 (U.S Energy Information Administration, 2017). One of the main reason for this increment is because biodiesel is another fuel option for the world consumption and it is made entirely out of natural, renewable resources; in this case, vegetable oil and animal fats (Ayoub and Abdullah, 2011).

Aside from that, there are plentiful of other factors why the biodiesel production industry has been booming over the years. As compared to petroleum, biodiesel fuel has a lower exhaust emission as can be depicted in Figure 1.2 (Johnson and Taconi, 2007). Building on that, biodiesel also reduces pollution and minimizes environmental impacts such as global warming as well. The management and storage methods is also less harmful for biodiesel as compared to petroleum diesel fuel (Madiwale and Bhojwani, 2016).

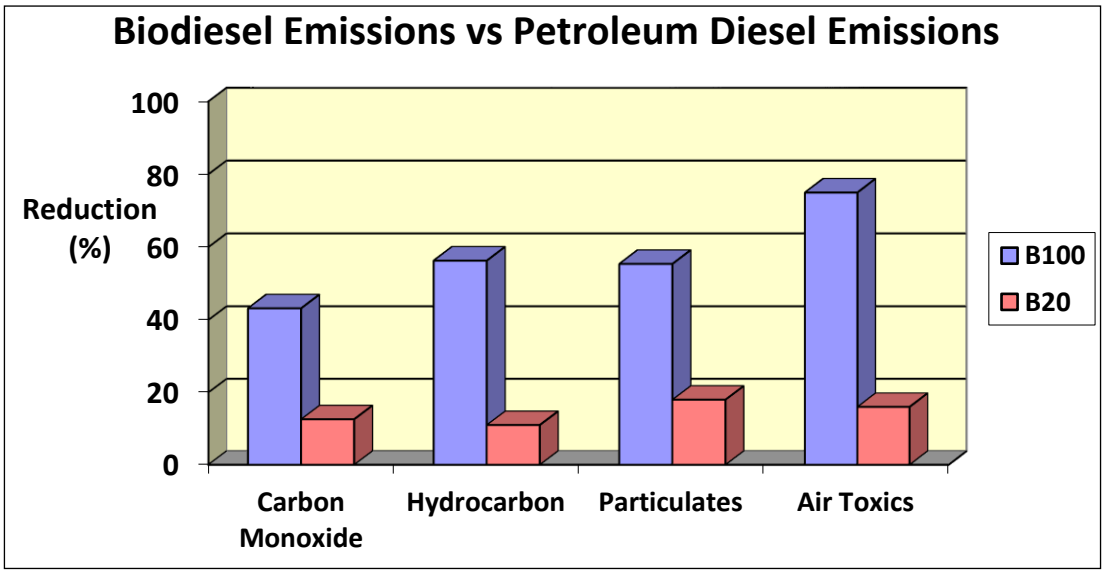

Figure 1.2: Percentage emission reduction of B100 and B20 (National Renewable Energy Laboratory (NREL), 2005)

B100 and B20 as termed in Figure 1.2 states the composition of biodiesel contained in the fuel. B100 contains 100 % natural and renewable biodiesel whereas B20 contains only 20 % biodiesel and 80 % petroleum diesel. The percentage of toxic emission each type of fuel produced is as illustrated in Figure 1.2 (U.S Energy Information Administration, 2017).

With the biodiesel production industry strengthening all around the world, the amount of co-products produced from the process will certainly surge as well. Biodiesel fuels are produced through the transesterification processes with feedstocks such as vegetable oil and animal fats. The primary by-product of the production process is crude glycerol which sums up to 10 wt. % (Cecava, et al., 2008). Hence, the major surge in construction of biodiesel production plants over the years has resulted in an extreme abundance of this glycerol by-product around the world.

The surplus of crude glycerol leads to a massive decrease in market price of pure glycerol due to the market being already too saturated. Hence, it is crucial that producers discover other possible ways to convert the abundant by-product into products that are of higher value, instead of letting it remain as a waste stream (Ayoub and Abdullah, 2011).

Today, the international crude glycerol market is still at a relatively new and developing stage; the supply and demand for glycerol is in a slump (Ayoub and Abdullah, 2011). Furthermore, glycerol has an uncommonly low economic value because of the composition of different impurities it contains such as ash, methanol and moisture (Valerio, et al., 2015). According to Patent CA 2685055 A1, the United States produces an average of 350,000 tons of crude glycerol per year throughout 2003 to 2008 (Cecava, et al., 2008). Therefore, the best solution to this dispute would be to device a proper use of the large glycerol production .

In conclusion, with the biodiesel production industry progressively increasing, large amounts of crude glycerol will continue to be formed. Relevant authorities in the industry should exercise necessary actions in order to scale down on the excessive

glycerol waste production. Other than that, producers should also source for other alternatives to turn crude glycerol into value-added products and up the opportunity of this by-product, rather than just leaving it as a liability as it is.

1.2 Problem Statement

With the world being determined to transfer all their energy production resources from non-renewable to renewable resources, it is crucial that alternatives such as osmotic power is introduced into the market. However, membranes that are built for these processes have to be of excellent properties in order to increase the efficiency of energy harnessing. Hence, thorough investigations and studies must be made in order to create the most competent and profitable membrane for various kinds applications that helps in energy generation.

Conventional osmotic power plants and most osmosis pilot plants that are built at river run-off areas where freshwater meets seawater, having seawater as a draw solution. This is so because in accordant to the U.S. Geological Survey report, seawater comprises about 70 % of the earth's surface (U.S. Geological Survey, 2017), leaving it in a large amount. However, the glycerol by-product from the biodiesel production industry was also forecasted to increase in the approaching years. This leads to a massive abundance in production of crude glycerol.

By utilizing glycerol, a major waste in the biodiesel manufacturing industry, as a draw solution and incorporating it into osmotic processes to generate power, it will enable the producers as well as the public to look at this chemical waste with value-added opportunity instead of having it be just a liability to the world. Aside from easing our planet of one of its major wastes, glycerol also possesses high osmotic pressure (Tan, et al., 2013). This added benefit leads to a higher water flux across the membrane at osmotic plants, enabling the process to harness more power and electricity (Tan, et al., 2013), (Clark, 2013).

To date, glycerol has yet to be recognized significantly as a draw solution in the osmotic power generation industry. This means that commercialized semi-permeable membranes may not work efficiently enough on this solution as compared

to seawater. Hence, alterations have to be made and distinct functions have to be added when fabricating membranes to cater specifically for the properties of glycerol. These added functions will result from the incorporation of nanoparticles into the membrane such as carbon nanofiber (CNF), carbon nanotube (CNT), zeolite and so on.

1.3 Objectives of Research

The objectives of this research are as outlined below:

1. To functionalize and characterize pristine carbon nanofibers (CNF) that will be incorporated into TFC membranes.
2. To fabricated and characterize TFC membranes incorporated with the functionalized CNF.
3. To evaluate the performance of the fabricated CNF-incorporated TFC membranes in FO and PRO in terms of water flux and power density with glycerol as the draw solution of the system.

CHAPTER 2

LITERATURE REVIEW

2.1 Introduction

In this chapter, thorough explanation and definition will be provided for every component and aspect used in this research. Aside from that, comprehensive elaboration on past researches that had been done throughout the previous years will also be made. This chapter will further define and strengthen the validity and purpose conducting this research.

2.2 Fundamental Theory of Osmosis

It was back in the mid-1700s when French scientist Jean-Antoine Nollet first set foot on the discovery journey of the osmosis process. It is a physical process that has been studied and evaluated back in the early ages of humanity. The French scientist made a massive breakthrough by validating the fact that solvents may selectively travel across a semi-permeable membrane by the means of what he called 'Natural Osmotic Pressure'. His pioneer experiments rely greatly on the osmotic membrane studies in plants and animals (Glater, 1998).

However, the rising moment of the membrane science studies and researches only occurred 200 years later, all with the main initial objective to desalinate sea water (Glater, 1998). This was the period that a substantial number of scientists begin fabricating synthetic membrane, filing patents for composite membranes as well as building osmotic plants to cater to the water purification demand. As time progresses, drastic amounts of scientific publications on processes such as Reverse Osmosis (RO), Forward Osmosis (FO) and Pressure Retarded Osmosis (PRO) began to arise. These three processes soon established themselves as the three main osmotic membrane processes.

Aside from molecular diffusion across a membrane, another thing that the three main osmotic membrane processes have in common is the general water flux formula.

The generic formula that portrays water transportation in all three of the said processes is

$$J_w = A(\sigma\Delta\pi - \Delta P) \quad (1.1)$$

where J_w is the rate of transfer of water, A is a constant for the permeability of water, σ is the reflection coefficient, $\Delta\pi$ is the difference in osmotic pressure across the membrane and ΔP is the difference in hydraulic pressure across the membrane (Baker, 2012).

The osmotic pressure is further represented by the following formula below as Equation 1.2, whereby π is the osmotic pressure, n is the number of molecules of the existing solute, V_M is the volume of the solvent, i is the Van't Hoff factor, R is the gas constant and T is the temperature (Alsvik & Hägg, 2013)

$$\pi = \frac{n}{V_M} iRT \quad (1.2)$$

With that being said, the general definition and functionality of osmosis processes is that with the help of the variation in pressure as a driving force, water will begin to maneuver itself over a selectively permeable membrane (Cath, et al., 2005). The most idealistic membrane for osmotic processes is one that efficiently grants water passage at the same time denying the flow of ions or solutes across the membrane (Touati, et al., 2014).

2.2.1 Forward Osmosis (FO)

Forward osmosis occurs naturally and appears throughout our everyday lives. For instance, this process is the reason why plants are able to draw and transport water from their roots to their shoots from the soil beneath; it is because of the difference in osmotic pressure (Baker, 2012). It is also the way how organisms such as humans and animals transport water in and out of their cells.

As mentioned previously, this process separates water from dissolved solutes by the means of a semi-permeable membrane. Since it occurs naturally, the process takes place by molecular diffusion without the requirement of any form of energy input (Cath, Childress, & Elimelech, 2005). The separation initiates with the pressure gradient created by two dissimilar solutions on opposite sides of the membrane, namely the "draw" and the "feed" solution. Under the FO condition, the draw solution should possess a higher osmotic pressure as compared to the feed solution (Alsvik and Hägg, 2013).

The mechanism of the FO is the complete inverse of the RO whereby FO initiates by osmotic pressure difference while RO initiates by the hydraulic pressure difference, causing a net movement of water molecules in the FO process to be transported from the feed side to the draw side (Cath, Childress, & Elimelech, 2005). Regarding Equation 1.1, since there is zero external pressure applied onto the system in FO as it occurs naturally, $\Delta P = 0$.

2.2.2 Pressure Retarded Osmosis (PRO)

It was back during mid-1900s when the pioneer paper publication regarding PRO by Professor Sidney Loeb was issued and invented (Helfer, et al., 2013). In his published journal article, extensive studies regarding different aspects such as technical, commerce and scientific breakthroughs of pressure retarded osmotic process was made and thoroughly discussed.

Unlike FO process which occurs naturally, PRO process happens far from habitually. According to Cath, et al., the working mechanism of PRO processes can be considered to exist somewhere between the FO and RO process mechanisms (Cath, et al., 2005), it is relatively alike to both the latter but in some way different in its own terms.

The water flux for PRO processes can also be represented by the flux formula in Equation 1.1 in Section 2.2. In the PRO process, an external hydraulic pressure, ΔP is introduced to the system and is enforced on the draw side of the membrane (Helfer, et al., 2013). However, this externally applied pressure has a maximum pressure limit

that is tantamount to the osmotic pressure of the system. This is because if the limit is exceeded, the whole process will be transformed from PRO to RO. The power density, W of PRO processes is described as the rate of total energy transferred per unit are of the membrane. It is governed by the following equation

$$W = J_w \Delta P \tag{1.3}$$

In this system, with the osmotic pressure remaining as the dominant pressure in the process, water molecules remained to be shifted from the feed to the draw solution; low to high concentration (Cath, et al., 2005). As summarized in Table 2.1, the similarities of the working mechanism of PRO as compared to FO and RO processes are as illustrated.

Table 2.1: Similarities of PRO to FO and RO

Osmotic Process	Similarities to FO	Similarities to RO
PRO	• Migration of water molecules are from the feed to the draw side of the membrane	• Presence of an applied hydraulic pressure on the draw side of the membrane

2.2.3 Comparison of FO, RO and PRO

The applications of the mentioned three main osmotic processes present in the evolving world today vary drastically from each other due to its contrasting functions each system possesses, in which will be discussed further in this chapter.

Aside from that, other properties such as membrane development and fabrication methods catering to each individual process are also immensely different from each other. Table 2.2 summarizes the similarities and differences of FO, RO and PRO based on different process characteristics.

Table 2.2: Comparison of FO, RO and PRO

Characteristics	FO	RO	PRO
Nature of process	Occurs naturally	Does not occur naturally	Does not occur naturally
Presence of external force	No	Yes	Yes
Driving force of process	Osmotic pressure $\Delta P = 0$	Hydraulic pressure $\Delta P > \Delta\pi$	Osmotic pressure $\Delta P < \Delta\pi$
Movement of molecules	From feed to draw solution	From draw to feed solution	From feed to draw solution
Illustration 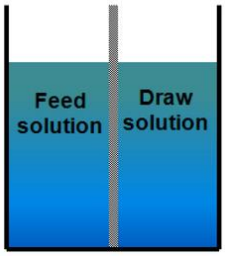 **(at equilibrium)**	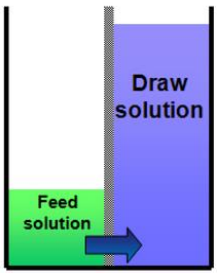	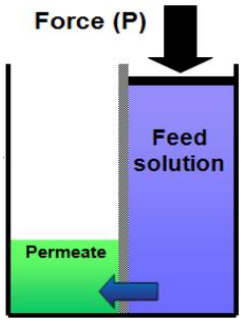	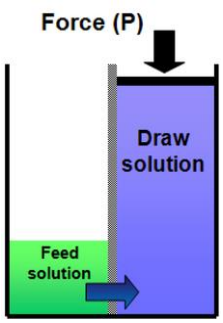

2.3 Various Osmotic Process Applications

In this current ever-evolving technological era, the various existing as well as newly discovered utilization of osmotic processes in the market have been broadening immensely throughout the years. These integrations of knowledge and technologies brings advancement to industries with some of the most common applications, namely seawater desalination, power generation, treatment of industrial wastewater, food processing as well as the pharmaceutical drug development.

2.3.1 Industrial Wastewater Treatment

With freshwater sources slowly diminishing, alternatives sources of clean drinking water have to be acquired. Aside from the conventional groundwater and seawater, wastewater is also another plausible water source. Desalination of seawater was one of the few pioneer applications to be discovered for the osmotic industry since the early 1970s (Yin and Deng, 2014). However, as time progresses, the application of FO was

also introduced as a mode of treatment for contaminated industrial wastewater to produce high quality water.

One of the few main reasons why FO was chosen as a mode of wastewater treatment is because it requires no hydraulic pressure. It also demands lesser energy input compared to RO and PRO processes (Zhao, et al., 2012). Hence, the use of FO technologies for industrial wastewater treatments sums up to a much lower cost as compared to other modes of treatment.

The treatment of wastewater through osmotic processes consists of two main steps; pre-treatment and the desalination process. FO is only taken as an intense pre-treatment process to dilute the wastewater. Further purification to the wastewater are still required to obtain clean water production (Baker, 2012). During pre-treatment, industrial wastewater is placed at the feed as it generally possesses low osmotic pressure. According to Lutchmiah, et al., during the process, clean water is extracted from the wastewater and shifted to the draw solution (Zhao, et al., 2012).

To heighten the efficiency of the pre-treatment process, suitable draw solutions with higher osmotic pressure must be selected accordingly to cater to FO (Lutchmiah, et al., 2014) and to influence the process performance. Figure 2.1 below shows some of the most common draw solutions used in FO processes (Lutchmiah, et al., 2014). Seawater or NaCl was also suggested by Cath, et al. (2005) as a suitable draw solution in wastewater treatment. This is because it is inexpensive and can be found in abundance (Cath, et al., 2005). It is also highly soluble and possesses comparatively high osmotic pressure (Lutchmiah, et al., 2014).

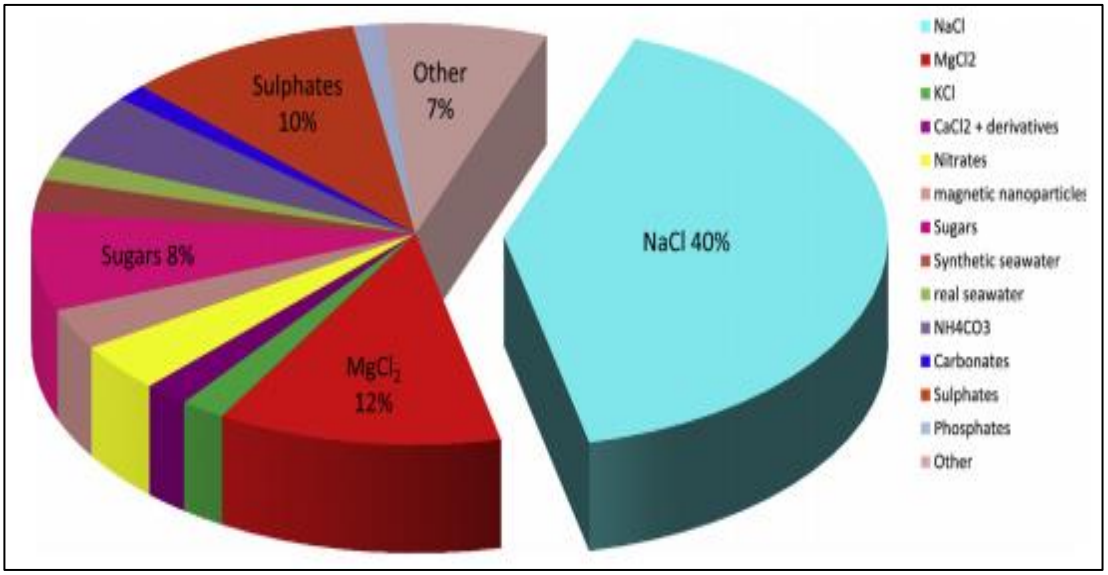

Figure 2.1: Percentage of Different Draw Solutions Used in FO as Reported by 50% of Publications Regarding FO as of 2014 (Lutchmiah, et al., 2014)

Contrasting to suggestions made by Cath, et al. (2005), other authors such as Achilli, et al. deduced that Magnesium Chloride ($MgCl_2$) would be a more suitable draw solution because the wastewater feed consists of a complex ion matrix (Lutchmiah, et al., 2014). However, the selection of $MgCl_2$ would be more costly as compared to NaCl. The pros and cons of different types of draw solution are outlined in Table 2.3 below.

Aside from draw solutions used, the antifouling property is also an important factor in obtaining an efficient FO process (Cath, et al., 2005). FO is most effective and energy efficient when the fouling property is low with permeable membranes of high rejection. Hence, membranes must also be further improved to cater to FO processes in order to achieve better wastewater treatment processes.

Table 2.3: Summary of The Advantages and Disadvantages of Various Draw Solutions Used in FO (Lutchmiah, et al., 2014)

Draw Solution	Advantages	Disadvantages	Reference
Inorganic substances **Eg. Salts**	• Inexpensive • High osmotic pressure • High solubility	• May cause clogging or fouling • Recovery may not be feasible • Salt contents may leak	Chung, et al. (2012)
Easily available sources **Eg. Seawater**	• Sources are in abundance	• Seawater are only inexpensive if process is carried out near coastal areas.	Cath, et al. (2005)
Engineered solutions **Eg. Nanoparticles**	• High osmotic pressure • No leakage • Antifouling	• Agglomeration may occur during the separation process • Water flux reduced due to viscosity of solution	Ling, et al. (2010)
Zwitterion of high solubility **Eg. Glycine**	• High flux • Low leakage	• Biodegradation of substance occurs and reduces storage time	Lutchmiah, et al. (2014)

2.3.2 Osmotic Power Generation

The rapid development of membrane technology over the years resulted to a much lower market price for producing membranes today. Hence, increasing number of researches based on incorporating osmosis technology into daily life applications including power generation through PRO.

The efficiency of PRO is dependent on the operating pressure as well as type of feed and draw solution (Touati, et al., 2014). Since are osmotic power plants usually built at river-runoff points, the feed and draw solutions are usually freshwater and seawater, respectively. The basic orientation for a continuous PRO power plant operated at steady state is as illustrated in Figure 2.2 below.

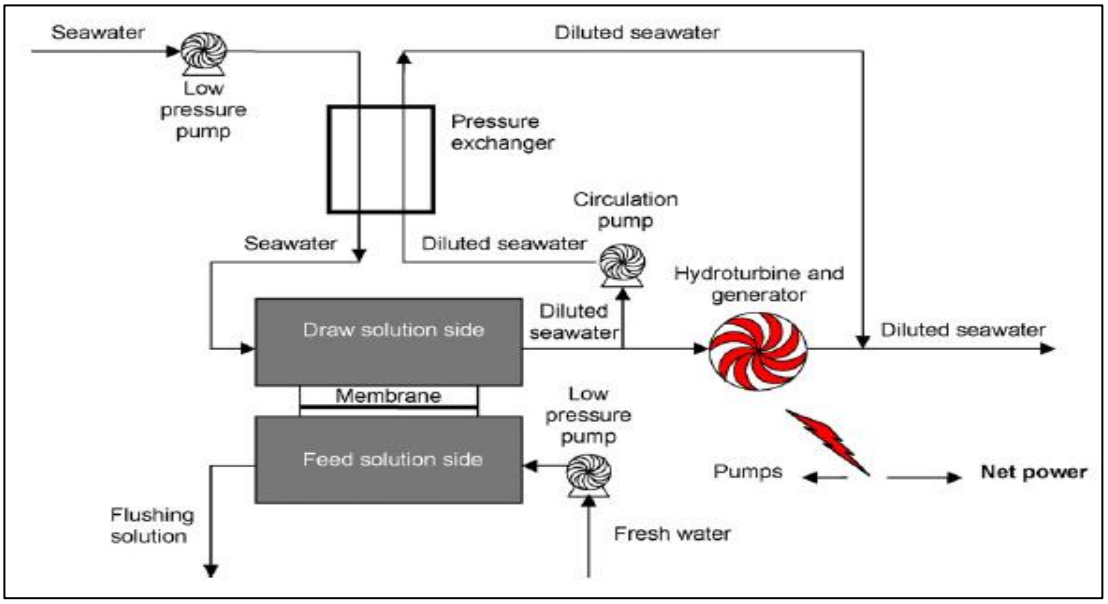

Figure 2.2: Ideal Orientation of a PRO Power Plant (Achilli, et al., 2010)

The low-pressure freshwater feed that charges through the membrane dilutes the high-pressure seawater draw and forms a new mixture named as brackish water (Han, et al., 2015). The pressurized mixture is separated into two streams: one to a circulation pump and one is fed into a hydro-turbine (Achilli, et al., 2010). The first stream enters a pressure exchanger that reduces the cost by recycling the pressure to the initial seawater draw solution. In the hydro-turbine, the stream of brackish water is depressurized and the hydraulic pressure is reduced to zero (Helfer, et al., 2013). Thus,

power is generated through the depressurizing process and obtained in the form of electricity.

2.4 Challenges in Membrane Processes

In this sub-chapter, a few of the common challenges faced by typical membrane processes are further described. The common obstacles faced in RO, FO and PRO processes are concentration polarization and membrane fouling.

2.4.1 Concentration Polarization (CP)

There are two major genre of membrane processes: the pressure driven and the osmotically driven membrane process. A common and unavoidable circumstance faced by these processes is concentration polarization (CP). CP is the occurrence of solute accumulation or reduction around the membrane interface. The occurrence of CP alters the permeate osmotic pressure that the hydraulic pressure needs to overcome, this is return also affects the water flux (Alsvik and Hägg, 2013). There are two types of CP: internal concentration polarization (ICP) and external concentration polarization (ECP).

An asymmetrical membrane consists of an active layer mounted onto a porous support layer (Cath, et al., 2005). In conventional PRO mode, the porous support faces the feed while the active zone faces the draw. This orientation is essential so the mechanical strength of the membrane is enough to sustain it from the pressurized draw solution (Zhao, et al., 2012). However, the active zone faces the feed in FO membrane as no hydraulic pressure is present.

2.4.1.1 Internal Concentration Polarization (ICP)

Internal concentration polarization (ICP) is one of the challenges faced entirely in osmotically driven membrane processes (RO & PRO). ICP is the polarization that arises within the support layer of the membrane where an abundance of solutes is either accumulated or depleted (McCutcheon & Elimelech, 2003).

There are two types of ICP, concentrative ICP and dilutive ICP. The two mentioned types take place under completely contrasting circumstance when the membrane is of different orientation, they are as depicted in Figure 2.3.

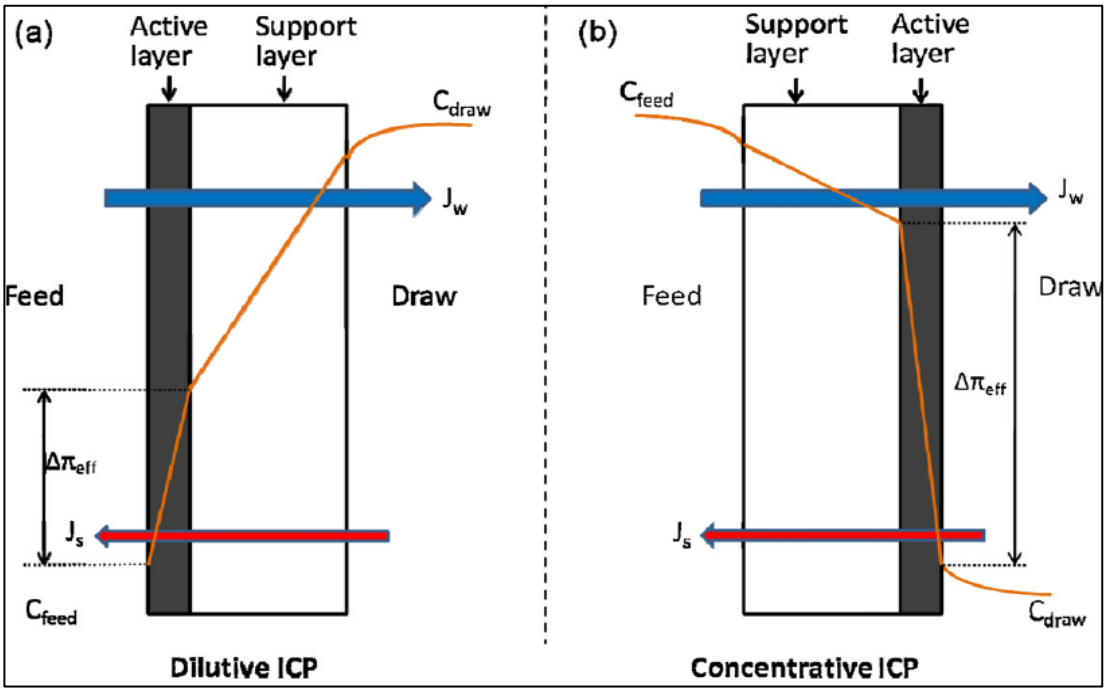

Figure 2.3: (a) Dilutive ICP and (b) Concentrative ICP (Zhao, et al., 2012)

Dilutive ICP occurs in FO mode as seen in Figure 2.3(a). This is because as the feed charges through the membrane, the draw solution within the support layer will be diluted (Zhao, et al., 2012), hence causing a drop in solute concentration and reducing the osmotic pressure (McCutcheon & Elimelech, 2003).

Contrary to dilutive ICP, concentrative ICP occurs in PRO mode as in Figure 2.3(b) (Cath, et al., 2005). As the feed enters the membrane in Figure 2.3(b), solute in the feed side gathers at the porous support layer of the membrane. The driving force reduces (Achilli, et al., 2010) as the draw solute accumulates at the interface. Since ICP is a phenomenon within the membrane support, amendments to the water flux or turbulence will not reduce the occurrence of ICP. To reduce the occurrence of ICP, the selected membranes must possess high water permeability, high porosity and have high hydrophilicity.

2.4.1.2 External Concentration Polarization (ECP)

Unlike ICP which only occurs in osmotically driven processes, external concentration polarization (ECP) can happen in both pressure-driven (RO) and osmotically driven (FO and PRO) processes (Achilli, et al., 2010). ECP is the polarization that occurs on the exterior surroundings of the membrane active layer where solutes are either accumulated or depleted.

Alike to ICP, there are also two natures of ECP: concentrative and dilutive ECP. The two mentioned types take place when the membrane is of different orientation. Concentrative ECP occurs when the active zone faces the feed where solute build up occurs on the active layer (Zhao, et al., 2012) before permeating through to the draw side of the membrane. When the dense active layer faces the draw solution, dilutive ECP occurs. This is because the feed solution charges across the membrane and dilutes the solutes of the draw solution (McCutcheon & Elimelech, 2003). Figure 2.4 illustrates the simultaneous occurrence of concentrative ICP and dilutive ECP.

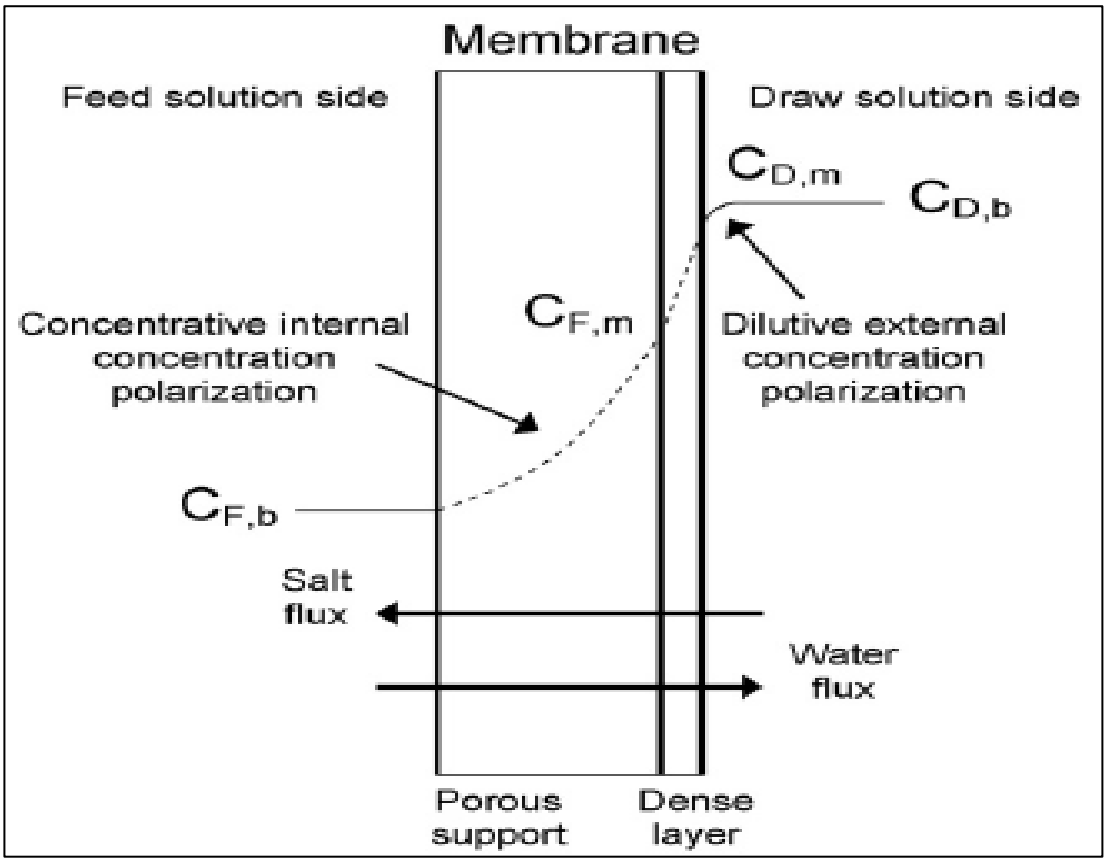

Figure 2.4: Simultaneous Occurrence of ICP and ECP (Achilli, et al., 2010)

Both natures of ECP lowers the osmotic driving force drastically. Unlike ICP, the effect of ECP on the driving force can be scaled down by raising the flow rate and turbulence at the surface of the membrane.

2.4.2 Membrane Fouling

Another infamous troublesome factor to take into consideration is the fouling of membrane. Fouling is the build-up of particles at the exterior surroundings of the membrane or within the porous membrane (Zhao, et al., 2012). Fouling greatly reduces the efficiency of a membrane by reducing the water flux as well as deteriorating the membrane material. Thus, reducing the membrane permeability (Touati, et al., 2014).

Fouling is different in both pressure and osmotically driven processes. For FO mode, fouling occurs on the smooth active layer surface of the membrane where foulants are deposited. On the other hand, during PRO mode, foulant are not only deposited on the surface of the membrane but also within the porous support (Helfer, et al., 2013). Figure 2.5 illustrates the fouling methods of FO, PRO and pressure driven process (RO).

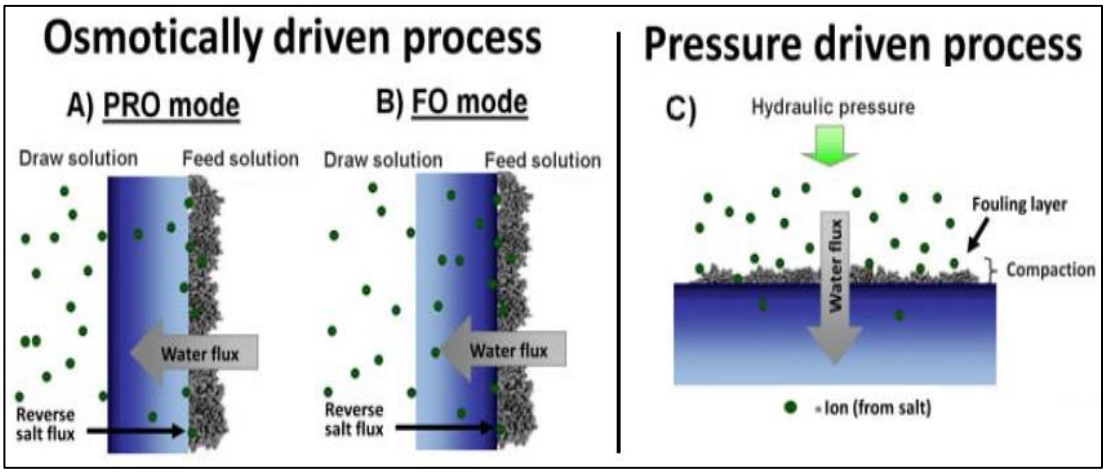

Figure 2.5: Fouling Mechanism of Membrane Processes (Alsvik and Hägg, 2013)

Fouling factors can be overcome by the strict monitoring of operating conditions, selecting suitable type of membrane materials and frequent membrane

cleaning. Aside from that, membrane surface or active layer can be modified or fabricated to cater to overcome the fouling factors (Alsvik and Hägg, 2013).

2.5 Types of Membrane

The two types of membrane discussed in this sub-chapter are thin film composite and thin film nanocomposite membrane.

2.5.1 Thin Film Composite (TFC) Membrane

Thin film composite (TFC) are made up of several layers, each with its own specific function. As shown in Figure 2.6, TFC are of asymmetric structure but with an extra fine polyamide (PA) layer structured on top of the porous membrane support. It Is usually fabricated through the process of polymerizing two monomers; trimesoyl chloride (TMC) and m-phenylene diamine (MPD) (Ismail, et al., 2015). TFCs are also classified as RO or nanofiltration (NF) membranes by many researches such as Lau, et al. (2011) and Torres, et al. (2016). TFC RO membranes are mostly utilized by the water desalination and purification industry.

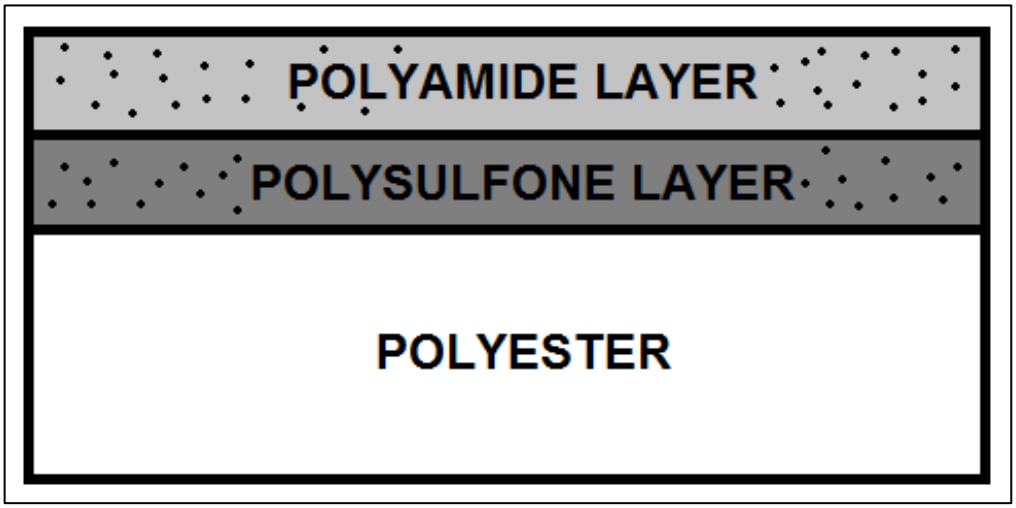

Figure 2.6: Structure of TFC Membrane

The thin rejection layer, also known as the polyamide (PA) layer is usually build on top of the porous support made from either polysulfone (PSf) or polyethersulfone (PES) on top of a support sheet. Regardless of what polymer it's made out of, the two layers formed below the top rejection layer is commonly known as the substrate layer. The newly introduced PA layer assists in increasing solute

rejection as it absolutely permeable to water (Ismail, et al., 2015) as well as possess high mechanical strength. As compared to conventional asymmetric membranes, TFCs have better selectivity as well as consumes lower amount of energy. However, according to Lau, et al. (2011), membrane performance may deteriorate and loses its function when the PA layer in commercial TFCs meet chlorine.

2.5.2 Thin Film Nanocomposite (TFN) Membrane

Alike to TFCs, thin film nanocomposites (TFN) are also manufactured by interfacial polymerization and has a structure as shown in Figure 2.6. However, contrasting to composite membranes, nanocomposite membranes contain additional incorporation of nanomaterials inside the thin PA layer of the membrane. The purpose of the added nanoparticles is to improve the functionality and performance of the TFC membrane (Lind, et al., 2009). TFN is still relatively new as compared to TFC that has been around since the later 1950s (Lau, et al., 2015).

Over the years, many researches have done several comprehensive studies on merging nanoparticles into the rejection layers of composite membranes. As in the experimental research done by Jeong, et al. (2007) when zeolite nanoparticles were incorporated into the PA active layer, the water flux was greatly enhanced without disturpting the chlorine rejection rate. Table 2.4 below depicts how the type and loading of zeolite nanoparticles incorporated into the membrane deeply affects the change in water flux in TFN and TFC. According to Lind, et al. (2009), as the size of nanoparticles decreases, the water flux increases. However, as the size of zeolite nanoparticles increases (~300 nm), the PA surface will be exposed to nanofillers (Lau, et al., 2015).

Table 2.4: Comparison of Water Flux for TFC and TFN of Different Nanoparticle Loadings

Membranes		Zeolite Loading (w/v%)	Water flux (10^{-12} m $Pa^{-1}s^{-1}$)	Reference
TFC		-	2.1	
TFN	**Type A**	0.004	~2.1	Jeong, et al., (2007)
	Type B	0.01	2.5	
	Type C	0.1	~3.2	
	Type D	0.4	3.8	

2.6 Types of Nanoparticles

Nanoparticles are often incorporated into the membrane matrix as a form a reinforcement as well as increasing the mechanical properties of the membrane. These common nanoparticles are carbon nanofiber (CNF), carbon nanotubes (CNT), graphene oxide (GO), zeolite and many more. However, only the CNF will be discussed in this sub-chapter. The incorporation of nanoparticles into TFC membranes greatly enhances the water flux, water permeability, membrane performance as well as membrane hydrophilicity (Achilli, et al., 2010).

2.6.1 Carbon Nanofiber (CNF)

Carbon nanofibers (CNF) are often advantageous in many areas of studies; in the matter of this project, CNF plays an important role as a mode of reinforcement for polymer composites. The introduction of CNF as a form of reinforcement in composites has been vaguely discovered back in 1980 (Poveda & Gupta, 2016).

CNF differ drastically from regular carbon fibers in terms of various means such as structure, size and applications. The sizes of traditional carbon fibers range within a couple micrometers whereas its nanoparticle ranges from 40 to 200 nanometers (Feng , et al., 2014). The structures of the common CNFs are as shown in Figure 2.7.

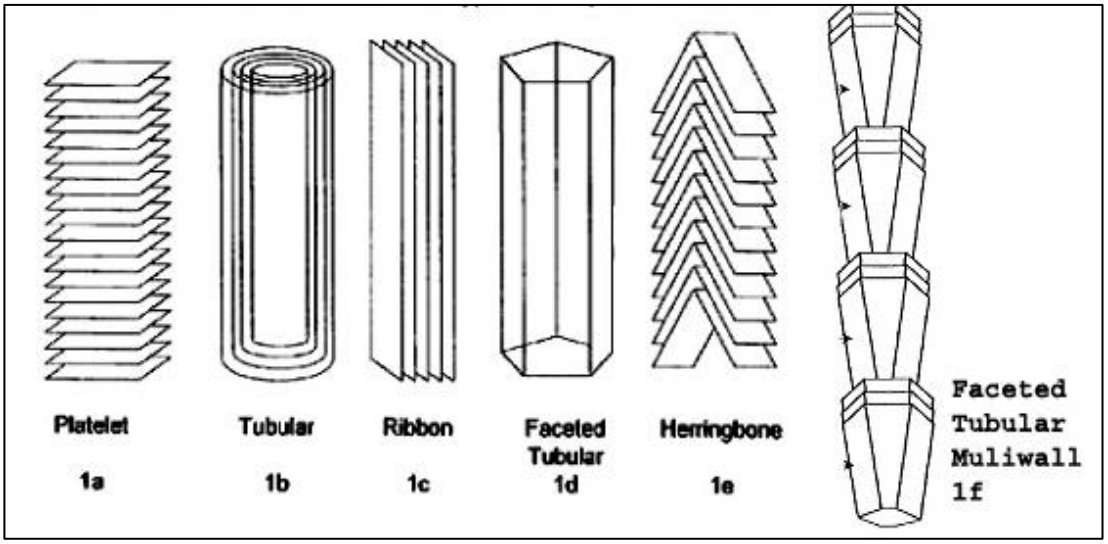

Figure 2.7: Structure of Different Types of CNF (Terry, et al., 2009)

That being said, one of the few factors that heavily affect the mechanical performance of the said nanoparticle is the structure and arrangement of the carbon fibers (Poveda & Gupta, 2016). One of the most frequently employed structures of CNFs is the 'cup-stacked' structure as shown in Figure 2.8. Concurrently, the structure of CNF is greatly dependent on its fabrication process. Hence, the mechanical performance of CNFs is affected by the way of which it is formed (Konios, et al., 2014).

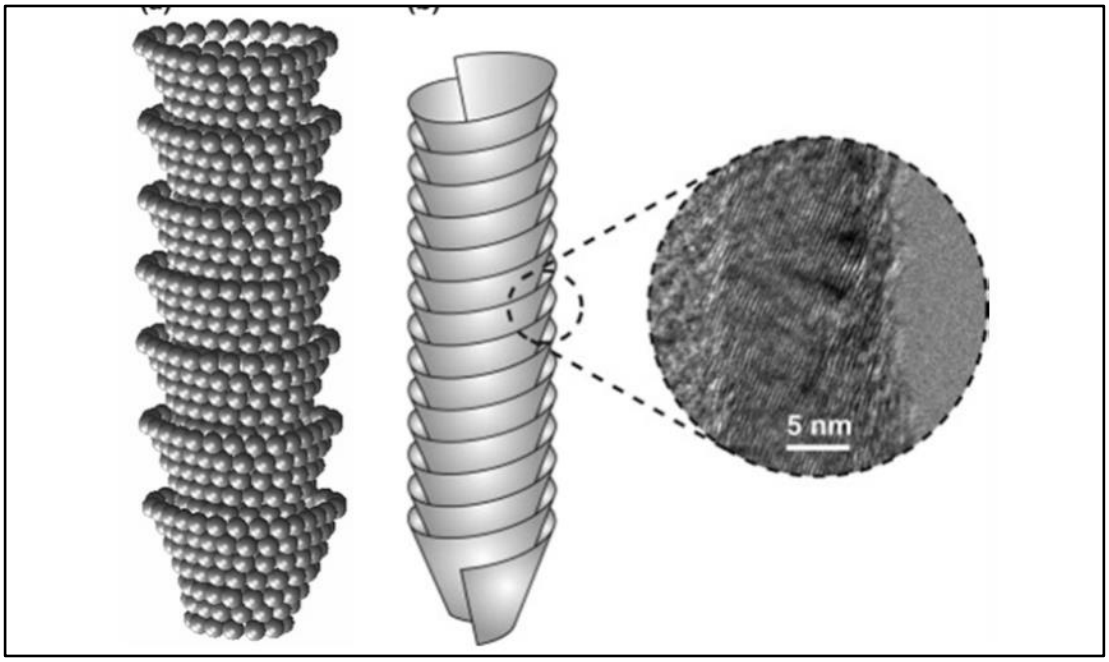

Figure 2.8: Cup-Stacked Structure of CNF (Poveda & Gupta, 2016)

CNFs usually fabricated and formed by vapour growth (VG) or electrospinning (ES) (Feng , et al., 2014). The VG fabrication method normally produces cup-stacked CNFs while the ES fabrication method produces shell-like CNF structures. The mechanical properties obtained by researches for CNFs of different fabrication methods are listed in Table 2.5.

Table 2.5: Measured Strength and Modulus of CNF (Poveda & Gupta, 2016)

Researcher	Processing Method	CNF Diameter (nm)	Strength (GPa)	Modulus (GPa)
Endo, et al. 2001	VG	300 - 1000	2.25 - 3	100 - 300
Ozkan, et al. 2010	VG	150	2.4 - 2.9	180 - 250
Zhou, et al. 2010	ES	300	0.6 - 1.0	N/A
Arshad, et al. 2011	ES	150 - 500	1.85 - 3.50	80 - 190

Whether or not CNF performs well in polymer composites depends greatly on its ability to disperse in the polymer matrix (Dabaghian & Rahimpour, 2015). With that being said, self-improvement of CNF plays a major role in increasing its mechanical properties. Hence, to produce CNF-composites with high mechanical characteristics, it is important that CNFs are well dispersed in the polymer matrix before they are manufactured. Sonication and acid-modification are two of the many ways of increasing the dispersion ability of CNFs (Feng , et al., 2014).

The acid-modification/functionalization process, also known as carboxylation, is an oxidation treatment of CNF by bathing the nanoparticles in a mixture of sulphuric and nitric acid (Liu & Kim, 2011). This enables suitable hydrophilic functional groups COOH group to be attached on the nanoparticle surface, as shown in Figure 2.9, increasing its hydrophilicity and dispersity in water. Hence, as the polymer and functionalized CNF are more chemically compatible (Zhou, et al., 2010), this enables it to have a better dispersion in the polymer matrices (Arshad, et al., 2011).

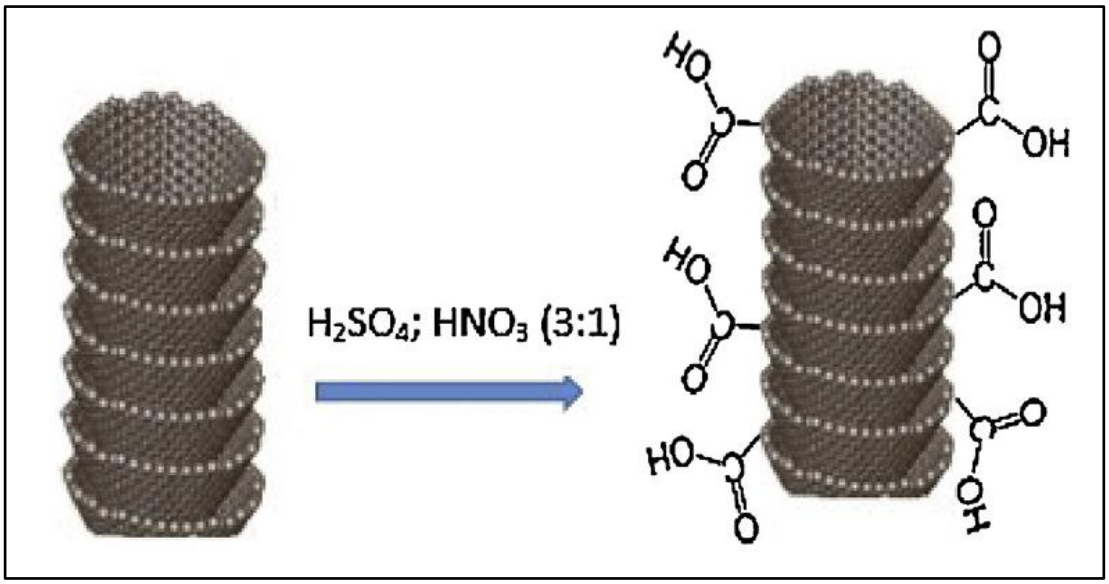

Figure 2.9: Structure of CNF Before and After Carboxylation/Functionalization

The performance of the nanoparticle-reinforced polymer increases with rising CNF loading. In a journal authored by Bortz, et al. (2010), with a CNF loading of 0.5 to 1.0 wt. %, the polymeric composite was able to withstand fracture 65% to 78% better. However, the mechanical properties will slowly deteriorate at much higher nanoparticle loading, mainly due to the serious agglomeration of the nanoparticles (Zhou, et al., 2010). The mechanical performance of CNF-incorporated composites is highly dependent on the ratio, the loading amount, the CNF-dispersion in the polymer matrix and improvement of CNF itself.

Also proven by Dabaghian and Rahimpour (2015), the osmosis water flux across a membrane will tend to increase as the nanoparticle loading increases. However, this statement is only valid until a certain optimum loading point whereby the water flux and performance will begin to decrease as agglomeration of the nanoparticle will tend to occur. The agglomeration of the fibers will cause a decrease in membrane performance, this phenomenon can be pictured with the aid instruments such as Scanning Electro Microscope (SEM).

2.7 Casting Methods of Membrane

The various membrane fabrication methods were invented to cater to design membranes for all sorts of water treatment processes at varying pore sizes such as RO,

NF, microfiltration (MF), ultrafiltration (UF) and membrane distillation (MD). The fabrication methods of the desired membranes differ based on different polymeric materials as well as membrane structure.

2.7.1 Phase Inversion (PI)

Phase inversion (PI) is the technique of transforming liquid homogeneous polymeric solutions into solid. There are four modes of phase inversion: immersion precipitation (non-solvent induced phase separation), evaporation-induced phase separation, vapour-induced phase separation and thermally-induced phase separation. Table 2.6 summarizes the descriptions of these processes.

Table 2.6: Description of PI casting method

Phase Inversion (PI)	Description	Reference
Immersion Precipitation Non-solvent-Induced Phase Separation (NIPS)	• Submerge support casted with polymer solution into non-solvent bath for coagulation • Precipitate form due to exchanging of solvent from polymer solution to the non-solvent • More concentrated the polymer, the less porous and smaller the pore size • Higher solubility between the polymer and non-solvent, the higher the porosity. • Suitable for RO, MD, UF and NF	• Liu & Kim, 2011 • Lalia, et al., 2013 • Jung, et al., 2016
Evaporation-Induced Phase Separation (EIPS)	• Polymer dissolved in a solvent and non-solvent mixture, casted on a flat support • More volatile solvents evaporate first, non-solvent precipitate on the surface of support • Suitable for NF and RO	• Lalia, et al., 2013
Vapour-Induced Phase Separation (VIPS)	• Casted polymer-solvent mixture placed in the presence of vapour solvent and non-solvent • Solvent-saturated atmosphere causes the solvent to remain in the polymer-solvent • The non-solvent vapour diffuses into the thin film, forms membrane • Water flux is affected by the air velocity, temperature and duration of exposure	• Khare, et al., 2005
Thermal-Induced Phase Separation (TIPS)	• Heated polymer solution immersed into non-solvent coagulation bath • Microstruction of membrane is highly affected by mass and heat transfer • Suitable for MF	• Jung, et al., 2016

According to Liu and Kim (2011), the few most common polymeric material that utlizes immersion precipitation are summarized in Table 2.7.

Table 2.7: Pros and Cons of Polymers Used in Immersion Precipitation

Polymer	Advantages	Disadvantages
Polyamide (PA)	• Wide pH tolerance • Thermally stable • Large mechanical strength	• Low chlorine rejection
PS and PES	• Thermally stable • Wide pH tolerance • High chlorine rejection • Large mechanical strength	• Hydrophobic
Polyvinylidene fluoride (PVDF)	• Large mechanical strength • High chemical rejection • Thermally stable	• Hydrophobic

2.7.2 Interfacial Polymerization (IP)

IP is a polymerization process that synthesises a thin polymer film at the interface of two contacting solutions. The contacting solutions are one aqueous solution and an organic solution, they each contain a monomer different from each other (Alger, 1996). IP is often used in NF and RO membranes. One of the advantages is that it enhances the salt rejection and produces high water flux. The process initializes by immersing the porous support into PA solution. Next, the membrane is then submerged into an organic solution (Lalia, et al., 2013). With the added heat treatment, the membrane will be integrated with crosslinking.

This process greatly enhances the membrane's chlorine resistance as it allows for individually optimizing the active layer as well as the porous layer. As mentioned previously in Section 2.5.1, TFC are usually manufactured via IP with MPD and TMC as its main monomers. According to Ismail, et al. (2014), the thin PA layer is created by having MPD is dissolving in DI water as the aqueous solution and TMC dissolving

in hexane as the organic solution that will be place in contact with each other. IP is carried out as per Figure 2.10.

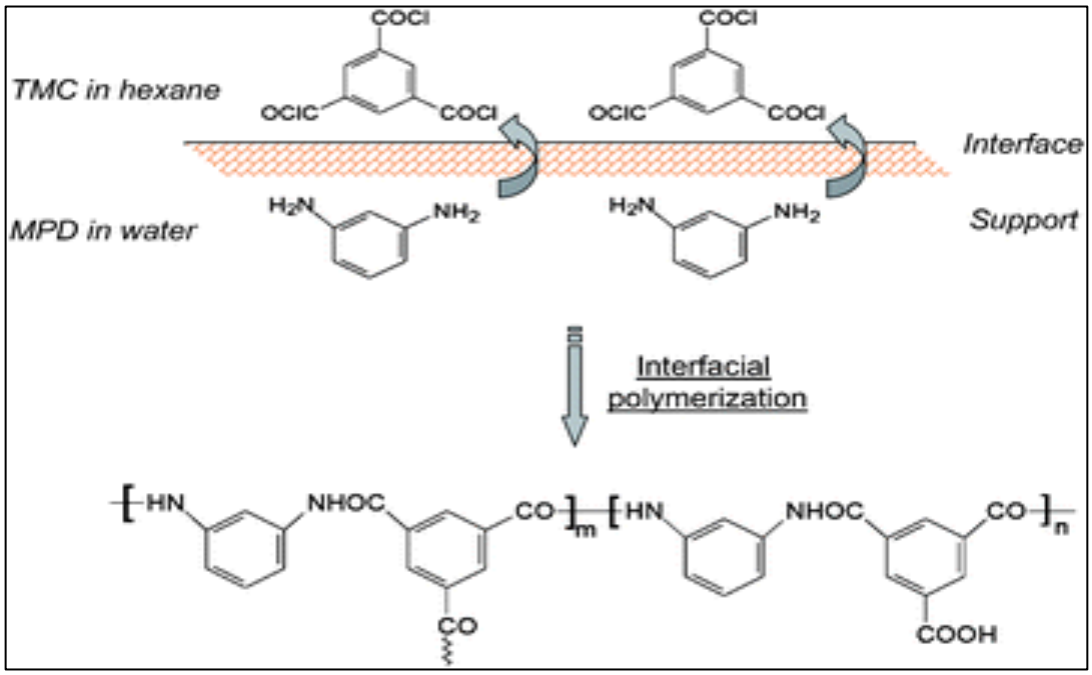

Figure 2.10: IP of MPD and TMC to form PA

2.7.3 Other Casting Method

Aside from PI and IP, there are also other casting methods such as stretching, track-etching, electrospinning and they are as outlined in Table 2.5 below.

Table 2.8: Description of Other Membrane Casting Methods (Lalia, et al., 2013)

Casting Methods	Descriptions
Stretching	• Initialized by extrusion, then stretching (cold stretching and hot stretching) by heating polymer over its boiling point. • Does not require solvent • To fabricate membranes for MD, MF and UF • Perfect for crystalline polymers

Continued

Casting Methods	Descriptions
Track-etching	• Ions irradiated onto surface of film causing tracks to be formed • Great control on the porosity • Porosity depends on exposure time • Pore size depends on etching time and temperature
Electrospinning	• Formation of liquid jet through the electrostatic potential between polymer solution and ground collector • To fabricate membranes for filtration and MD • Great control on the fibre size, shape and morphology

2.8 Selection of Draw Solution

To select any solution as the draw in an FO and PRO system, the main criteria is that it must possess a greater osmotic pressure than the feed side. Aside from that, the lower the draw solute reverse flux, the better more efficient the system. This can be achieved by ensuring the concentration differences of solutions on both sides are not that large (Ge, et al., 2012). Table 2.9 shows the common draw and feed solution of FO and its process characteristics.

Table 2.9: Common Draw Solutes in FO Processes Using Flat Sheet Membranes

Draw	Concentration of Draw	Osmotic Pressure	Feed Solution	Water flux	Reference
NaCl	0.60 M	28 atm	DI Water	9.6 L/m²h	Achilli, et al., 2010
$MgCl_2$	0.36 M	28 atm	DI Water	8.4 L/m²h	Achilli, et al., 2010
KCl	2.00 M	89.3 atm	DI Water	22.6 L/m²h	Phuntsho, et al., 2011
Polyglycol copolymer	30 ~ 70 %	40 ~ 95 atm	3.5% NaCl	≥ 4 L/m²h	Carmignami, et al., 2012

Ideal draw solutions are those that fully dissociates. It is also important that the selected draw solution contains minimal toxicity, inexpensive as well as easily recovered. Aside from that, draw solutions with larger molecules are also preferable

as it decreases the chances of reverse solute flow leading to a lower reverse flux (Setiawan, et al., 2011). Table 2.10 summarizes the reverse flux for different ionic salts as draw solutions. As analysed from Table 2.10, the reverse flux for 0.5 M NaCl for flat sheet membrane by Qiu, et al (2012) is low.

Table 2.10: Comparison of solute flow rates for TFC membranes

Feed solution	Draw solution	Water flux (L/m²h)		Reverse flux (g/m²h)		Type of TFC Membrane	Reference
		FO	PRO	FO	PRO		
DI water	2M NaCl	13.9	32.3	5.3	14.2	Flat sheet	Emadzadeh, et al., 2013
DI water	0.5M NaCl	9.54	16.6	3.0	6.1	Flat sheet	Emadzadeh, et al., 2013
DI water	0.5M NaCl	16.3	19.7	9.54	28.7	Flat sheet	Qiu, et al., 2012
DI water	2 M NaCl	34.5	65.1	9.87	12.34	Hollow fibre	Setiawan, et al., 2011
DI water	1.5M $MgCl_2$	11.7	17.2	3.9	37.7	Hollow fibre	Qiu, et al., 2012

More importantly, researcher Sobczuk and co-workers (2015) concluded in their paper that pure glycerol posses an osmotic pressure of over 90 MPa which is 3.5 times more than the osmotic pressure of common seawater (Sobczuk, et al., 2015). This will produce higher water flux in FO processes when compared to using seawater as a draw solution. As glycerol possesses a significantly high osmotic potential, it could be a good selection as draw solute. Aside from that, glycerol is also highly soluble and has the ability to form hydrogen bonding in water (Qiu, et al., 2012). It is also non-toxic, so the waste disposal process isn't as tedious.

CHAPTER 3

METHODOLOGY

3.1 Introduction

This chapter depicts the methods used to functionalize and characterize nanoparticles, incorporate the selected nanoparticles into membranes that will also be fabricated, characterize the fabricated membranes as well as describe the methods used to evaluate and carry out thorough performance study on the fabricated membranes. The experimental setup and design is thoroughly planned through to obtain the most accurate results possible.

3.2 Research Methodology

Figure 3.1 briefly outlines the flow chart of the overall experimental work that will be conducted throughout the research.

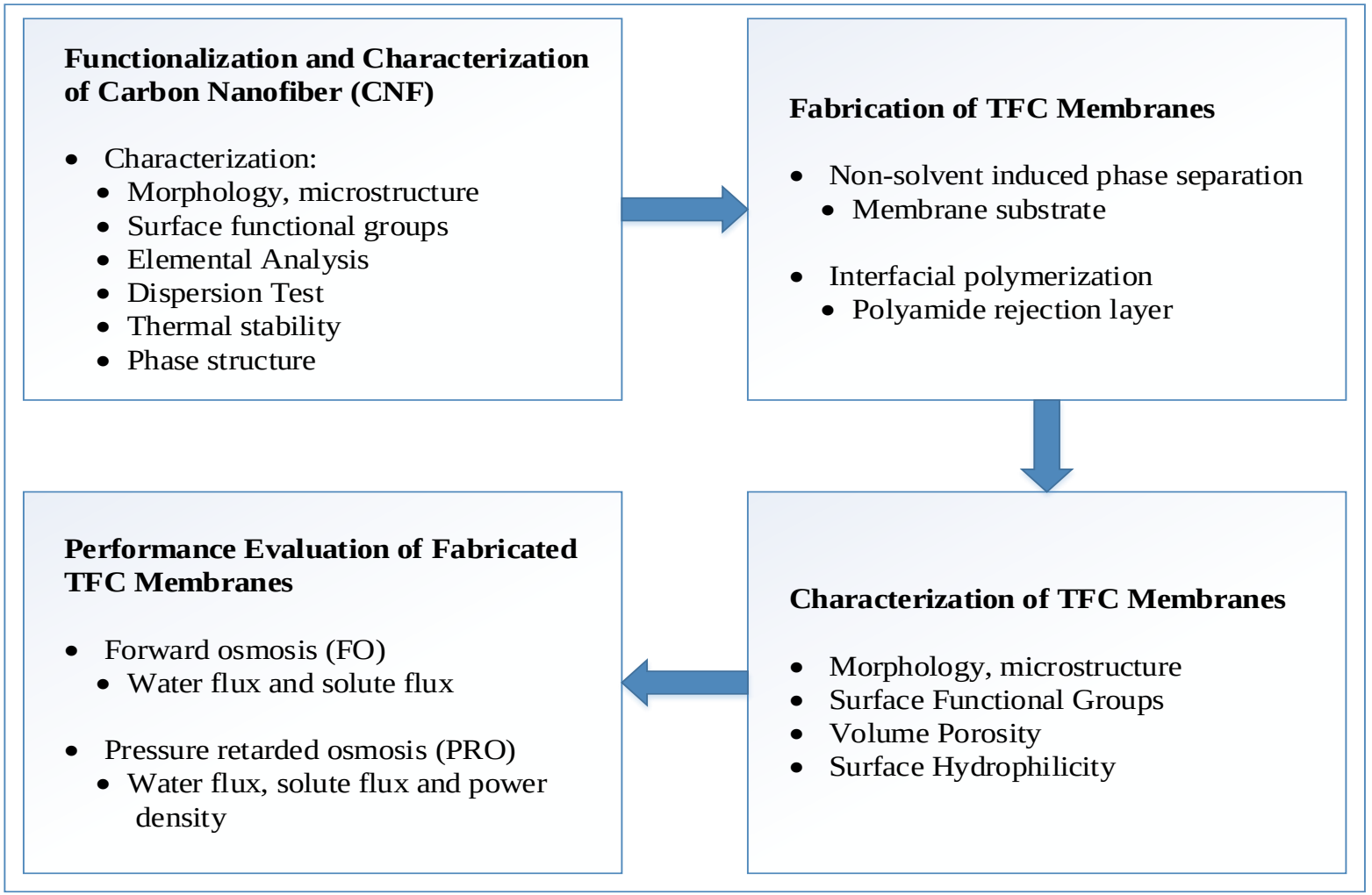

Figure 3.1: Flow Chart of Research Methodology

3.3 Materials and Apparatus

3.3.1 Raw Materials and Chemicals

Table 3.1 tabulates the complete list of the chemicals and raw materials required to carry out the functionalization of CNF, fabrication of CNF-incorporated TFC membranes, characterization of fabricated membranes and performance evaluation of membranes.

Table 3.1: List of Chemicals and Materials Required

Chemical/Material	Usage
Carbon Nanofiber (CNF)	To enhance membrane performance Specification: - 12.02 g/mol - Powder, conical platelets - Brand: Aldrich - Diameter: 130 nm - Pore size: 0.12 cm3/g average pore volume - Surface area: 39 m2/g average surface area
Sulphuric Acid (5M)	To functionalize CNF
Nitric Acid (5M)	To functionalize CNF
Nylon Membrane Filter	To filter and wash the functionalized CNF - Diameter: 47 mm
Deionized Water	To functionalize CNF, to be used as feed solution, to wash the functionalized CNF, to wash and store fabricated membrane
Glycerol	To be used as the draw solution

Continue

Chemical/Material	Usage
Polyetherimide (PEI)	To form the membrane substrate Specification: - Melt index: 9 g/10 min - Brand: Sigma-Aldrich
n-Methyl-2-pyrrolidinone (NMP)	As solvent to dissolve the polymer and disperse CNF Specification: - Anhydrous, 99.5 % - Brand: Sigma-Aldrich
Polyvinylpyrrolidone (PVP)	As a pore forming agent Specification: - 40000 g/mol - Brand: Alfa-Aesar
m-Phenylenediamine (MPD)	As aromatic diamine monomer to form PA layer Specification: - Flakes, 99 % - Brand: Sigma-Aldrich
Trimesoyl Chloride (TMC)	As polyacyl chloride monomer to form PA layer Specification: - 98 % - Brand: Sigma-Aldrich
Sodium Dodecyl Sulfate (SDS)	To enhance absorption of MPD into membrane substrate Specification: - 99 % - Brand: Sigma-Aldrich
n-Hexane	To dissolve TMC solids Specification: - 95 % Brand: Sigma-Aldrich

3.3.2 Apparatus, Equipment and Instruments

Table 3.2 and Table 3.3 tabulates the complete list of the apparatus, equipment and instruments required to carry out the functionalization of CNF, fabrication of CNF-incorporated membranes, characterization of fabricated membranes and performance evaluation of membranes.

Table 3.2: List of Apparatus and Equipment Required

Apparatus/Equipment	Usage
Volumetric Flask	To dilute concentrated acid
Reflux Apparatus	To functionalize CNF
A&D Digital Balance	To constantly record the weight of DI water during the membrane performance evaluation
Vacuum Filtration Apparatus	To filter and wash the functionalized CNF
pH meter	To aid in the washing of the functionalized CNF
Air Circulating Oven	To dry the functionalized CNF
Ultrasonicator	To carry out dispersion test
Glass plate	Used to form TFC membrane
Thin-Film Applicator	To apply spread the dope solution onto the glass plate
Acrylic Plastic Plate and Frame	To carry out IP
Soft Rubber Roller	To remove excess water on membrane surface
Storage Box	To store fabricated membranes

Tale 3.3: List of Instruments Required

Apparatus/Equipment	Specification	Usage
Scanning Electron Microscopy (SEM)	Hitachi SEM Model S-3400N	To determine the morphology and microstructure of CNF, f-CNF and fabricated TFC membranes
Fourier Transform Infrared Spectrometer (FTIR)	Thermo Scientific Nicolet iS10	To study the surface functional groups of CNFs, f-CNF and fabricated TFC membranes
Thermogravimetric Analysis (TGA)	Perkin Elmer Simultaneous Thermal Analyzer (STA) 8000	To measure the thermal stability of the CNF and f-CNF
X-ray Diffractometer (XRD)	Shimadzu LabX XRD-6000	To identify the phase structure of CNF and f-CNF
Contact Angle Goniometer	Rame-Hart Instruments Model 100-25-A	To determine the hydrophilicity of the fabricated TFC membrane
Refractometer	Sper Scientific 300034, Brix 0~95%	To determine the refractive index of the feed and draw solutions

3.4 Experimental Procedure

This sub-chapter described all the experimental procedure as well as the experimental setup conducted for this research.

3.4.1 Functionalization of Carbon Nanofiber (CNF)

The oxidation of CNF is initiated by mixing sulfuric acid, H_2SO_4 and nitric acid, HNO_3 together in a round bottom flask at a 3:1 ratio for a total volume of 160 mL (Emadzadeh, et al., 2013). Next, 0.5 g of CNF was added into the flask. The mixture was then refluxed and continuously stirred using a heating mantle for 5 hours at 100°C. The experimental setup is as shown in Figure 3.2.

As soon as the reflux process was completed, the mixture was set aside to be cooled to room temperature with the magnetic stirring remain turned on. The CNF-acid solution was then poured into a beaker containing DI water of a volume 10 times of the acidic solution used. The mixture was left stirring overnight. The experimental setup is as shown in Figure 3.3.

The next day, the overnight-solution was poured onto a 0.2 µm nylon membrane filter with a diameter of 47 mm through a filter funnel on a vacuum pump apparatus. After the filtration process, with the vacuum pump remained turned on, the CNF filter cake was repeatedly washed with DI water until the pH of the water that passed through is of neutral pH. The experimental setup is as shown in Figure 3.4. The filter cake was thoroughly scraped off the nylon membrane and then dried in an air-circulating oven for 48 hours at 80°C (Dabaghian and Rahimpour, 2015).

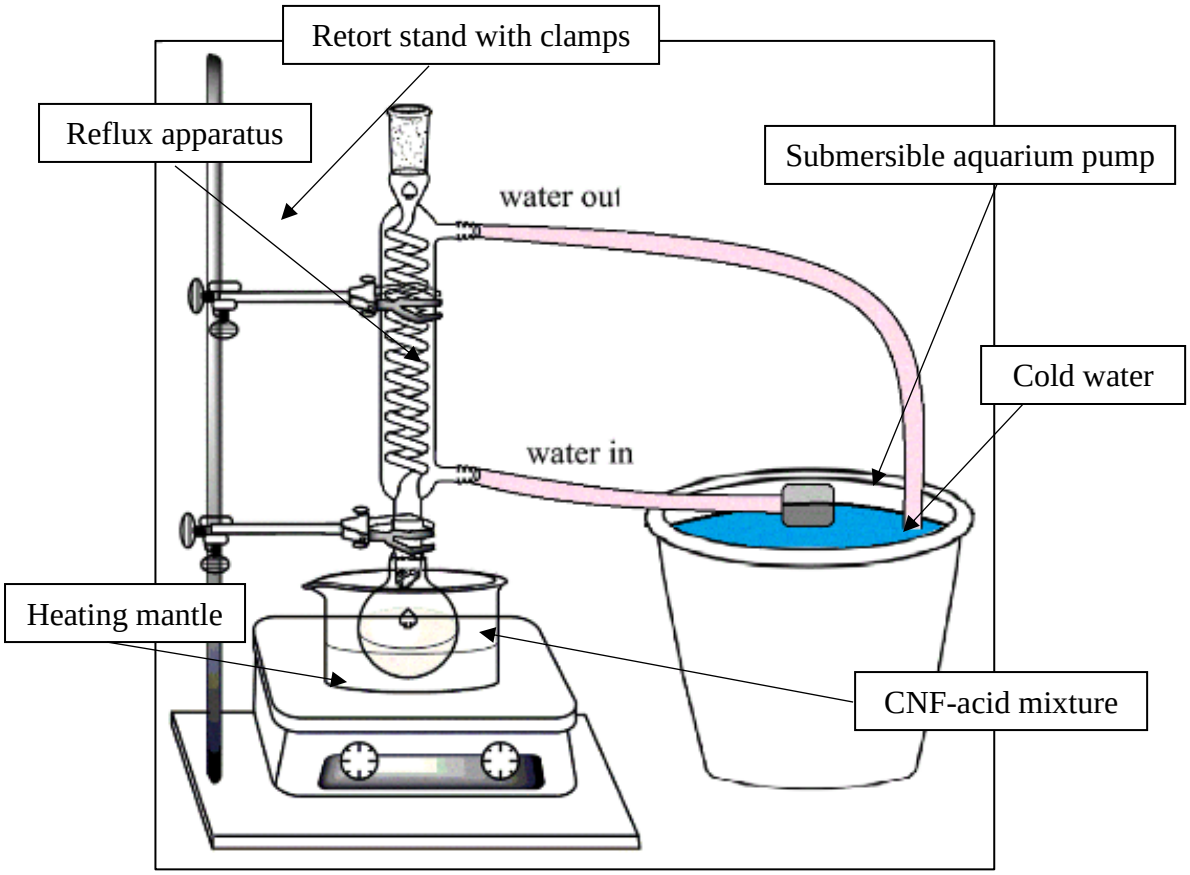

Figure 3.2: Experimental Setup of the Reflux Procedure for CNF Acid Treatment

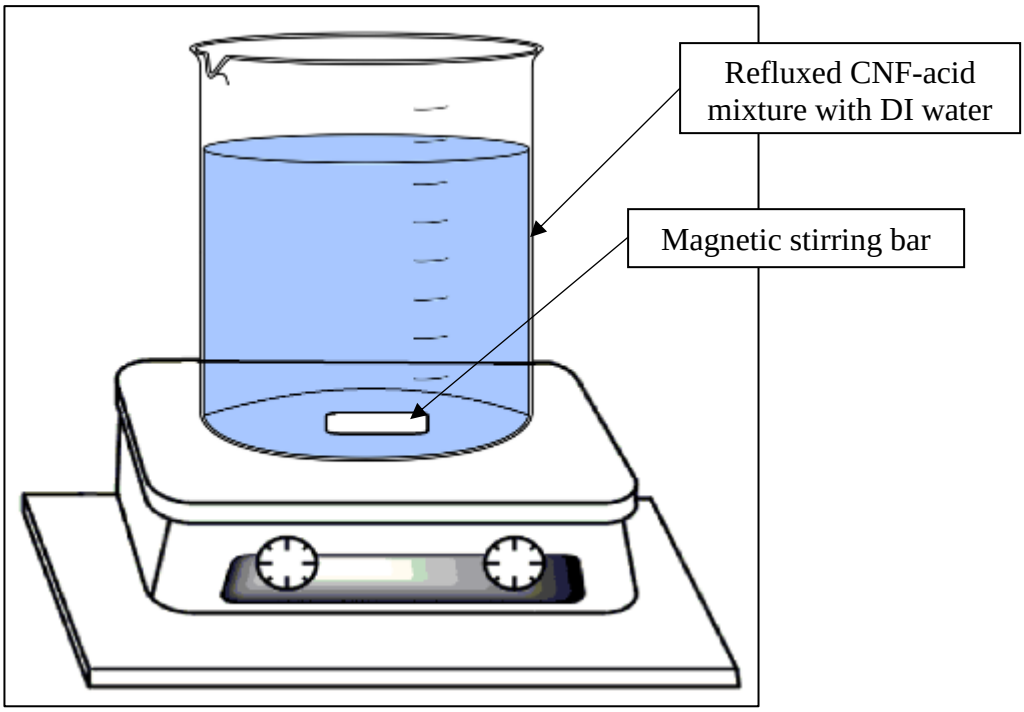

Figure 3.3: Experimental Setup of the Overnight Stirring Procedure

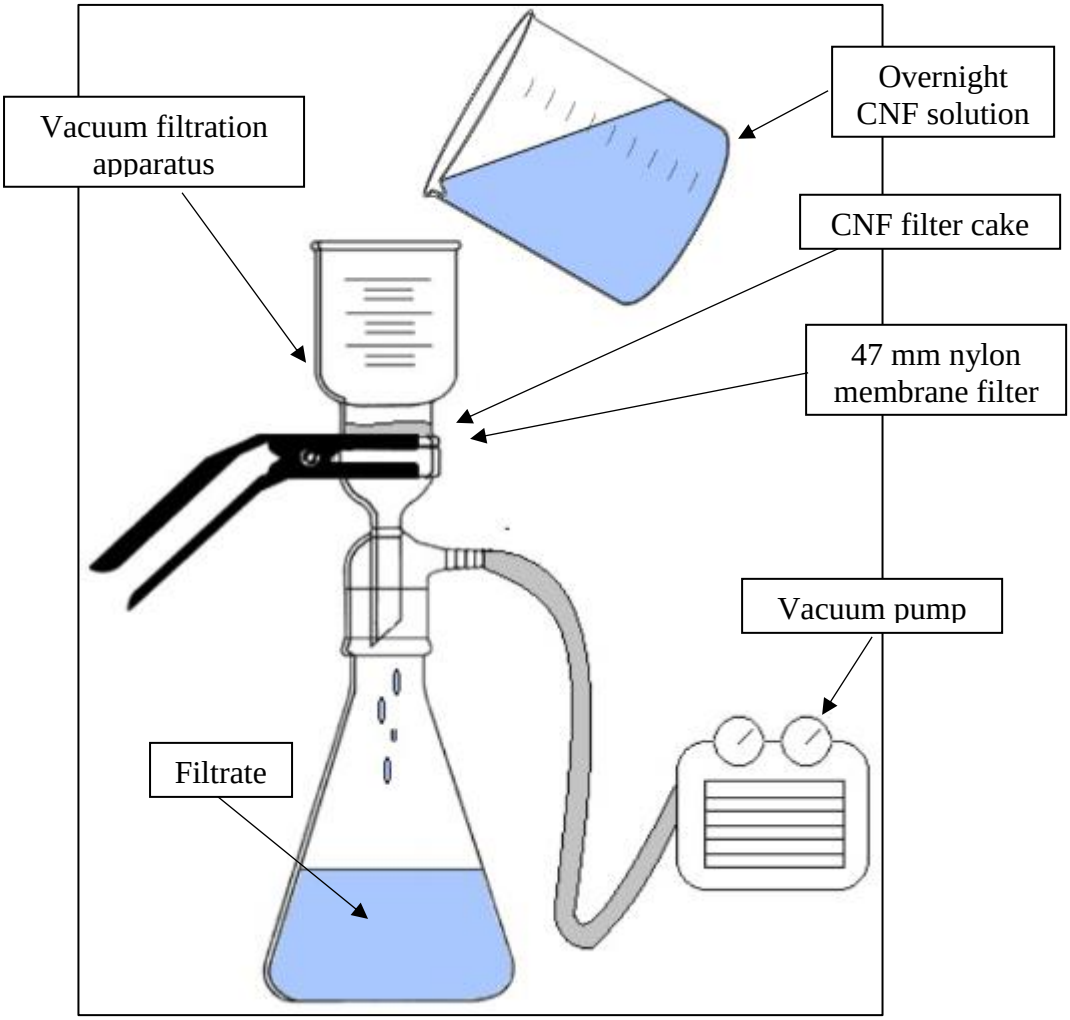

Figure 3.4: Experimental Setup of the Filtering and Washing Procedure

3.4.2 Fabrication of CNF-Incorporated Membranes

This sub-section describes the fabrication of membranes with the incorporation of CNF in two steps; the preparation of mixed matrix membrane via phase inversion and the formation of polyamide (PA) layer via interfacial polymerization.

3.4.2.1 Preparation of TFC Membrane via Phase Inversion

The preparation of the dope solution (casting solution) initiates by phase inversion, through immersion precipitation phase separation induced by a non-solvent solution. A designated quantity of the functionalized CNF (f-CNF) prepared in Section 3.4.1 was added into NMP solvent. NMP solvent was chosen because it is a good dispersing agent for carbon nanoparticles. The mixture was then put through an ultrasonication process for 30 minutes and then magnetic stirring for another 30 minutes (Chou, et al., 2013).

This step was to ensure that CNF was completely dissolved, has low agglomeration and becomes homogenous.

Next, powdered-form PVP was added into the homogenous mixture and magnetically stirred for 30 minutes. The PVP aids in the formation of pores. Beforehand, PEI polymer pellets were vacuum dried at a temperature of 80 °C for 24 hours to remove moisture. Then, dried PEI polymer pellets were added into the mixture, while continuously stirred. The addition of PVP and PEI was conducted gradually to avoid agglomeration and abrupt rise in viscosity. The dope solution was then continuously stirred for 1 days at 50°C (Choi, et al., 2006). The homogeneous dope solution was statically degassed for 3 hours at room temperature to remove trapped bubbles in the solution. The flowchart of the conducted experiment is as shown in Figure 3.5.

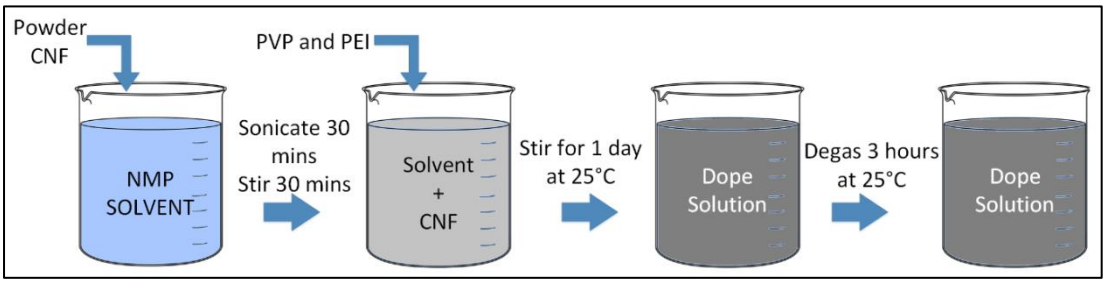

Figure 3.5: Experimental Setup for the Dope Solution Preparation

The degassed casting solution was carefully let flow onto the surface of a glass plate. The film applicator was set to a thickness of 200 µm and used to ensure that the solution was spread out into a thin film. To officially initiate the phase inversion process, the membrane was immersed together with the glass plate into a water bath at 25°C for 10 minutes (Konios, et al., 2014).

Then, the fabricated membrane was removed from the water bath and then submersed in a large container enclosed with DI water. The fabricated membrane was stored in the enclosed container for 24 hours (Choi, et al., 2006) to ensure all solvent residues and additives were eliminated. The experimental setup is as shown in Figure 3.6.

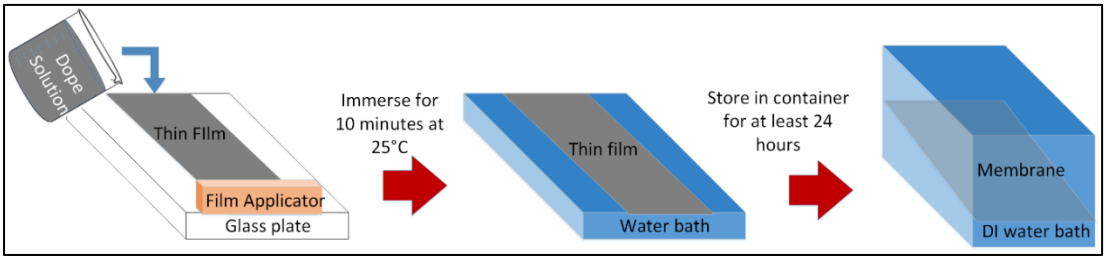

Figure 3.6: Experimental Setup for the Membrane Casting Procedure

3.4.2.2 Formation of PA Layer via Interfacial Polymerization (IP)

The 200 µm fabricated membrane's active PA rejection layer was synthesized via IP on the fabricated membrane substrate. The two monomers used in the IP process were MPD and TMC. Two solutions were prepared; dissolving 2/2 wt. % MPD/SDS in DI water and 0.1 w/v % TMC in n-hexane (Ren, et al., 2016). Both solutions were prepared at room temperature with continuous stirring.

A soft rubber roller was used to cart off excess water and residue from the membrane prepared in Section 3.4.2.1. Then, an acrylic plate and frame were used to clamp the membrane and to hold it in place while 50 mL of the prepared MPD/SDS aqueous solution was slowly discharged onto the membrane surface for 5 minutes (Ren, et al., 2016). After that, the membrane was stripped of excess residue and then dried in a fume hood.

The same pouring procedure was repeated with 50 mL of the TMC-hexane solution. However, the contact time was only for 1 minute. The end membrane was rinsed and dried in an air-circulating oven for 2 minutes at 70 °C (Cui, et al., 2014). IP occurs as soon as TMC-hexane was in contact with the MPD soaked substrate. The casted TFC membrane was thoroughly washed and then stored in a DI water bath until further testing was required. The experimental setup is as shown in Figure 3.7.

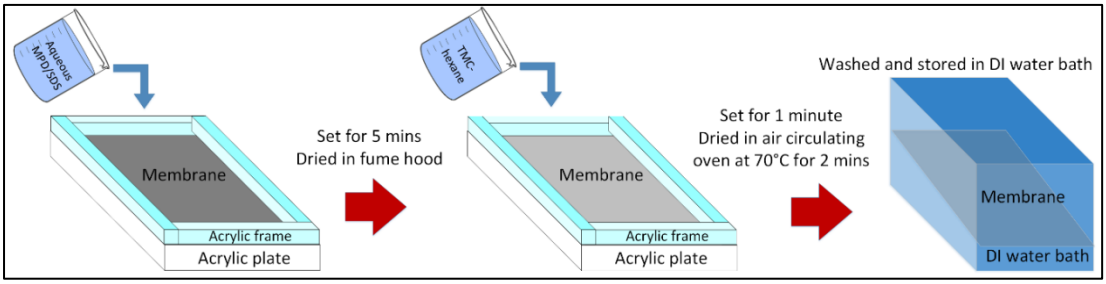

Figure 3.7: Experimental Setup for the Formation of PA Layer via IP

3.4.3 Characterization of CNF and Fabricated TFC Membrane

In this subtopic, the pristine as well as functionalized CNF were characterized. Aside from that, the characterization was also done for the fabricated membranes of different loadings with and without the formation of rejection layer were thoroughly studied based on its morphology, microstructure, pore size, existing functional group, thermal stability and many more.

3.4.3.1 Morphology of CNF and Fabricated Membrane

The morphology and microstructure of the f-CNF as well as the fabricated membrane was studied with the aid of Scanning Electron Microscopy (SEM). The instrument generates an electron beam that results in the production of a high-resolution image of the sample (Lai, et al., 2016). This assist in concluding whether if the f-CNFs were well dispersed in the membrane matrix. This method of characterization also assists in determining the morphology of the fabricated membrane's surface and cross-sectional area.

The microstructure of the fabricated TFC membrane was characterized under two conditions; membrane with and without the formation of rejection layer. Before entering the SEM, each of the membrane samples with different CNF loading was pre-treated and cracked in liquid nitrogen (Dabaghian and Rahimpour, 2015). This is to ensure that a homogeneous chip is produced throughout all the samples. Then, all moisture trapped within the membrane was stripped by air-drying for 24 hours (Kiadehi, et al., 2014) before being varnished with a thin gold layer to boost the electrical conductivity. The images produced by the SEM were saved and the pore size was measured based on the images.

3.4.3.2 Surface Functional Groups of CNF and Fabricated Membrane

With the aid of Fourier Transform Infrared Spectrometer (FTIR), the surface chemistry of f-CNF and the fabricated membranes were studied via an infrared beam passing through the sample. This assist in concluding whether or not the pristine CNF was successfully and properly functionalized to the desired state. The type of functional groups present in the fabricated TFC membrane was also studied.

Aside from that, the size of the peaks of the spectrum generated by the FTIR also determines the amount of the functional group present (Setiawan, et al., 2011); this assist in concluding whether or not the PA layer was successfully mounted onto the substrate layer.

3.4.3.3 Dispersity of CNF and f-CNF

The pristine and acid-functionalized CNF were put under a dispersity test to ensure that the pristine CNF was successfully modified as well as to determine how well CNF dispersed in n-Methyl-2-pyrrolidinone (NMP). Aside from only DI water, NMP was also used as a solvent in this test. The reasoning behind that is because NMP will be used as a solvent in the preparation of the membrane dope solution. It is crucial that the dispersity of the f-CNF in NMP is known before conducting the entire experiment.

Both powdered CNFs were immersed in DI water as well as NMP under two conditions; with and without the presence of sonication process. Hence, two sets of the following samples were prepared, one set to be hand-shaken and the other set to be sonicated; (i) pristine CNF in DI water, (ii) pristine CNF in NMP, (iii) f-CNF in DI water and (iv) f-CNF in NMP. The samples were prepared in vials and those that were to be sonicated were placed in an ultrasonication bath for 30 minutes (Liu & Kim, 2011). Observations were made 1 hour later based on whether the powdered nanoparticles dispersed well in the medium.

3.4.3.4 Phase Structure of CNF and f-CNF

X-ray Diffractometer (XRD) was used to study the phase structure of the powdered pristine CNF as well as the f-CNF. Before entering the analyser, the samples were

prepared by compacted the powdered CNF onto a metal slide. The XRD analyser identifies phases present in a crystalline sample.

The X-ray beam strikes the powdered sample and is then diffracted into different patterns (Lai, et al., 2016). The ray is positioned at various angles to obtained more information on the powder sample. These patterns are then pieced together to produce a 3D diffraction picture of the density of electron within the crystalline material. The results can predict the chemical bonds present in the sample (Kiadehi, et al., 2014).

The analyser characterized both CNF and f-CNF in terms of their crystalline structure. The XRD was set at a voltage of 40 kV, current of 30 mA, wavelength of 1.54 Å and a target of copper. The samples were at analysed at 2θ ranging from 5 ° to 70 ° and rate of 1.2 ° per minute.

3.4.3.5 Thermal Stability of CNF and f-CNF

Thermogravimetric Analysis (TGA) was used to analysed the thermal stability of the powdered pristine CNF as well as the f-CNF. The analyser determines the physical and chemical changes occurring in the sample as a function of time or temperature (Zhou, et al., 2010). The instrument heats up the sample while continuously measuring the weight of it to determine if any of the components in the sample is lost to the environment.

This characterization test is to determine whether if both conditions of the powdered CNF decompose at different rates in the presence of a nitrogen gaseous atmosphere. This is obtained from the weight change versus temperature curve. The temperature range used for the two samples are from room temperature up to 800 °C at a rate of 10 °C per minute (Feng , et al., 2014).

3.4.3.6 Volume Porosity of Fabricated Membrane

The fabricated TFC membranes with f-CNF loadings of 0.0, 0.1, 0.5 and 1.0 wt. % were all also placed under a porosity test to determine its overall volume porosity. The test initiated by cutting a 2 cm by 2 cm sample of each membrane and stripping it of all its

moisture content. The membrane samples were dried by storing them in small storage boxes containing silica gel pallets for 24 hours (Dabaghian and Rahimpour, 2015).

The weight of bone-dried membranes was measured. After that, the samples were immersed in DI water for 24 hours. The weight of the wetted membranes was then measured as well. The results were tabulated and the membrane's volume porosity for each CNF loadings were calculated with Equation 3.1

$$\varepsilon = \frac{\frac{m_{wet} - m_{dry}}{\rho_{water}}}{\frac{m_{wet} - m_{dry}}{\rho_{water}} + \frac{m_{dry}}{\rho_p}} \times 100 \quad (3.1)$$

Whereby the porosity of the TFC membrane is represented by ε, m_{wet} and m_{dry} are the weight of the dried and wetted membranes, ρ_{water} and ρ_p are the densities of DI water and polymer of the membrane substrate. In this case, the polymer used was polyetherimide (PEI).

3.4.3.7 Hydrophilicity of Fabricated Membrane

The hydrophilicity of the fabricated TFC membranes was analysed using the contact angle goniometer. The test was performed on the PA rejection layer of the membrane as well as both the bottom surface of the membrane. Aside from that, the second parameter that was tested were the membranes containing different f-CNF loadings. The samples were prepared by cutting the membranes with different loadings and mounting them onto a typical glass slide (Emadzadeh, et al., 2013).

The process was carried out by using DI water at approximately 25°C with a minimum number of five results, each at different positions of the membrane (Shepl, et al., 2014). As can be seen from Figure 3.8, a lower contact angle confirms that the surface of the sample exhibits higher hydrophilic properties.

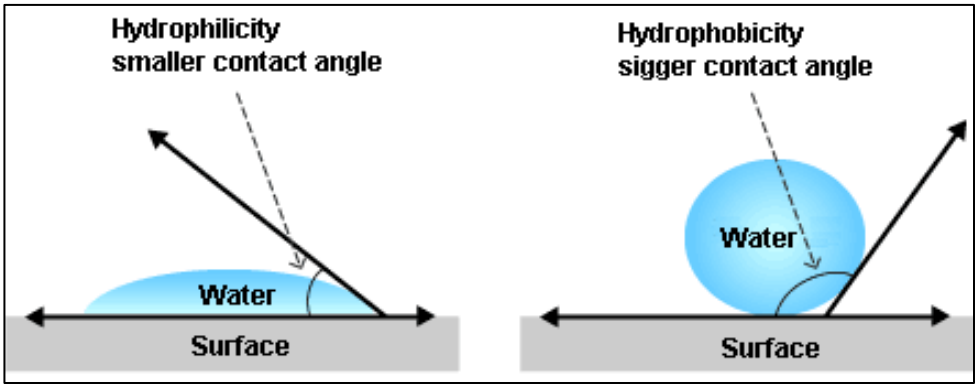

Figure 3.8: Contact Angle on the Surface of a Sample

3.4.4 Membrane Performance Evaluation

This sub-section thoroughly describes the method of evaluation of the membrane performance in two processes; FO as well as PRO.

3.4.4.1 Forward Osmosis (FO) Evaluation

Through the cross-flow FO membrane test unit as shown in Figure 3.9, the water flux and solute flux of the flow were studied and analysed. The setup commences with the feed solution of DI water in a beaker placed on top of a digital balance and the draw solution of glycerol in a beaker on alternative sides of the fabricated TFC membrane. The flow of the feed and draw solutions were initiated with the aid of a peristaltic pump.

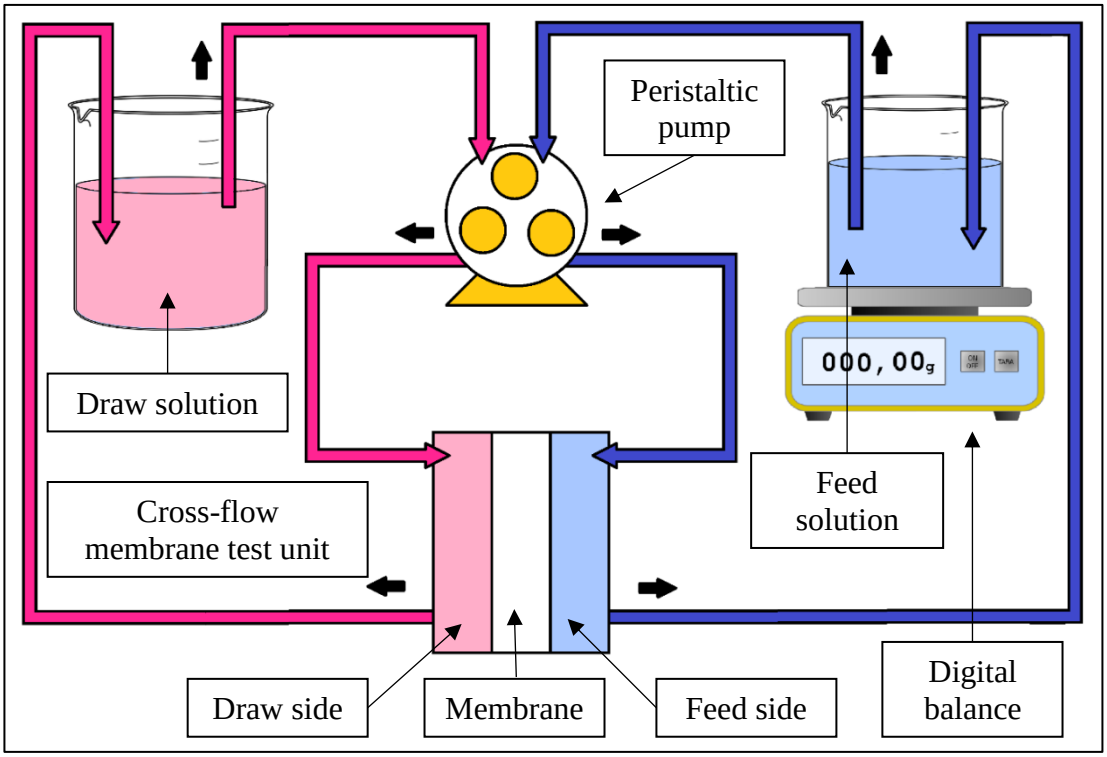

Figure 3.9: Experimental Setup for FO Evaluation

Both sides of the solutions were pumped into the crossflow setup, meeting at the cell, both solutions were separated by as well as in contact with the membrane. The water and solute flux were obtained based on the initial and final readings of the digital balance. The reading of the A&D digital balance was continuously recorded for every 1-minute interval for 30 minutes to obtain a linear plot. This was possible by utilizing the WinCT software provided. The initial and final mass and volume of the DI water feed was measured and the water flux was calculated with the formula as in Equation 3.2.

$$J_w = \frac{\Delta m}{\rho A_m \Delta t} \tag{3.2}$$

where Δm is the change in mass of the feed solution, ρ is the density of the feed solution, A_m is the effective area of the membrane and Δt is the change in time. The effective area of the membrane of the system is approximately 42 cm² while the crossflow rates of the feed and draw solution is 300 mL/min. The experiment was repeated with

fabricated membranes of different CNF loadings; 0 wt. %, 0.1 wt. %, 0.5 wt. % and 1.0 wt. % CNF.

The reverse solute flux was also generated for each set of readings by measuring the refractive index of the DI water feed to ensure that the experiment was being conducted at optimum condition as well as to troubleshoot any discrepancies. The glycerol concentration on the feed solution is calculated with the aid of the calibration curve attached in Appendix C.

3.4.4.2 Pressure Retarded Osmosis (PRO) Evaluation

The PRO evaluation was carried out with the cross-flow PRO membrane test unit as shown in Figure 3.10. Alike to the FO evaluation setup, the process commences with the feed solution of DI water also placed on top of a digital and glycerol as draw solution. The flow of the feed and draw solutions were also initiated with the aid of a peristaltic pump.

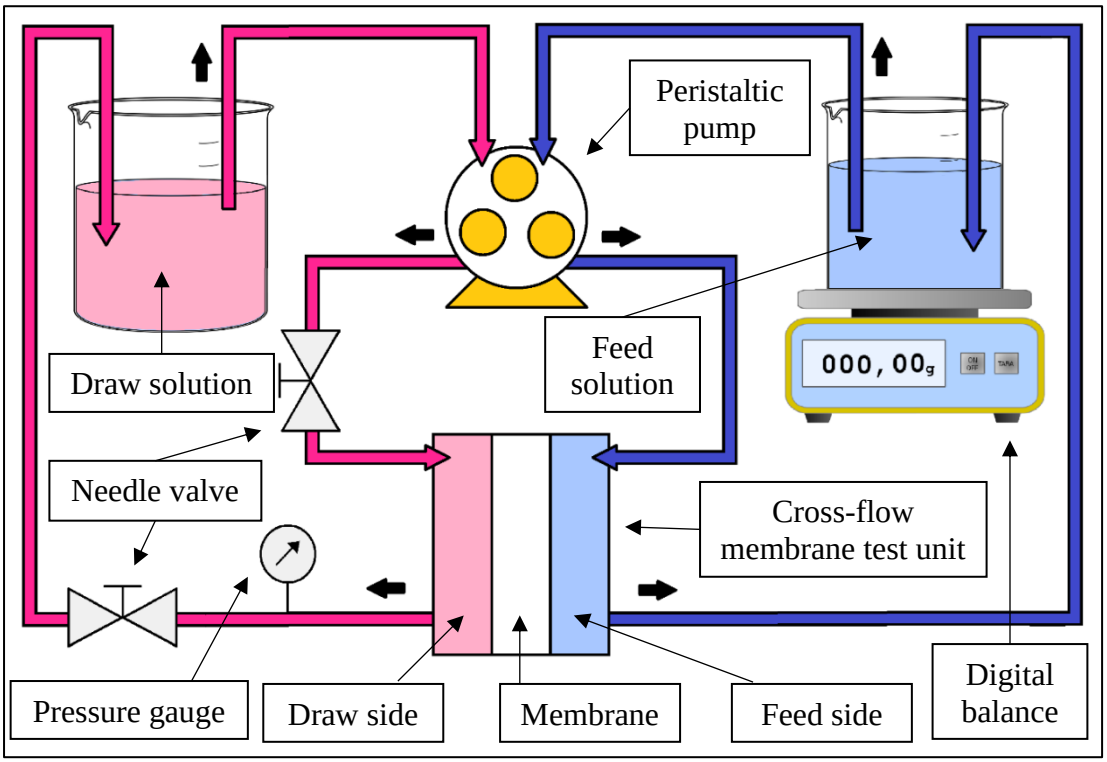

Figure 3.10: Experimental Setup for PRO Evaluation

Since PRO has an additional hydraulic pressure as compared to FO, two needle valves were installed at the draw side of the membrane to control the pressure of the system; one at the entrance to the membrane and one after the draw solution exits the membrane (Tian, et al., 2013). The PRO test was conducted under two pressure conditions; unpressurized and pressurized at 1 bar. The needle valves were adjusted accordingly.

Both the feed and the draw solution were pumped to the membrane surfaces to be in contact with each other. Alike to FO performance evaluation, the water and solute flux were also obtained based on the value changes of the digital balance at every 1-minute interval for 30 minutes. The power density estimation was made based on the water flux and difference in pressure. The pressure reading on the gauge is recorded every 3 minutes throughout the experiment. The experiment was repeated with membranes of different CNF loadings; 0 wt. %, 0.1 wt. %, 0.5 wt. % and 1.0 wt. % CNF.

The water flux of the system was calculated based on Equation 3.2 according to the initial and final reading of the digital balance. The power density was calculated based on Equation 1.3 with ΔP being the difference in the initial and final reading of the pressure gauge values.

The reverse solute flux was also generated for each set of readings by measuring the refractive index of the DI water feed to ensure that the experiment was being conducted at optimum condition as well as to troubleshoot any discrepancies. The glycerol concentration on the feed solution is calculated with the aid of the calibration curve attached in Appendix C.

CHAPTER 4

RESULTS AND DISCUSSION

4.1 Characterization of CNF and f-CNF

In this sub-chapter, a thorough study on the pristine CNF as well as f-CNF has been done. The characterization of the above-mentioned nanoparticles has been done based on its morphology, surface functional groups, thermal stability, phase structure as well as a comparative dispersion test in n-Methyl-2-pyrrolidinone (NMP).

4.1.1 Morphology and Microstructure

The micrograph obtained from the Scanning Electron Microscopy (SEM) for pristine CNF and acid-functionalized CNF is as depicted in Figure 4.1. The micrograph illustrates the comparative microstructure between the two conditions of CNF. With this, it was possible to determine if f-CNF was properly and successfully functionalized to the desired state as the strong acid bath may deteriorate the fibers during the functionalization process.

Based on Figure 4.1 (a), it can be observed that pristine CNF has a very fine, smooth and clean tubular surface. However as can be seen in Figure 4.1 (b), the structure of the acid-functionalized CNF was no longer smooth and clean. It has a bumpy and groovy surface with large spherical arrays attached onto the fibers (Goh, et al., 2012). The acid-functionalized CNF is also more densely packed as compared to pristine CNF. The rough surface finish of f-CNF can be explained by the acid-functionalization treatment the fibers had undergone whereby hydrophilic functional groups such as carboxyl group (COOH) were grafted onto its surface (Buang, et al., 2012).

Aside from that, it can also be observed that even after acid-treatment of CNF, f-CNF still preserved its ‘cup-stacked’ tubular shape and did not undergone much structural damage to its fibers. With this, it can be confirmed that f-CNF was properly functionalized (Favvas, et al., 2013).

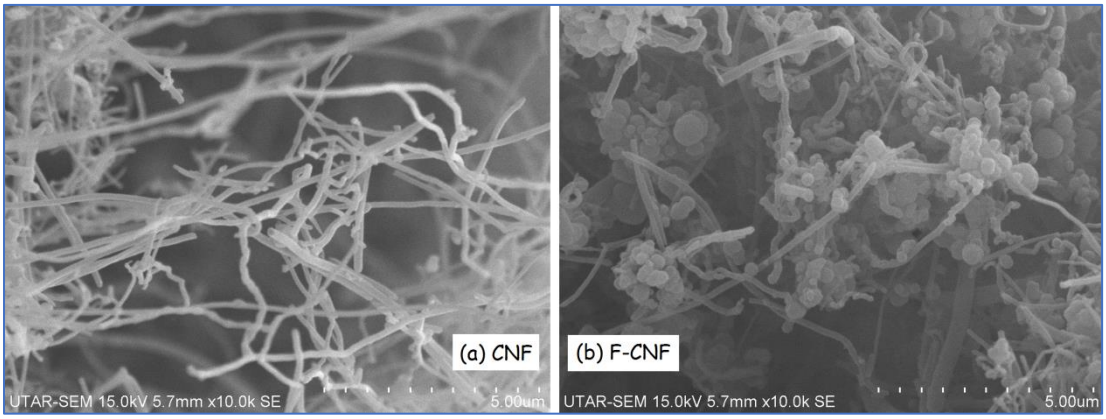

Figure 4.1: SEM Micrograph of (a) Pristine CNF and (b) Functionalized CNF

4.1.2 Surface Functional Groups

The spectrum obtained from the Fourier Transform Infrared (FTIR) spectroscopy for the pristine CNF and the acid-functionalized CNF is as depicted in Figure 4.2. The spectra show various discrepancies in peaks between the two conditions of CNF; this indicates the difference in functional groups as well as its intensities present in the sample. With this, it was also possible to determine whether if f-CNF was properly and successfully functionalized to the desired state. Figure 4.2(a) shows the spectra of pristine CNF and (b) show the spectra of the functionalized CNF.

Based on the enlarged FTIR spectra in Figure 4.2, the peak observed at approximately 1639 cm^{-1} for both pristine CNF as well as f-CNF spectrum expresses the stretching of the carbon nanofiber backbone (Buang, et al., 2012). This peak is essential as it describes the functionality of f-CNF; that it still retained its original structure and no damage or defects occurred to the fiber even after the acid-functionalization treatment (Ahmed, et al., 2013).

Aside from that, another peak around 1706 cm^{-1} was found in the spectra for the acid-functionalized CNF in Figure 4.2 (b). This peak represents the carbonyl group (C=O) stretching caused by the carboxylic acid present in the sample. This stretching is can be explained by the acid treatment after bathing CNF in a mixture of sulphuric acid and nitric acid (Mallakpour & Zadehnazari, 2013).

Next, a weak surface peak at 1406 cm^{-1} was also found in the f-CNF sample. This was the hydroxyl (O-H) group bending that was found grafted onto the fiber. Similarly, this was also caused by the acid treatment that f-CNF had undergone (Rana, et al., 2012). The O-H bending could also be explained by the water absorption during the acid treatment of f-CNF (Klein, et al., 2008).

The overall C-H stretching in the structure for f-CNF has decreased in intensity when compared to pristine CNF. This can be explained by the reduced about of C-H bond that can be found on the surface of the fiber as there are other functional groups attached (Rana, et al., 2012).

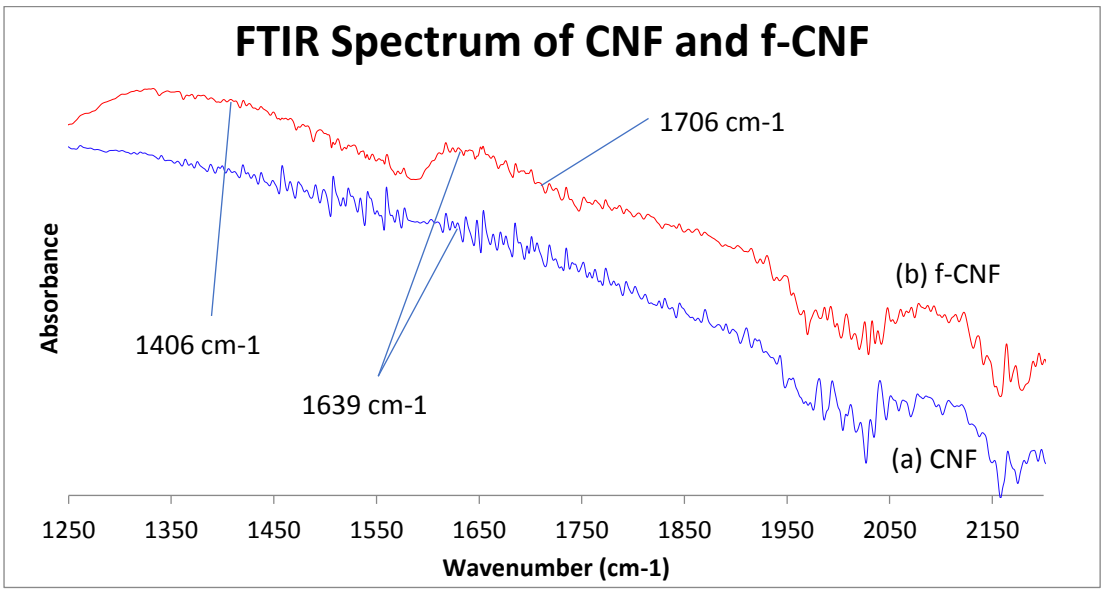

Figure 4.2: FTIR Absorption Spectrum of (a) CNF and (b) f-CNF

4.1.3 Elemental Analysis

Table 4.1 shows the results obtained from the elemental analysis conducted on pristine CNF as well as acid-functionalized CNF. Based on the following data, three main elements were found in the two samples; carbon, oxygen and sulphur.

Based on Table 4.1, it was concluded that there were only two elements found in pristine CNF sample with carbon being the dominant element at 99.38 wt. %. It was also the dominant element in the f-CNF sample with 88.19 wt. %. Functionalized CNF has a lower carbon weight percentage in as compared to pristine CNF due to the acid

treatment f-CNF had undergone, whereby more oxygenated functional groups were grafted onto its surface and thus lowering its carbon content.

The minor content of oxygen found in pristine CNF with 0.62 wt. % was due to the mild oxidation of the surfaces (Buang, et al., 2012). However, f-CNF successfully exhibits high content of oxygen after functionalization. This confirms that f-CNF was properly and successfully functionalized to the desired state as necessary hydrophilic functional groups were attached onto the surfaces of the fiber.

Aside from that, a low content of sulphur element was also found in f-CNF sample at 4.67 wt. %. This could be caused by the acid-functionalization treatment whereby residual sulphuric acid contents were also left on the surfaces of the fibers (Rana, et al., 2012).

Table 4.1: Elemental Analysis of Pristine CNF and f-CNF

Element	Amount (wt. %)	
	CNF	f-CNF
Carbon	99.38	88.19
Oxygen	0.62	7.14
Sulphur	0.00	4.67

4.1.4 Dispersion Comparison Test

Figure 4.3 (a) shows the results of the dispersion test conducted on the pristine CNF whereas Figure 4.2 (b) show the result of the test conducted on f-CNF. Based on the following figure, a drastic divergence between the two set of samples can be observed. There are two solvents in this test, DI water and n-Methyl-2-pyrrolidinone (NMP).

From Figure 4.3, it can be observed that both forms of CNF are more well-dispersed in vials (iii) and (iv) as compared to vials (i) and (ii), producing an almost homogeneous carbon black solution. This is due to the 30-minute ultrasonication process these 4 vials were put through. The sound energy produced by the ultrasonicator worked by homogenizing the nanoparticles in the solvent (Rana, et al., 2012).

Although the extra sonication process does assist in increasing the dispersity of the nanoparticle, the solution in vials (a) (iii) and (iv) are still less homogenous as compared to that of vials (b)(iii) and (iv); suspensions and sediments can still be observed in vials (a)(iii) and (iv). This can be explained in terms of the state of the nanoparticles themselves.

The pristine CNFs are not able to disperse well in DI water or NMP because of its lack in hydrophilic surface functional groups. This causes it to diverge itself and suspend as well as sediment within DI water as well as NMP solvent (Buang, et al., 2012). This confirms that pristine CNF itself is insufficient and inefficient to be incorporated into composites as it will not be able to homogenize well in the polymer matrix, even with the help of an ultrasonicator as can be seen in (a) (ii) and (iv). Pristine CNF will not be able to produce competent or profitable composites when used as a form of reinforcement. Hence, it has to be modified to be compatible to its solvent or polymer matrix.

In contrast to pristine CNFs, f-CNF dispersed much better as compared to the pristine CNF (Ahmed, et al., 2013), even without the help of an ultrasonicator as can be seen in (b) (ii). The f-CNFs are almost thoroughly soluble in (b) (iii) DI water as well as (b) (iv) NMP when sonicated. This is due to the previous carboxylation process during the functionalization of CNF whereby it was bathed in sulphuric acid and nitric acid (Favvas, et al., 2013). During this process, additional carboxyl (COOH) groups were attached onto the surface of the fiber, causing it to increase in hydrophilicity. The functionalization process also increases the fiber's capability of forming more hydrogen bonding with the solvent (Favvas, et al., 2013). Hence, this confirms that the f-CNF was successfully functionalized by the acid mixture.

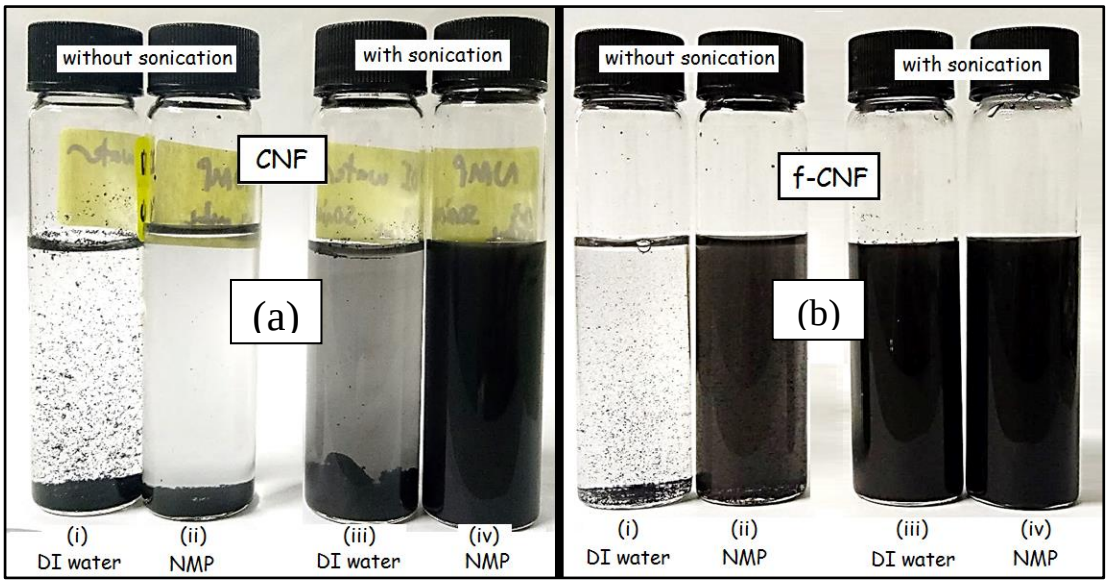

Figure 4.3: Dispersion Test for (a) (i) Pristine CNF in DI water, (ii) Pristine CNF in NMP, (iii) Pristine CNF in DI Water with Ultrasonication, (iv) Pristine CNF in NMP with Ultrasonication and (b) (i) f-CNF in DI Water, (ii) f-CNF in NMP, (iii) f-CNF in DI Water with Ultrasonication, (iv) f-CNF in NMP with Ultrasonication

4.1.5 Thermal Stability

The percentage weight change as a function of time of pristine CNF and f-CNF is as plotted in Figure 4.4. The data obtained from the thermogram shows the nanofiber's weight response to a uniformly increasing temperature.

Based on Figure 4.4 (a), it can be observed that the pristine CNF powder began having a drastic weight loss at 677 °C. The rate of weight reduction continued to increase until the end of the heating process at 800 °C. On the other hand, in Figure 4.3 (b), the f-CNF powder already began its weight loss gradually from 100 °C and plunges at 585 °C. The escalation in weight loss of f-CNF occurs at a lower temperature as compared to that of pristine CNF. This is because the pristine CNF powdered sample is purer and contains less impurities and catalyst residues (Buang, et al., 2012).

Aside from that, f-CNF has a higher total weight loss as compared to pristine CNF. The final weight percentage of CNF and f-CNF is 90.1 % and 83.4%, respectively. This is because after the acid-functionalized process of CNF, there are many hydrophilic as well as oxygen-based functional groups attached onto the surface of the fiber

structure, such as the carboxyl (COOH) group (Buang, et al., 2012). This enables ease of combustion of f-CNF powder at a much lower temperature as compared to CNF (Chatterjee & Deopura, 2006).

Based on Figure 4.4, it was also proven that f-CNF is still thermally stable at high temperature when compared to pristine CNF. This is because no significant amount of defects occurred to the f-CNF structure when the temperature was raised during the decomposition of carbon (Mallakpour & Zadehnazari, 2013). Also, f-CNF is slightly more thermally stable as compared to that of pristine CNF due to its additional functional groups (Rana, et al., 2012).

As can be observed in Figure 4.4 (a), there was an increase in weight percentage during the heating of pristine CNF powder. The maximum weight percentage obtained from the data was 112.86 %, the weight only began decreasing at 581.75 °C. The experiment was attempted several times; however, the results obtained were still the same. This phenomenon could be caused by buoyancy effects and can be explained with Archimedes' principle (THASS - Thermal Analysis & Surface Science GmbH, 2010). As the process initiates, the nitrogen gas surrounding the sample holder decreases in density as the temperature slowly increases. Hence, the weight of the sample recorded was affected by the changes in the surrounding gas causing an increase in weight percentage of the sample.

However, the increase in weight percentage tends to decrease at higher temperatures; in this case, it decreased after 581.75 °C. This is because as the temperature rises, the heat transfer to the sample is no longer governed by convection only. The main mode of heat transfer at higher temperatures is by radiation (THASS - Thermal Analysis & Surface Science GmbH, 2010). Hence, the recorded weight of the sample will not be affected so much by the buoyancy of the nitrogen gas, leading to a decrease in weight.

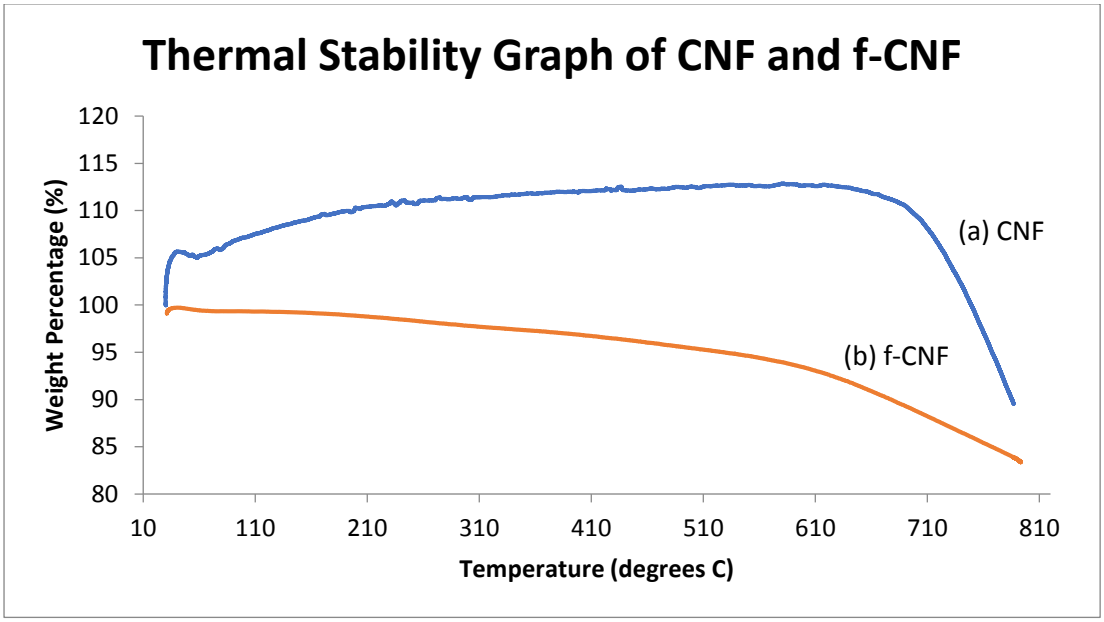

Figure 4.4: Thermal Stability of (a) Pristine CNF and (b) f-CNF

4.1.6 Phase Structure

The spectrum from the X-ray Diffractometer (XRD) for pristine CNF and f-CNF is as depicted in Figure 4.5. The spectra show various discrepancies in peak intensity between the two conditions of CNF. The intensities of each spectrum play in important role in the characterization as it determines the proportions of diffraction in the crystal spacing.

Based on Figure 4.5, both CNF and f-CNF show three sharp and dominant characteristic peaks at 2θ = (i) 25.85 °, (ii) 37.78 ° and (iii) 44.02 °. From the diffractogram, it can be seen that the highest diffraction peak was found at a 2-theta value of approximately 25.84 ° as depicted in (i) for both (a) CNF and (b) f-CNF. This peak represents the crystalline carbon in the sample (Mallakpour & Zadehnazari, 2013). The peak observed at (iii) 44.02 ° represents nickel present in the sample. The presence of this element is resulted from the growth catalyst of the sample (Sebastian, et al., 2010).

It is observed that both the XRD patterns are closely alike to each other in terms of peaks. This proves that even after functionalization, the structure of the nanofibers still remained in its ‘cup-stacked’ origin, leaving the inter-planar spacing fairly unchanged (Mallakpour & Zadehnazari, 2013). This analysis confirms that even after

the acid-treatment of f-CNF and addition of hydrophilic surface groups, the crystalline structure is still preserved and unmodified (Sebastian, et al., 2010). However, there are still slight discrepancies present between the two XRD patterns.

Functionalized-CNF showed a more broadened graphite peak at 25.85°. Aside from that, the graph's overall intensity is also lower as compared to that of CNF. The high intensity characteristic peak indicates a high abundance of graphite within the sample while the sharper characteristic peak indicates a higher crystallinity of graphite (Kiadehi, et al., 2014). Hence, this means that although they may seem undistinguishable, CNF generally has higher crystallinity and higher abundance of graphite as compared to f-CNF from Figure 4.5 (Sebastian, et al., 2010).

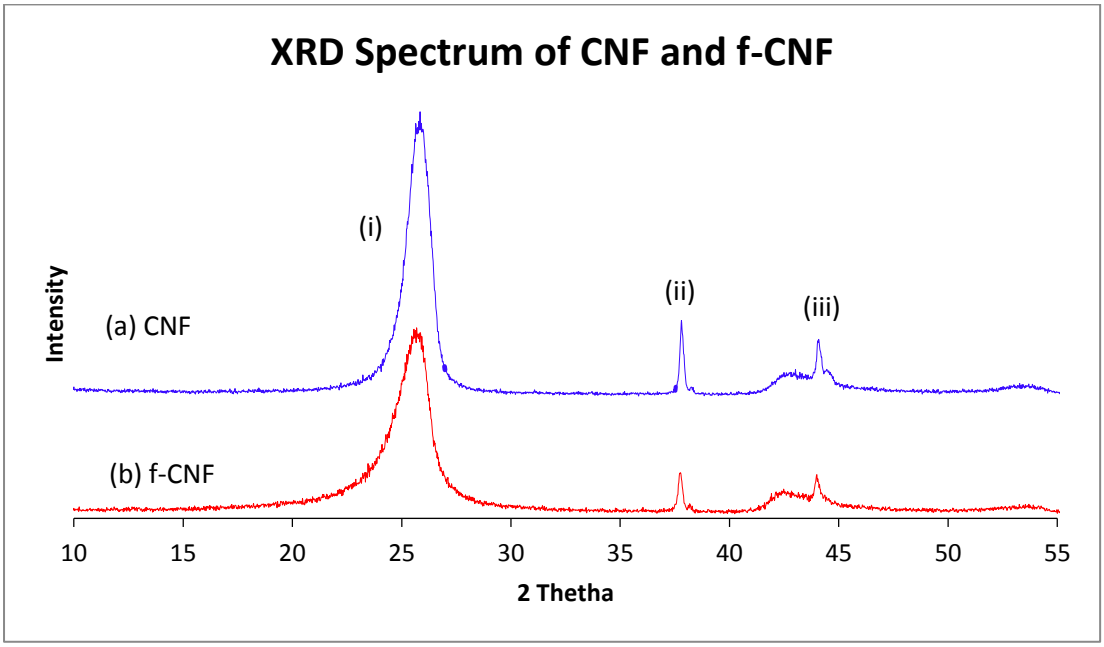

Figure 4.5: XRD Spectrum of (a) Pristine CNF and (b) f-CNF

4.2 Characterization of Fabricated Membrane

In this sub-chapter, a thorough study has been done comparatively on the fabricated f-CNF TFC membrane before and after forming the rejection layer on the membrane. The characterization of the above-mentioned membrane conditions has been done based on its morphology, porosity, hydrophilicity, surface chemistry as well as pore size and pore size distribution with the aid of a comparison table at the end.

4.2.1 Morphology and Microstructure

The micrograph obtained from the Scanning Electron Microscopy (SEM) illustrates the comparative microstructure of fabricated TFC membranes with different f-CNF loadings; 0.0, 0.1, 0.5 and 1.0 wt.%. With this, it was possible to determine its pore distribution as well as whether if the polyamide (PA) rejection layer was properly and successfully coated on the membranes.

Figure 4.6 depicts two different membranes; one with the addition of a polyvinylpyrrolidone (PVP) and one without. It can be observed from Figure 4.6 (a) that without the addition of PVP component, a rough surface finish was formed. However, when PVP was added into the polymeric casting solution, the 200 µm membrane in (b) appeared to be more porous than the membrane in (a). The outcome was reasonable and expected as PVP is a well-known pore forming agent in membrane studies, this statement was also proved by previous research works of Torres, et al. (2016). Through this morphology analysis, it can be confirmed that PVP successfully advocated more pores onto the membrane surfaces (Kim, et al., 2011)

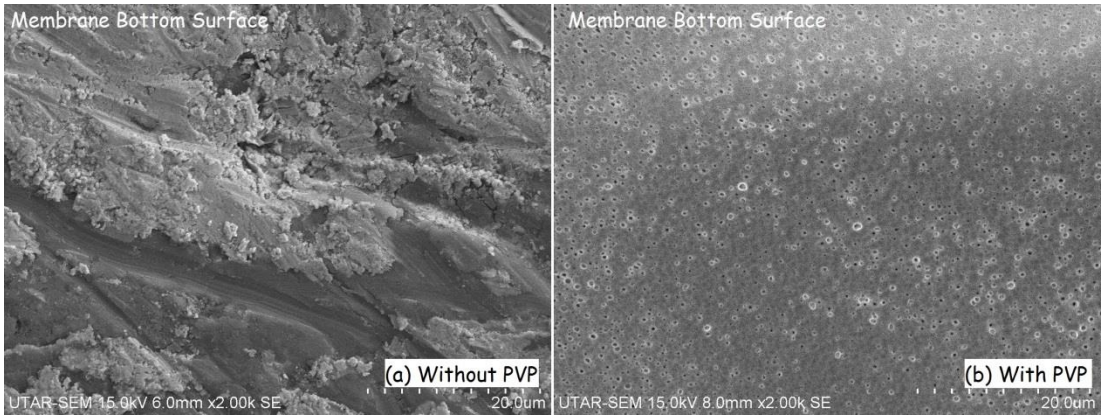

Figure 4.6: Bottom Surface of the Fabricated TFC Membrane (a) Without PVP and (b) With PVP

Figure 4.7 shows the morphology of the top surfaces of the fabricated TFC membranes under two conditions; (a) before and (b) after the formation of the PA layer. As emphasized by researcher Torres and co-workers (2016), most of the surface differences and characterizations are located at the bottom of the membranes. Hence,

the only studies that could be made on the top surface of the membrane are the verification of the PA layer existence.

Figure 4.7 (a) showed a plain dull surface while Figure 4.7 (b) showed a rough and feathery surface finish. The surface morphology of the membrane in 4.7 (b) is the result of the interfacial polymerization process between the two monomers; MPD and TMC (Torres, et al., 2016). In other words, the micrograph displayed in Figure 4.7 (b) proves the successful formation of the PA rejection layer on the membrane substrate (Ren, et al., 2016).

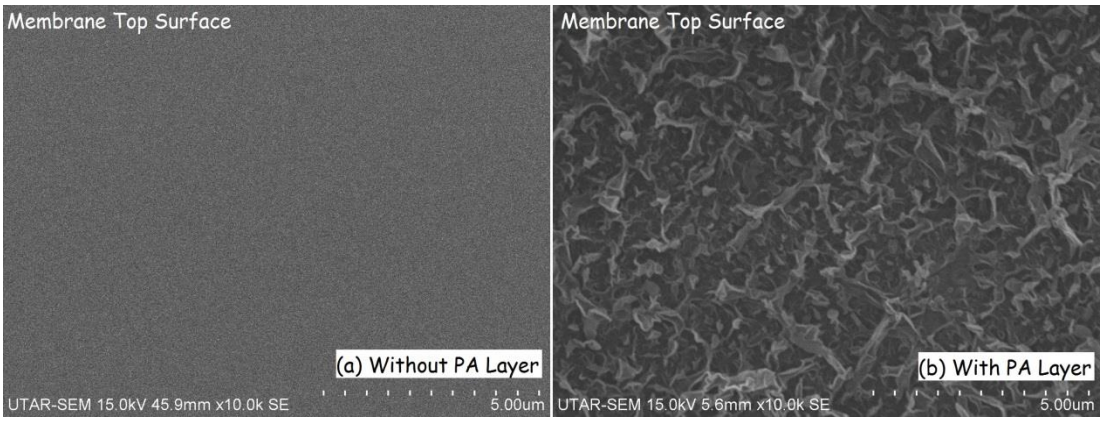

Figure 4.7: Top Surface of the Fabricated Membrane (a) without PA layer and (b) with PA layer

Figure 4.8 exhibits the bottom membrane surface morphology of membranes with different f-CNF loadings. As the loading of f-CNF increases, the colour of the fabricate membrane began to alter from a lighter shade of grey to a darker shade. Aside from that, the microstructures in Figure 4.8 show that the porosity of each membrane increases with increasing f-CNF loading; with morphology that resembles a porous sponge.

The increase in porosity and sponge-like structure is caused by the hydrophilic functional groups that were grafted onto the f-CNF surface during the acid-functionalization treatment. During the occurrence of immersion precipitation, more phase inversion was initiated when more hydrophilic contents of f-CNF were added into

the mix. This increases the formation of pores on the membrane during phase immersion (Vatapour, et al., 2011).

It was also observed that the macro-voids were more obvious in the membranes with higher f-CNF loading as seen in Figure 4.8 (d) for 1.0 wt.%. The pore size as well as number of pore increases with increasing f-CNF. These statements can also be explained by the hydrophilic functional groups present in f-CNF during phase inversion as justified by Dabaghian and Rahimpour (2015). According to Figure 4.8, the average pore sizes of membranes with f-CNF loading of 0.0, 0.1, 0.5 and 1.0 wt. % are approximately 5 µm, 5.71 µm, 8.21 µm and 11.43 µm, respectively; significantly proving the increase in pore sizes as loading increases.

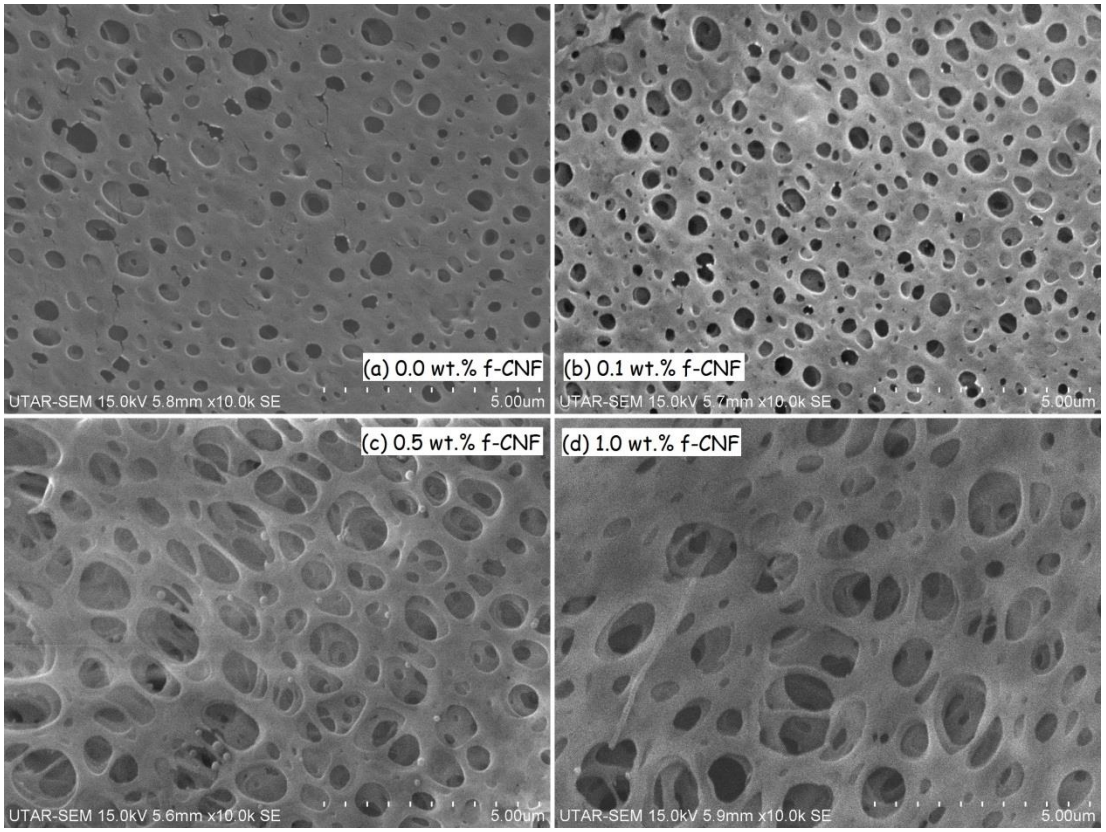

Figure 4.8: Bottom Surface of the Fabricated Membrane with (a) 0.0, (b) 0.1, (c) 0.5 and (d) 1.0 wt. % f-CNF Loading

The SEM micrograph in Figure 4.9 confirms that the fabricated TFC membrane consists of an asymmetrical structure and of two major layers; a densely packed top layer and a porous sub-layer. The formation of the dense top layer resulted from

evaporation of solvent during phase inversion when casted on the glass plate (Dabaghian & Rahimpour, 2015). The bottom porous layer was also formed during the phase inversion process; however, it was the part of the membrane that was in contact with the class plate. This resulted in a slight form of aggregation when it attaches itself onto the glass plate as seen in Figure 4.9 (Buang, et al., 2012).

Through Figure 4.9, it was also safe to conclude that there was no agglomeration of f-CNF in the polymer matrix. Many researchers such as Favvas and co-workers (2013) concluded that as the loading of f-CNF increases, agglomeration of nanoparticles will tend to occur and thus reducing the performance of the fabricated membrane. However, since no agglomeration was observed in Figure 4.9, it can be concluded that f-CNF was dispersed in a favourable manner (Ren, et al., 2016).

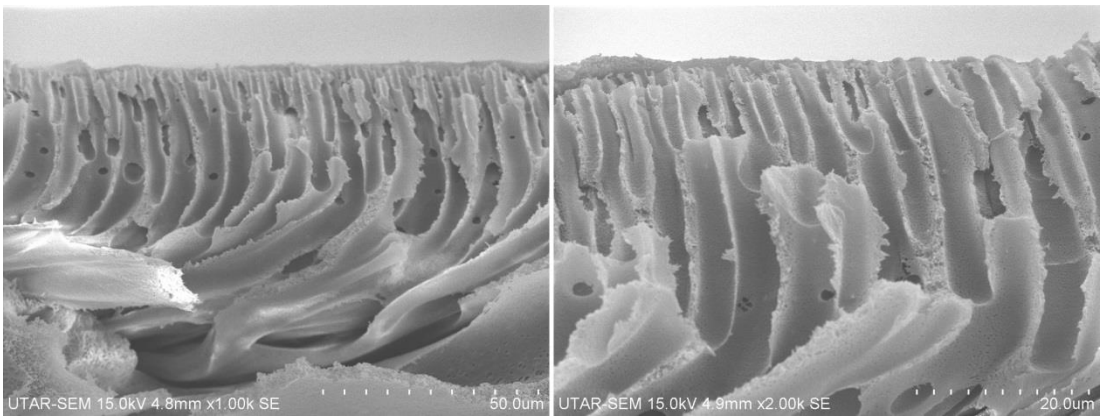

Figure 4.9: Cross-Sectional View of Membrane with 0.5 wt. % f-CNF Loading

4.2.2 Surface Functional Groups

The spectra obtained from the Fourier Transform Infrared (FTIR) spectroscopy for the fabricated membranes of different f-CNF loadings are depicted in the figures contained in this subchapter. The spectra showed discrepancies in peaks of the fabricated membranes under two conditions; with and without the formation of the polyamide (PA) rejection layer on the surface of the membrane substrate. This indicates the difference in functional groups as well as its intensities present in the sample. With this, it was also possible to determine whether if the PA rejection layer was properly and successfully formed and coated on top of the membrane substrate layer to desired state.

Before the TFC membrane was casted, 1 wt. % of polyvinylpyrrolidone (PVP) was added into the membrane casting solution for each membrane as a pore-forming agent (Torres, et al., 2016). Despite so, a confirmative test was conducted to ensure that PVP present in the membrane matrix before further forming the PA rejection layer above the membrane substrate. Based on Figure 4.10 (a), PVP displays its C=C stretching peak at approximately 1660 cm^{-1} (Nguyen Van, et al., 2014) whereas when compared to 4.4 (b) the same peak cannot be found in the membrane without PVP addition.

However, when the casting solution was added with the pore forming agent, a peak at 1660 cm^{-1} was formed in the spectrum. The spectrum obtained from the FTIR previously in Figure 4.4 (c) confirms the presence of PVP. This concludes that PVP was well dispersed as a pore forming agent in the mixed membrane matrix and its surface was ready to be coated with the PA rejection layer (Nguyen Van, et al., 2014).

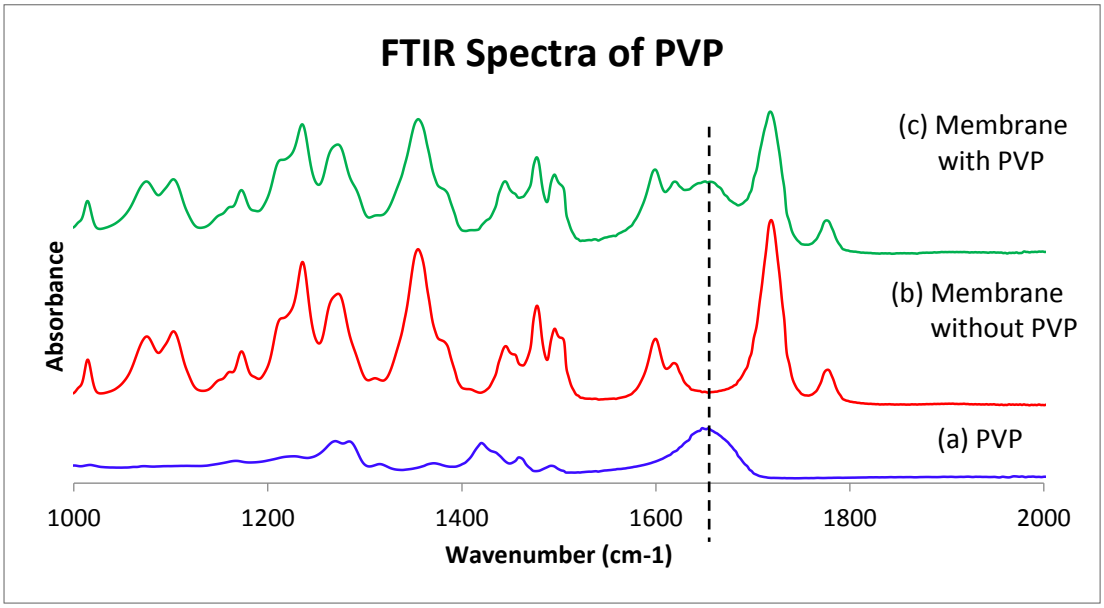

Figure 4.10: FTIR Spectrum of (a) PVP, (b) Fabricated TFC Membrane Without PVP and (c) Fabricated TFC Membrane With PVP

The spectrum in Figure 4.11, 4.12, 4.13 and 4.14 confirms the successful coating of PA rejection layer onto the surface of the porous TFC membrane substrate. Through the 4 figures, it was clearly observed that there were several peaks found in the membranes that were coated with PA layer that cannot be seen in those that were not

coated. Firstly, the membranes that were coated with the PA layer with f-CNF loadings of 0.0, 0.1, 0.5 and 1.0 wt. % exhibit additional peaks at 1541 cm^{-1}, 1539 cm^{-1}, 1539 cm^{-1} and 1542 cm^{-1}, respectively. These peaks can be found from Figure 4.11, 4.12, 4.13 and 4.14. These extra 4 peaks that were present in the membrane with PA layer represent the amide II bending that can be found in polyamide. These peaks were formed due to the vibrations of the N-H and N-C functional groups as confirmed by researcher Tang and co-workers (2009).

Aside from that, the notation labelled as (i) in Figures 4.11, 4.12, 4.13 and 4.14 represents the formation of amide I peak patterns (Tang, et al., 2009). The amide I functional groups was noticeable when it was attached to C=O and C-N stretching, this peak can be found at approximately 1629 cm^{-1}.

The intensities of C=O stretching due to carboxylic acids were also weakened in the membranes with the formation of PA layer as can be observed in all 4 figures. This resulted from the successful coating of the PA layer on the membrane surface, leading to lesser C=O functional groups detected by the FTIR on the surface (Tang, et al., 2009). The C=O stretching can be found at approximately 1720 cm^{-1} of figures 4.11, 4.12, 4.13 and 4.14.

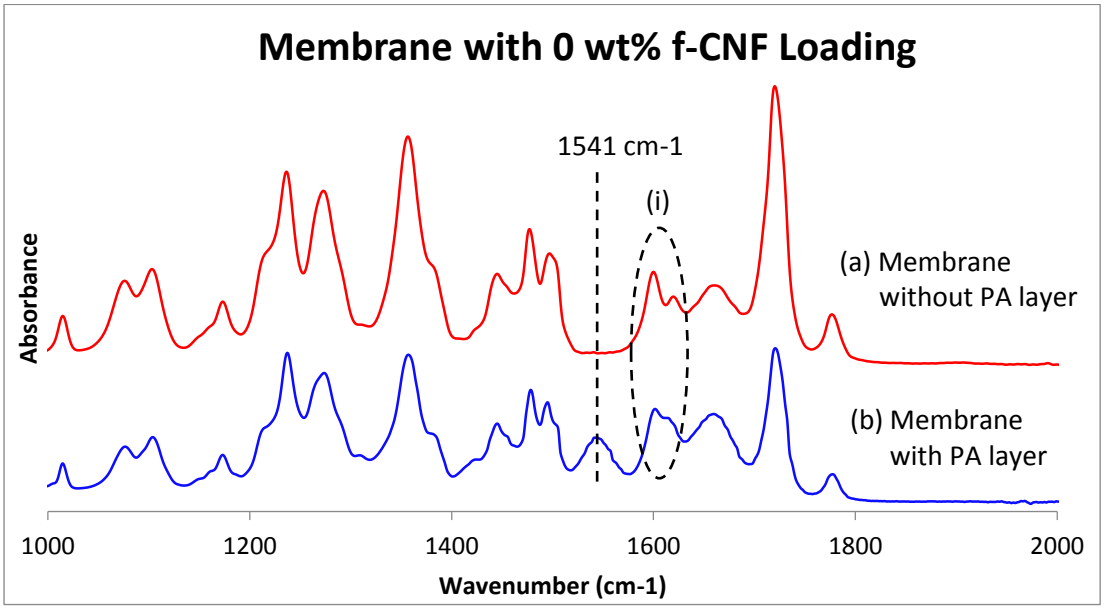

Figure 4.11: FTIR Spectrum of Membrane With 0.0 wt. % f-CNF Loading (a) Without and (b) With the PA Layer

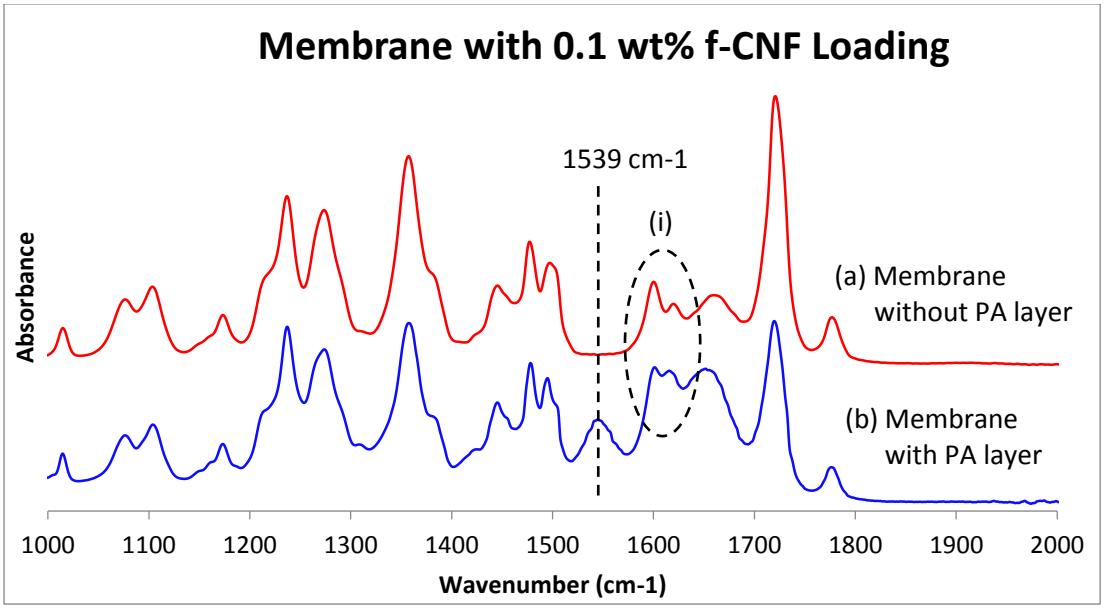

Figure 4.12: FTIR Spectrum of Membrane With 0.1 wt. % f-CNF Loading (a) Without and (b) With the PA Layer

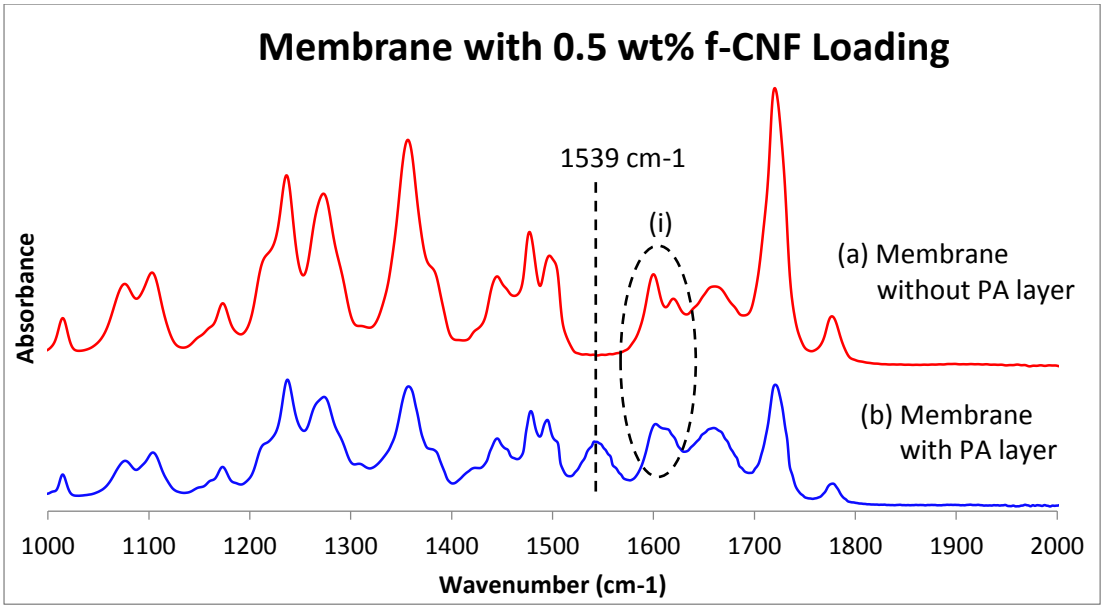

Figure 4.13: FTIR Spectrum of Membrane With 0.5 wt. % f-CNF Loading (a) Without and (b) With the PA Layer

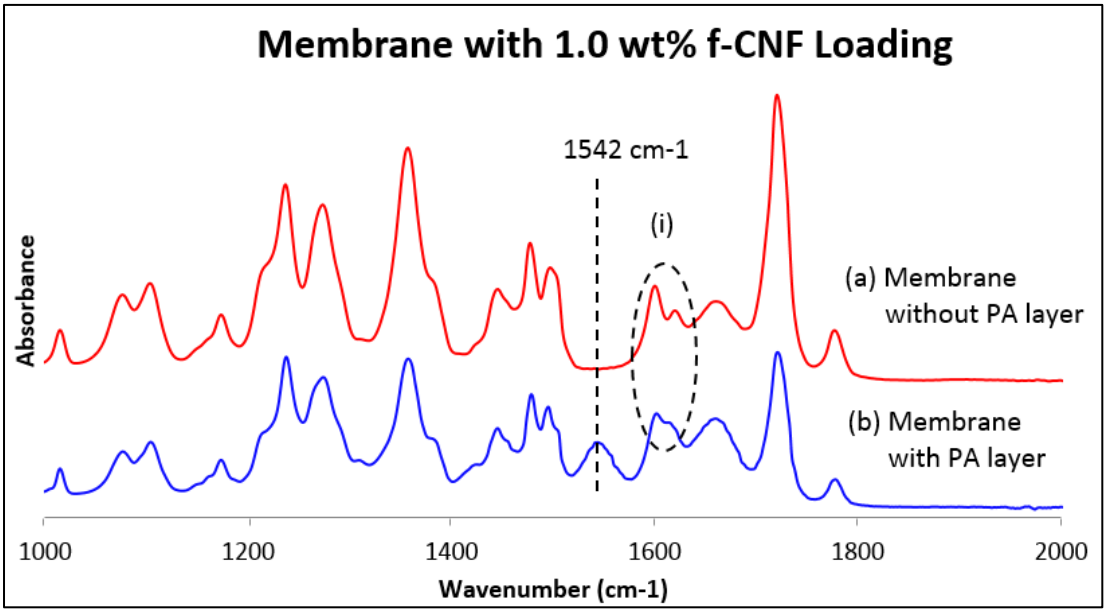

Figure 4.14: FTIR Spectrum of Membrane With 1.0 wt. % f-CNF Loading (a) Without and (b) With the PA Layer

4.2.3 Volume Porosity

The data obtained and the calculations that were made to find the volume porosity for each of the TFC membranes are as tabulated in Appendix A. Figure 4.15 tabulates the final overall volume porosity of the fabricated membranes of different f-CNF loadings; 0.0, 0.1, 0.5, and 1.0 wt. %.

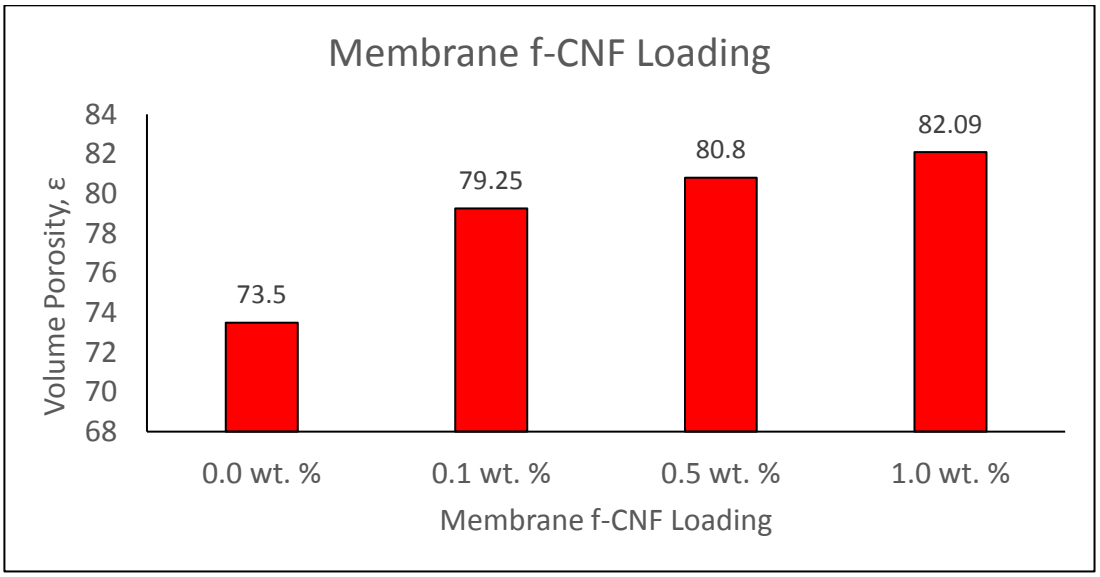

Figure 4.15: Overall Volume Porosity of Fabricated membranes

From Figure 4.15, the overall volume porosity for membranes of 0.0 wt. %, 0.1 wt. %, 0.5 wt. %, and 1.0 wt. % f-CNF loadings were 73.50, 79.25, 80.80 and 82.09, respectively. Membranes with 0.0 wt. % f-CNF loading has already shown a high porosity value of 73.50. This is due to the added PVP as a pore forming agent into all the membranes. PVP advocated many pores on the membrane surface which enables it to trap water molecules at a higher rate.

However, even with the addition of a PVP, the volume porosity of the fabricated membranes still increased with increasing f-CNF loading. This phenomenon can be explained by the incorporation of increasing hydrophilic substances into the polymeric membrane mix. As proven earlier by FTIR spectra in Figure 4.2 as well as the elemental analysis method and data in Table 4.1, it was confirmed that f-CNF was successfully functionalized with oxygenated functional groups grafted into the surface of the fibers. The hydrophilic f-CNF incorporated into the membrane increases the hydrophilicity of the membrane and thus allowing water molecules to be entrapped within the pores of the membrane (Khalid, et al., 2015).

Although as many researches (Torres, et al., 2016; Khalid, et al., 2015) have proven that the porosity of the membrane tend decrease as the nanoparticle loading increases over an optimum value due to increase in agglomeration of f-CNF as well as increasing viscosity of dope solution, this phenomenon did not occur throughout this experiment. As concluded by Rahimi, et al. (2015), the trend of decreasing porosity may occur at a f-CNF loading higher that 1.0 wt. %. Also as proven by the SEM migrograph in Figure 4.9, there were no agglomeration of nanoparticles observed. In the case of this project, incorporating 1.0 wt.% f-CNF loading may still be in the range of optimum loading value.

4.2.4 Surface Hydrophilicity

Figure 4.16 summarizes the contact angles of membranes of varying f-CNF loadings obtained from the contact angle goniometer. According to the tabulated data, when the test was conducted on the membranes with PA layer attached, its contact angles were 66.9°, 57°, 56° and 40.4° for membranes with f-CNF loadings of 0.0 wt. %, 0.1 wt. %, 0.5 wt. % and 1.0 wt. %, respectively.

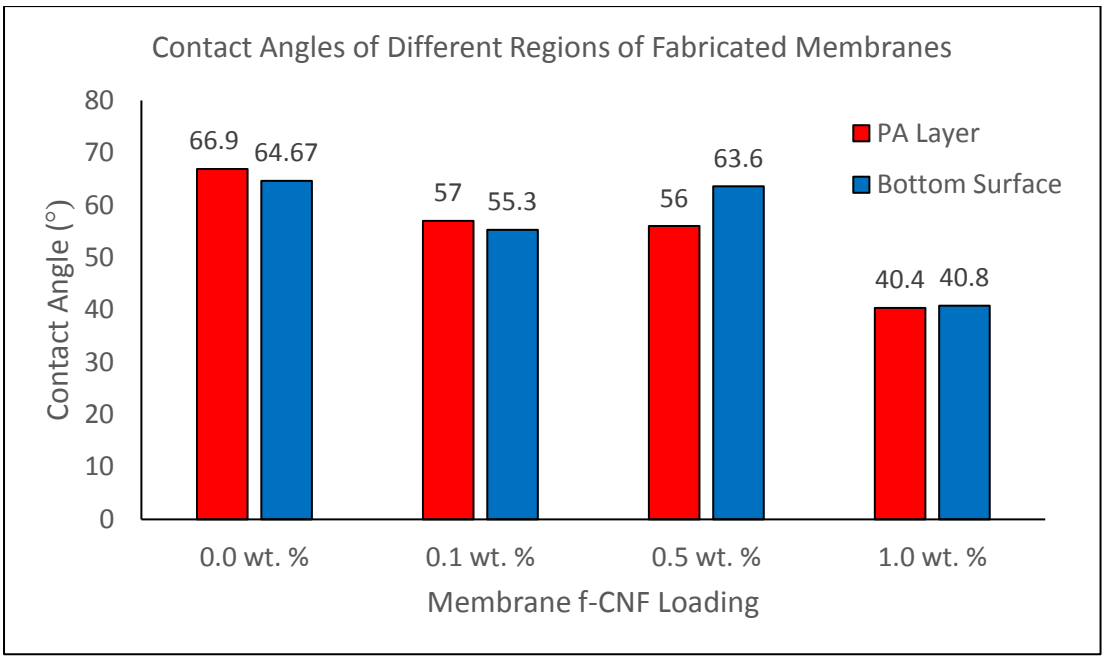

Figure 4.16: Contact Angles of Fabricated Membranes

The test conducted on the PA layer of fabricated membranes with no incorporation of nanoparticle into its matrix has the highest measured contact angle with a reading of 66.90°. The measured contact angles have a trend of decreasing values as the nanoparticle loading increases. This indicates a rise in hydrophilicity of the membrane as the loading increases due the water droplet seeping deeper into the membrane as oppose to remaining stagnant above the membrane.

This phenomenon can be explained by the hydrophilicity of the functionalized fibers themselves. Hydrophilic functional groups such as COOH group attached to the fiber surface due to the previous acid-functionalization process causes the membrane matrix to automatically be more inviting to water molecules during the phase inversion process (Dabaghian & Rahimpour, 2015). As the f-CNF loading increases, the number of water-loving functional groups in the membrane matrix increases as well, making the fabricated membrane more hydrophilic and allowing the water droplet to seep deeper into the membrane, causing the contact angle to decrease (Tang, et al., 2009).

Aside from that, when the test was conducted on the bottom side of the membrane, a similar trend was also observed with 64.67°, 53.3°, 63.6° and 40.80° for

membranes with f-CNF loadings of 0.0 wt. %, 0.1 wt. %, 0.5 wt. % and 1.0 wt. %, respectively. This can be justified by the SEM micrograph as pictured earlier in Figure 4.8. The micrographs of the membranes exhibit an increase in number of pores and pore sizes with increasing f-CNF loading (Dabaghian & Rahimpour, 2015). This was due to the increase in phase inversion as the hydrophilic contents added into the membrane mix was increased, leading to an increase in pore formation (Tian, et al., 2013). The increased pores on the surface of the membrane allows for more contents of the water droplet to enter into the membrane, thus, leading to a lower contact angle.

However, there is a slight discrepancy in contact angle for the bottom surface of 0.5 wt. % f-CNF membrane. This could be due to the irregularities in pore sizes and pore distribution of the membrane sample (Tang, et al., 2009). Hence, causing its result to deviate out of trend.

Lastly, it can be observed that the set of contact angle test results for the PA layer is slightly higher than that of the bottom surface of the membrane. This confirms that the PA layer side is less hydrophilic and accepting to water molecules as compared to the bottom surface of the membrane which contains of many pores (Torres, et al., 2016).

4.3 Performance Study of Fabricated Membrane

This sub-chapter thoroughly describes the performance efficiency of the fabricated CNF-incorporated membrane when it was put through a forward osmosis as well as a pressure retarded osmosis setup. The parameters varied in the study were the CNF loading incorporated in the membrane as well as the concentration of the glycerol draw solution.

4.3.1 Forward Osmosis (FO)

Two parameters were analyzed in this study; f-CNF loading of the TFC membrane and the concentration of the glycerol draw solution. Through the experiment, the mass change of the DI water feed solution was recorded throughout 30 minutes of the run. The recorded mass change is then used to calculate the average overall water flux of the system for each fabricated membrane. The mass change data as well as water flux

calculations are as attached in Appendix B. The calculated water flux results responding to the change in f-CNF loading and glycerol concentration are illustrated in Figure 4.17 for ease of interpretation.

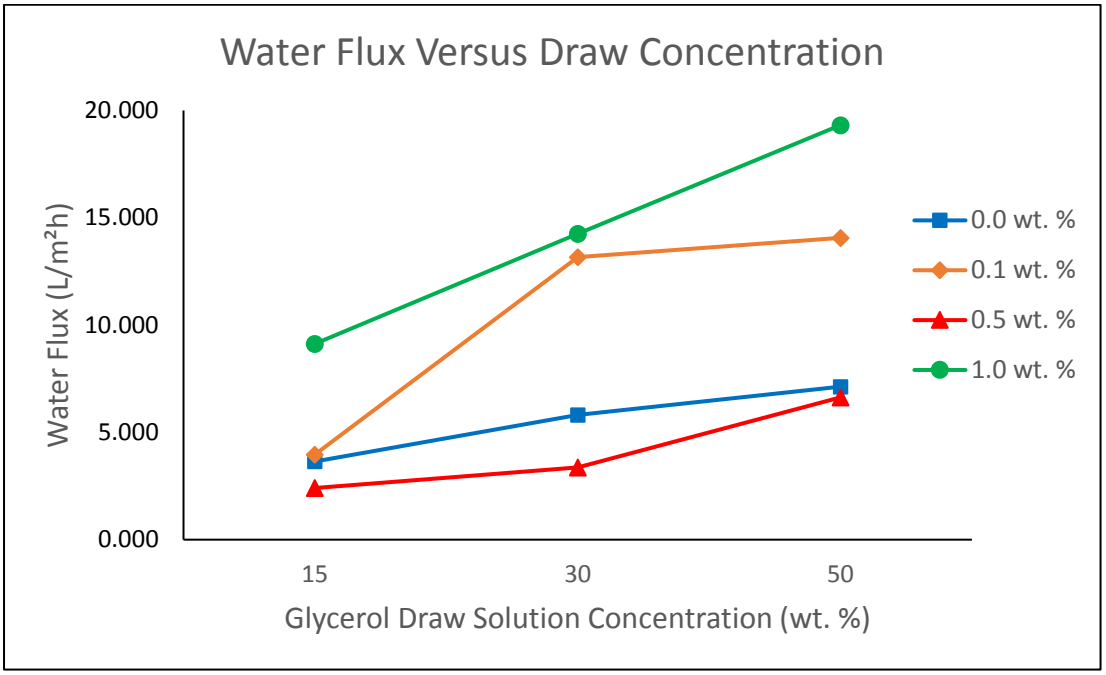

Figure 4.17: Resulting Water Flux of Forward Osmosis Process

From Figure 4.17, it can be observed that all four of the trend lines possess a common characteristic; the water flux increases as the concentration of the glycerol draw solution increases from 15 wt. % to 50 wt. %. This can be explained by the high osmotic pressure of glycerol (Sobczuk, et al., 2015) which is approximately 3.5 times greater than that of seawater. The highest water flux obtained was 19.317 L/m²h, from membrane of 1.0 wt.% f-CNF loading with 50 wt. % glycerol draw solution.

Through Figure 4.17, it can be concluded that regardless of the f-CNF loading on the membrane, as the concentration of glycerol draw solution increases, a larger osmotic gradient is created across the fabricated membrane causing the water molecules to permeate through the fabricated membrane and slowly migrate from the feed side to the draw side of the membrane.

As many researches such as Dabaghian and Rahimpour (2015) had concluded, the water flux will tend to increase as the nanoparticle loading increases. This statement

is valid until a certain optimum loading point whereby the water flux and performance will begin to decrease as agglomeration of the nanoparticle will tend to occur. However, this phenomenon did not occur accordingly in this study, deviating from literature. By analysing the water flux of the membrane at a constant glycerol concentration, 15 wt. %, membrane with 1.0 wt. % f-CNF loading possesses the highest flux at 9.127 L/m²h followed by 0.1 wt. % at 3.967 L/m²h, 0.0 wt. % at 3.643 L/m²h and finally 0.5 wt. % f-CNF at 2.406 L/m²h. The water flux increases in accending order from membrane with loading of 0.5, 0.0, 0.1 and 1.0 wt. %.

Out of the four different TFC membranes, the only membrane that was out of place was membrane with loading of 0.5 wt. % f-CNF. The water flux of this membrane was lower than it was expected to be. It was expected to have a water flux that was higher than 0.1 wt. % and lower than 1.0 wt. % membrane. This deviation in trend could be caused by dilutive ICP as elaborated earlier in Chapter 2. This phenomenon reduces the water flux of the membrane (McCutcheon & Elimelech, 2003). The water flux is reduced and slows down because the osmotic pressure on the draw side is lowered as the glycerol within the support layer is diluted by the permeating DI water (Zhao, et al., 2012).

Aside from that, the deviation in data could also be cause by the lack of support in the fabricated membranes of this project. Many researches such as Guan and Wang (2016) casted their membranes on a porous non-woven fabric support and managed to obtain a steady reading of increasing flux with increasing nanoparticle loading.

A similar water flux trend is observed for membranes with 0.0 wt. % and 0.1 wt. % f-CNF loading. It can be seen that the water flux only increased slightly when altering the draw solution concentration from 30 wt. % to 50 wt. % glycerol. This indicates that the membrane has reached the end of its sensitivity region as proven by Tian, et al. in 2013. This means that the water flux will not show any drastic increase in value even when the concentration of the glycerol draw solution is increased continuously.

With this peculiar trend in water flux, the glycerol concentration present in the DI water feed at the end of the experiment for all membranes were recorded and illustrated in Figure 4.18. Calculations for the glycerol concentrations were made based on the refractive indexes of the feed solution and are as tabulated in Appendix C. From the data in Figure 4.18, there were no trace of glycerol found in the feed side for membranes with a 15 wt. % glycerol draw solution. This indicates that the performance of these membranes showed no reverse solute flux.

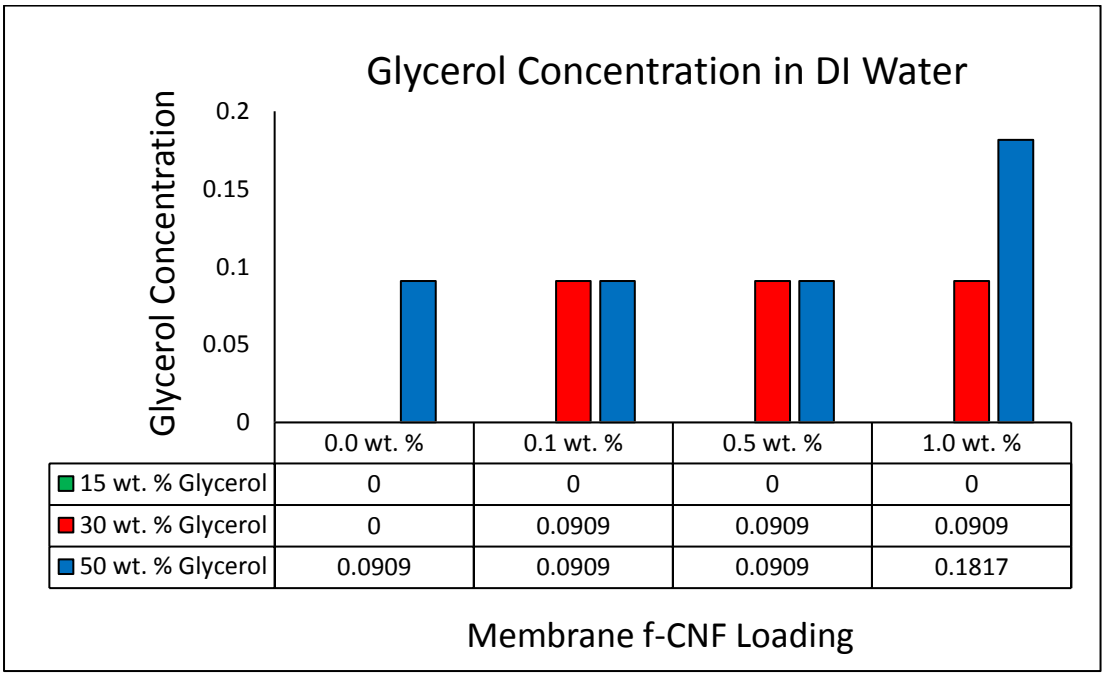

Figure 4.18: Measured Glycerol Concentration at DI Water Feed Solution

However, as for draw solution concentration of 30 wt. % and 50 wt. %, a slight increase in refractive index in DI water was observed. The increased refractive indexes confirmed a 0.0909 wt. % and 0.1817 wt. % of glycerol trace in the feed solution. This concludes a slight reverse solute flux present for these membranes. According to the tabulated data above, the reverse solute flux was the highest for membranes undergoing FO with a draw solution of 50 wt. % glycerol.

A common characteristic of the water and reverse solute flux is that the reverse flux of the membranes tend to increases as the water flux increases (Torres, et al., 2016). It is clear that the reverse solute flux was the highest when the water flux was also the highest for FO at a draw solution concentration of 50 wt. % glycerol. The reason to why

the water flux did not increase according to rising f-CNF loading in the membrane can be due to many experimental errors.

As highlighted by researcher Tang, et al. (2009), the PA rejection layer formed on top of the membrane surface plays a major role in the water as well as solute flux. Hence, one of the reasons of the deviation in results could be due to the uneven PA formation on the membrane surface during interfacial polymerization. This may cause certain regions of the membrane to be exposed to the glycerol draw solution without the PA barrier.

4.3.2 Pressure Retarded Osmosis (PRO)

Two of the fabricated TFC membranes were put under PRO testing in this study; membrane with 0.0 and 1.0 wt. % f-CNF loading. Each of the TFC membranes were tested with glycerol draw solution with concentration of 30 wt. % under two conditions; unpressurized and pressurized with 1 bar. The results obtained are as illustrated in the figures present in this subchapter. The water flux and refractive index sample calculations for PRO are alike to that of FO, attached in Appendix C.

PRO was conducted for both the stated TFC membranes with an unpressurised glycerol draw side, the data are as tabulated in Figure 4.19 below. Based on Figure 4.19, the PRO water flux for both membranes under an unpressurized draw solution exhibits fairly low and decreasing values. This is because as the DI water feed permeates across the membrane to the glycerol draw side, it slowly dilutes the draw solution. This reduces the osmotic gradient across the membrane and thus lowering the water flux as time passes (Alsvik & Hägg, 2013).

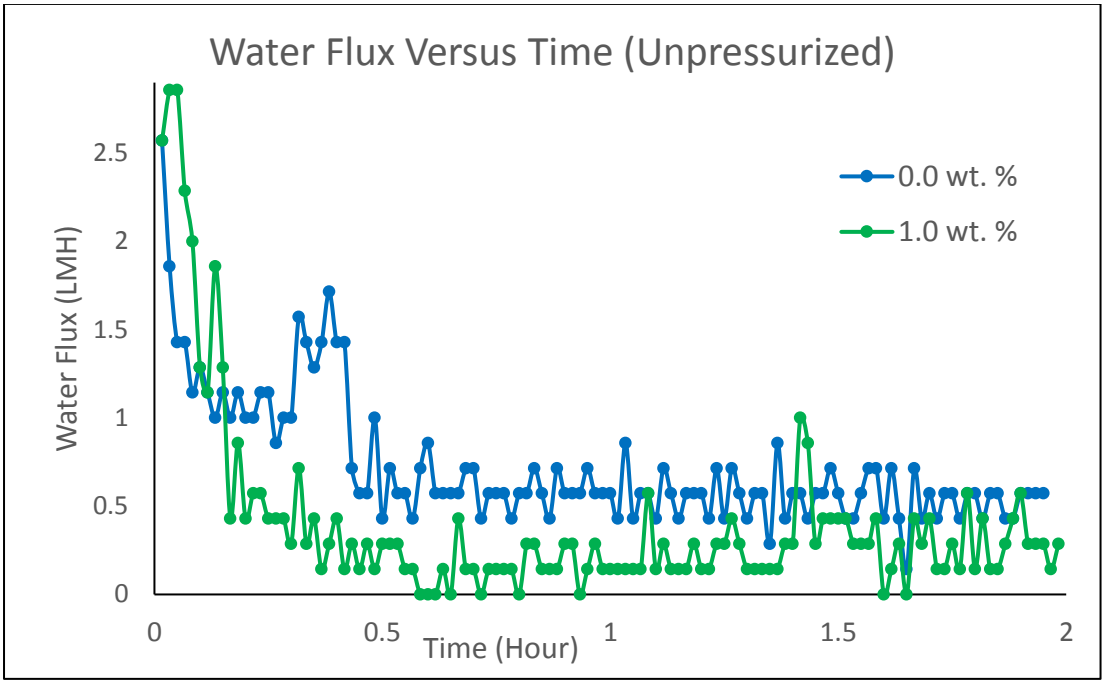

Figure 4.19: Water Flux for PRO with Unpressurized Glycerol Draw Solution

The water flux continually remains stagnant at an average rate of 0.56 L/m²h for TFC membrane with 0.0 wt. % f-CNF from the half until the second hour mark. According to Han, et al., (2013), as the feed permeates to the draw, pressure will begin to build up at the draw side of the TFC membrane. Although the water flux remained to be present for the next hour, however, no pressure reading was recorded on the pressure gauge in this review. This was because the pressure gauge that was used in the set up wasn't sensitive enough to lower pressure readings.

A similar trend was observed for TFC membrane with 1.0 wt. % f-CNF loading. Although there were slight increases in water flux after the half hour of the run, the water flux still managed to remain at a considerably stagnant of rate of 0.238 L/m²h until the end of the run. Alike to the previous, there was no build-up pressure reading observed on the gauge.

From Figure 4.19, it was also observed that the water flux trend for 1.0 wt. % f-CNF membrane is lower than that of 0.0 wt. % f-CNF membrane. This data pattern deviates from literatures as the water flux for nanoparticle-infused TFC membranes should acquire a higher water flux reading as compared to normal TFC due to its surface

being more porous and hydrophilic (Son, et al., 2016). To verify the validity of the deviation, the refractive indexes of the feed solution was recorded at the end of both PRO runs.

The resulting refractive indexes of the feed solution was 1.3332 for both membranes. This further confirms that there was no glycerol trace in the feed solution even after 2 hours, this concludes that there was no reverse solute flux in the system. This proves the validity of the obtained PRO data and justifies that the mechanical strength of 0.0 wt. % f-CNF TFC membrane is higher.

According to literature, a higher water flux for PRO systems will tend to generate a higher pressure reading (Son, et al., 2016). By analytical comparison, since the overall water flux was higher for TFC membrane with 0.0 wt. % f-CNF loading, it should generate a higher pressure compared to TFC membrane with 1.0 wt. % f-CNF loading, producing a higher power density.

With the continuous water flux reading even after 2 hours, it shows that there was a pressure was generated at the draw side of the membrane. After the 2-hour PRO run, a total of 6.08 g and 3.31 g of DI water had successfully permeated across to the draw side for 0.0 wt. % and 1.0 wt. % f-CNF TFC membrane, respectively. Since the generated pressure wasn’t high enough to be picked up by the pressure gauge, another PRO run was conducted for both of the fabricated membranes with the draw side pressurized with 1 bar. The data obtained are as illustrated in Figure 4.20 and 4.21.

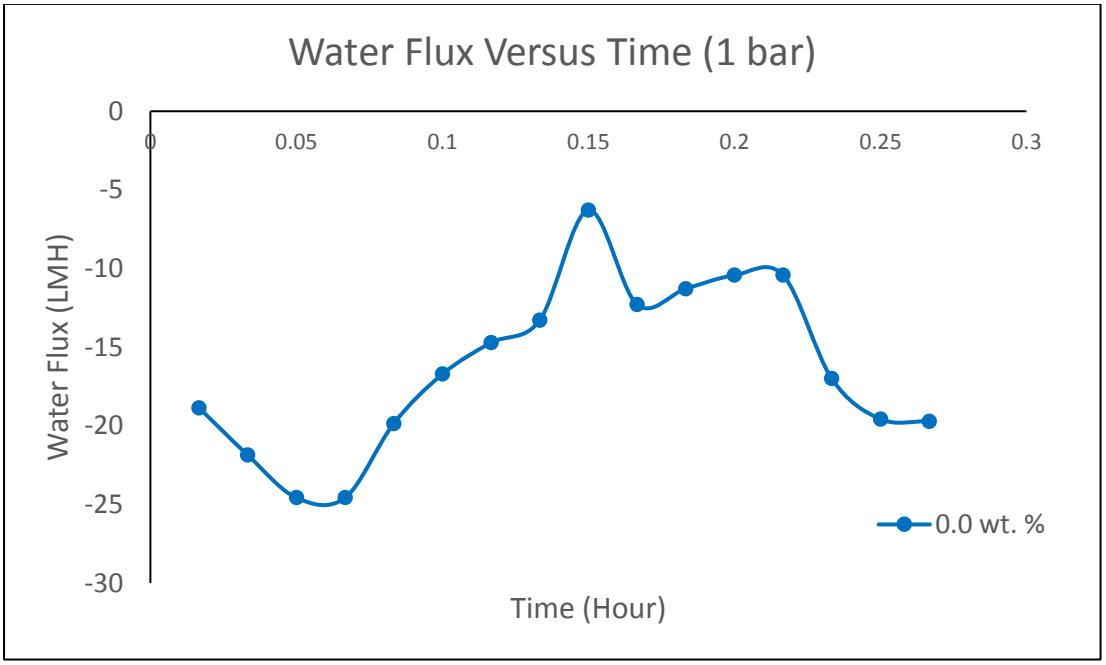

Figure 4.20: Water Flux for PRO at 1 Bar for Membrane with 0.0 wt.% f-CNF Loading

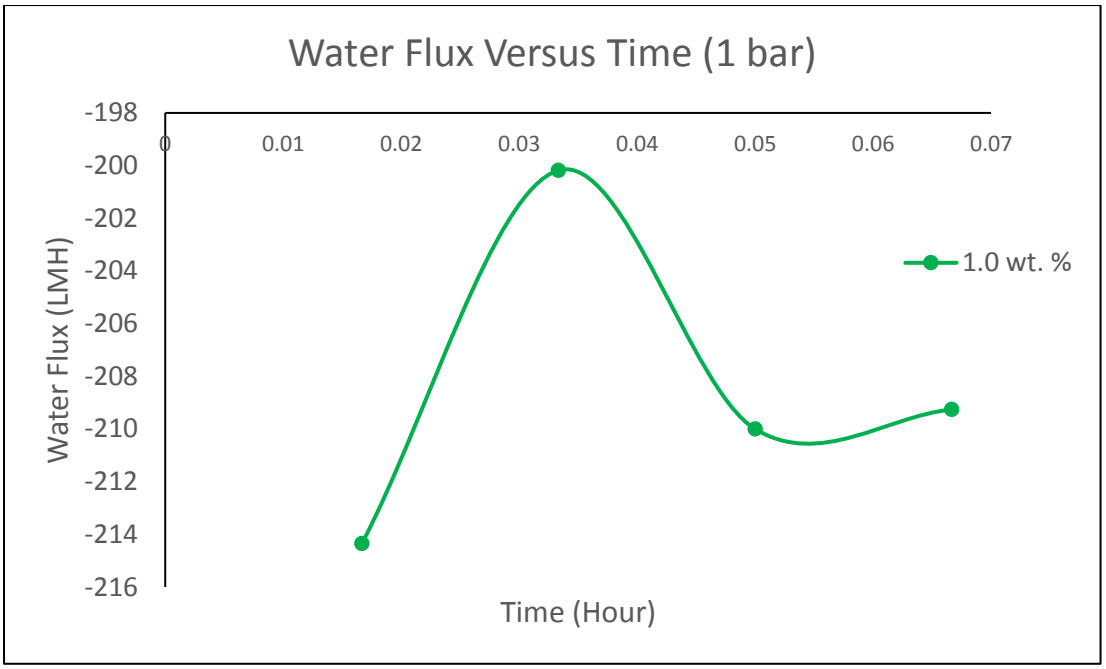

Figure 4.21: Water Flux for PRO at 1 Bar for Membrane with 1.0 wt.% f-CNF Loading

Based on Figure 4.20 and 4.21, the water flux of the PRO system exhibits negative values throughout the experiment. The average water flux for 0.0 and 1.0 wt.% f-CNF membranes are -16.34 L/m²h and -208.45 L/m²h, respectively. This data pattern

concludes that the DI water feed did not permeate across the membrane but instead, the glycerol draw solution began to migrate to the feed side. The reasoning to this phenomenon was due to the pressurized draw side of the membrane causing a higher force on the glycerol molecules to be transported across the membrane to the feed side (Han, et al., 2015). Alike to the unpressurized PRO system that was earlier conducted, there were no increase in pressure at the pressure gauge. However, the reading on the pressure gauge remained stagnant at 1 bar.

To further confirm that the glycerol had slowly permeated across to the feed side of the membrane, the refractive index of the DI water was recorded at different intervals. The refractive indexes were recorded and the glycerol concentration on the feed side were calculated to further confirm this statement, illustrated in Figure 4.22.

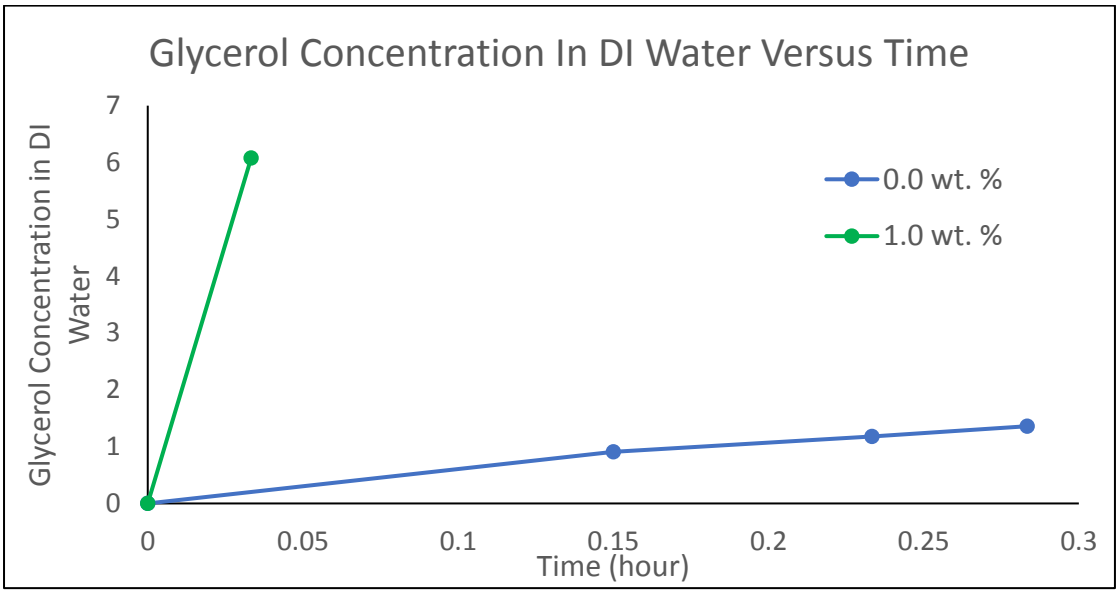

Figure 4.22: Glycerol Concentration in DI Water Over Time

The refractive indexes obtained for PRO with a 1 bar pressurized draw solution exhibits large traces of glycerol present in the feed solution for both TFC membranes. Based on Figure 4.22, a reverse solute flux in the system was confirmed based on the increase in refractive index and glycerol concentration of the DI water feed after both runs. Aside from that, it also shows that the glycerol concentration increases as time passes, this shows that the glycerol draw solution is permeating the membrane at an increasing rate.

The glycerol permeation rate was higher for TFC membrane with 1.0 wt. % as compared to 0.0 wt. % f-CNF loading. This validates that TFC membrane with 0.0 wt. % f-CNF loading can retain a higher pressure compared to the latter. From the resulting water fluxes obtained for both TFC membranes, it can be concluded that neither of the tested membranes could generate a power density under a PRO system with the draw solution pressurized at 1 bar.

Through this PRO study, under an unpressurized and a 1 bar glycerol draw solution, it can be concluded that the both tested TFC membranes performed efficiently at a pressure lower than 1 bar. This is because as the pressure of the draw solution is increased to 1 bar, the water molecules were unable to move across the membrane to the draw side anymore but instead, causing a massive reverse glycerol flux in the system. This concludes that both fabricated TFC membranes were not able to withstand a pressure of 1 bar.

However, it was not concluded that the fabricated TFC membranes were not eligible to withstand pressure lower than that. Unfortunately, due to the lack in sensitivity of the pressure gauge, the lowest pressure that could be pumped to the draw solution was 1 bar. Hence, due to that and the fact that membranes of 0.1 wt. % and 0.5 wt. % f-CNF loadings were not studied in this chapter, this research was not an exhaustive one.

On the other hand, at an unpressurized draw solution, both TFC membranes performed well in PRO mode. However, no pressure reading was observed on the pressure gauge due to its lack in sensitivity to lower pressures. It can be concluded that the membrane did managed to generate a slight amount of pressure on the draw side by analyzing the increasing water flux trend even after 2 hours. Unfortunately, due to the sensitivity of the pressure gauge, the power density of the PRO system was unable to be calculated and concluded.

Through the analytical method, it was concluded that membrane with 0.0 wt. % f-CNF loading generated a higher power density when compared to 1.0 wt. % loading. It can also withstand a higher-pressure due to its higher mechanical strength.

CHAPTER 5

CONCLUSION AND RECOMMENDATIONS

5.1 Conclusion

In this research, desired membranes as well as the effect of different loadings of f-CNF in membranes on FO and PRO processes have been studied comprehensively. Firstly, the functionalization of pristine CNF was deemed successful in grafting hydrophilic functional groups onto the fiber surfaces, awarding it with the ability to disperse much better in solvents.

Next, through the membrane characterization methods, it was also proven that the PA rejection layer was successfully formed on top of each of the membrane surfaces and its surface is less hydrophilic as compared to the bottom surface of the membrane. When the f-CNF loading in the membrane increases, the colour of the membrane darkens, the number of pores, volume porosity and the surface hydrophilicity of the membrane increases as well.

In the FO process, the water flux of each membrane increases as the glycerol draw solution increases due to its possession of higher osmotic pressure. The reverse glycerol flux is considered low and it is more significant in FO with 50 wt. % glycerol draw solution. The water flux resulting from membrane with 0.5 wt. % loading was slightly lower than expected, deviating from literature. Membrane with 1.0 wt. % f-CNF loading possesses the highest flux followed by 0.1, 0.0 and 0.5 wt. %.

Through analytical method, it was concluded that membrane with 0.0 wt. % f-CNF loading has a higher mechanical strength, can withstand a higher pressure and may generate a higher power density when compared to membrane with 1.0 wt. % f-CNF loading. The power density of the PRO system could not be calculated and concluded due to the lack in sensitivity of the pressure gauge used in the crossflow setup as no pressure reading could be recorded.

5.2 Recommendations

In this review study, the author has tried with utmost effort in fabricating and characterizing the TFC membranes with varying f-CNF loading as well as performing both FO and PRO performance testing on the fabricated TFC membranes. Since this study only covers the analysis of one type of nanoparticle as well as only one type of draw solution, this study is not an exhaustive one. Therefore, it would be highly recommended to conduct further studies on other additional nanoparticle and draw solutions available in the market which were not included in this review.

It was also concluded that there were many discrepancies in water flux values in the FO processes that could be cause by the inefficient PA layer formation on the fabricated membrane surface. It would be advised that more precise and clearer methodologies to be generate before the commencement of this study. Aside from that, since the PA layer formation is a very time dependent situation, it is highly recommended that all membranes undergo interfacial polymerization for the same duration of time to ensure an even coating, that includes the intermediate drying process as well.

Next, the power density of the PRO system could not be calculated and concluded due to the lack in sensitivity of the current pressure gauge in the crossflow setup. Thus, it is highly recommended that a pressure gauge of lower range sensitivity is used when conducting PRO experiments. Aside from that, the PRO study was not an exhaustive one as only TFC of 2 loadings were studies. Hence, TFC membranes with 0.1 and 0.5 wt. % f-CNF loading are advised to be included in the PRO study as well.

REFERENCES

Achilli, A., Cath, T. & Childress, A., 2010. Selection of inorganic based draw solutions for forward osmosis applications. *Journal of Membrane Science,* Volume 364, pp. 233-241.

Ahmed, D., Haider, A. & Mohammad, M., 2013. Comeparesion of Functionalization of Multi-Walled Carbon Nanotubes Treated by Oil Olive and Nitric Acid and Their Characterization. *Energy Procedia,* pp. 1111-1118.

Alger, M. S. M., 1996. *Polymer science dictionary.* 2nd ed. London: Chapman & Hall.

Alsvik, I. L. & Hägg, M. B., 2013. Pressure Retarded Osmosis and Forward Osmosis Membranes: Materials and Methods. *Polymers,* 21 March, Volume 5, pp. 303-327.

Arshad, S., Naraghi, M. & Chasiotis, I., 2011. Strong carbon nanofibers from electrospun polyacrylonitrile. *Carbon,* Volume 49, pp. 1710-1719.

Ayoub, M. & Abdullah, A. Z., 2011. Critical review on the current scenario and significance of crude glycerol resulting from biodiesel industry towards more sustainable renewable energy industry. *Renewable and Sustainable Energy Review,* 22 April, Volume 16, pp. 2671-2686.

Baker, R. W., 2012. *Membrane Technology and Applications.* 2rd ed. Newark: John Wiley and Sons Ltd.

Ball, P., 2015. Blue Energy: How mixing water can create electricity. *BBC*, 10 June.

Bortz, R. D., Merino, C. & Gullon, I. M., 2010. Carbon Nanofibers Enhance The Fracture Toughness And Fatigue Performance of a Structural Epoxy System. *Composite Science and Technology,* Volume 71, pp. 31-38.

Buang, N. A., Fabil, F., Majid, Z. A. & Shahir, S., 2012. Characteristics of Mild Acid Functionalized Multiwalled Carbon Nanotubes Towards High Dispersion With Low Structural Defects. *Journal of Nanomaterials and Biostructures,* Volume 7, pp. 33-39.

Bui, N.-N. & McCutcheon, J. R., 2014. Nanofiber Supported Thin-Film Composite Membrane for Pressure-Retarded Osmosis. *Environmental Science and Technology*, 48(7), pp. 4219-4136.

Carmignani, G., Sitkiewitz, S. & Webley, J. W., 2012. *Recovery of Retrograde Soluble Solute for Forward Osmosis Water Treatment.* s.l. Patent No. US 20120267308 A1.

Cath, T. Y., Childress, A. E. & Elimelech, M., 2005. Forward osmosis: Principles, applications, and recent developments. *Journal of Membrane Science,* Volume 281, pp. 70-87.

Cecava, M., Doane, P., Holzgraefe, D. & Pyatt, N., 2008. *Application of glycerin for improved livestock production.* Europe, Patent No. CA 2685055 A1.

Chatterjee, A. & Deopura, B., 2006. Thermal Stability of Polypropylene/Carbon Nanofiber Composite. *Journal of Applied Polymer Science,* Volume 100, pp. 3574-3578.

Choi, J., Jegal, J. & Kim, W., 2006. Fabrication and characterization of multi-walled carbon nanotubes/polymer blend membranes. *Journal of Membrane Science,* pp. 406-415.

Chou, S., Wang, R. & Fane, A., 2013. Robust and High performance hollow fiber membranes for energy harvesting from salinity gradients by pressure retarded osmosis. *Journal of Membrane Science,* pp. 44-54.

Chung, T. et al., 2012. Emerging Forward Osmosis (FO) Technologies and Challenges Ahead for Clean Water and Clean Energy Applications. *Current Opinion in Chemical Engineering.,* Volume 1, pp. 246-257.

Clark, D., 2013. *Salt Power: Norway Project Gives Osmotic Energy a Shake.* [Online] Available at: http://news.nationalgeographic.com/news/energy/2013/01/130107-osmotic-energy-norway [Accessed 18 February 2017].

Cui, Y., Liu, X. & Chung, T., 2014. Enhanced osmotic energy generation from salinity gradients by modifying thin film composite membranes. *Chemical Engineering Journal*, pp. 195-203.

Dabaghian, Z. & Rahimpour, A., 2015. Carboxylated carbon nanofibers as hydrophilic porous material to modification of cellulosic membranes for forward osmosis desalination. *Chemical Engineering Research and Design,* p. 647–657.

Emadzadeh, D. et al., 2013. Synthesis and characterization of thin film nanocomposite forward osmosis membrane with hydrophilic nanocomposite support to reduce internal concentration polarization. *Journal of Membrane Science,* Volume 449, pp. 74-85.

Endo, M. et al., 2001. Vapor-grown carbon fibers (VGCFs): Basic properties and their battery applications. *Carbon,* Volume 39, pp. 1287-1297.

Enerdata, 2015. *Global Energy Statistical Yearbook 2016.* [Online] Available at: https://yearbook.enerdata.net [Accessed 18 February 2017].

Favvas, E. et al., 2013. High purity multi-walled carbon nanotubes: Preparation, characterization and performance as filler materials in co-polyimide hollow fiber membranes. *Separation and Purification Technology,* pp. 262-269.

Feng , L., NingXie & Zhong, J., 2014. Carbon Nanofibers and Their Composites: A Review of Synthesizing, Properties and Applications. *Materials,* Volume 7, pp. 3020-3045.

Ge, Q., Ling, M. & Chung, T.-S., 2012. Draw solutions for forward osmosis processes: Developments, challenges, and prospects for the future. *Journal of Membrane Science,* Volume 442, pp. 225-237.

Glater, J., 1998. The early history of reverse osmosis membrane development. *Desalination,* September.pp. 297-309.

Goh, P., Ng, B., Ismail, A. & Hayashi, Y., 2012. Pre-treatment of multi-walled carbon nanotubes for polyetherimide mixed matrix hollow fiber membranes. *Journal of Colloid and Interface Science,* pp. 80-87.

Guan, P. & Wang, D., 2016. The improvement of CTA forward osmosis membrane performance by hydrophilic modification on interface between support layer and non-woven fabric. *Desalination and Water Treatment,* pp. 1944-3994.

Han, G., Wang, P. & Chung, T.-S., 2013. Highly Robust Thin-Film Composite Pressure Retarded Osmosis (PRO) Hollow Fiber Membranes with High Power Densities for Renewable Salinity-Gradient Energy Generation. *Environmental Science and Technology,* pp. 8070-8077.

Han, G., Zhang, S., Li, X. & Chung, T.-S., 2015. Progress in pressure retarded osmosis (PRO) membranes for osmotic power generation. *Pogress in Polymer Science,* Volume 51, pp. 1-27.

Helfer, F., Lemckert, C. & Anissimov, Y. G., 2013. Osmotic power with Pressure Retarded Osmosis: Theory, performance and trends - A review. *Journal of Membrane Science,* 1 November, Volume 453, pp. 337-358.

Ismail, A. et al., 2015. Thin film composite membrane — Recent development and future potential. *Desalination,* Volume 356, pp. 140-148.

Ismail, A. et al., 2015. Thin film composite membrane — Recent development and future potential. *Desalination,* Volume 356, pp. 140-148.

Jeong, B. et al., 2007. Interfacial polymerization of thin film nanocomposites: A new concept for reverse osmosis membranes. *Journal of Membrane Science,* 294(1-2), pp. 1-7.

Johnson, D. T. & Taconi, K. A., 2007. The Glycerin Glut: Options forthe Value-Added Conversion of Crude Glycerol Resulting from Biodiesel Production. *Environmental Progress,* 1 October, 26(4), pp. 338-348.

Jung, J. T. et al., 2016. Understanding the non-solvent induced phase separation (NIPS) effect during the fabrication of microporous PVDF membranes via thermally induced phase separation (TIPS). *Journal of Membrane Science,* Volume 514, pp. 250-263.

Kathryn, 2016. *http://www.carboncounted.co.uk/when-will-fossil-fuels-run-out.html*. Available at: http://www.carboncounted.co.uk/when-will-fossil-fuels-run-out.html [Accessed 18 February 2017].

Khalid, A. et al., 2015. Preparation and properties of nanocomposite polysulfone/multi-walled carbon nanotubes membranes for desalination. *Desalination,* Volume 367, pp. 134-144.

Khare, V., Greenberg, A. & Krantz, W., 2005. Vapor-induced phase separation - Effect of the humid air exposure step on membrane morphology: Part I. Insights from mathematical modeling.. *Journal of Membrane Science,* Volume 258, pp. 140-156.

Kiadehi, A. D., Rahimpour, A., Jahanshahi, M. & Ghoreyshi, A. A., 2014. Novel carbon nano-fibers (CNF)/polysulfone (PSf) mixed matrix membranes for gas separation. *Journal of Industrial and Engineering Chemistry,* Volume 22, p. 199–207.

Kim, E.-S., Hwang, G., El-Din, M. G. & Liu, Y., 2011. Development of nanosilver and multi-walled carbon nanotubes thin-film nanocomposite membrane for enhanced water treatment. *Journal of Membrane Science,* Volume 394-395, pp. 37-48.

Klein, K. et al., 2008. Surface characterization and functionalization of carbon nanofibers. *Journal of Applied Physics,* Volume 103.

Konios, D., Stylianakis, M., Stratakis, E. & Kymakis, E., 2014. Dispersion behaviour of graphene oxide and reduced graphene oxide. *Journal of Colloid and Interface Science,* Volume 430, pp. 108-112.

Lai, G. et al., 2016. A practical approach to synthesize polyamide thin film nanocomposite (TFN) membrane with improved separation properties for water/wastewater treatment. *Journal os Materials Chemistry A,* Volume 4, pp. 4134-4144.

Lalia, B. S., Kochkodan, V., Hashaikeh, R. & Hilal, N., 2013. A review on membrane fabrication: Structure, properties and performance relationship. *Desalination,* Volume 326, pp. 77-95.

Lau, W. et al., 2015. A review on polyamide thin film nanocomposite (TFN) membranes: History, applications, challenges and approaches. *Water Research,* Volume 80, pp. 306-324.

Lau, W., Ismail, A., Misdan, N. & Kassim, M., 2011. A recent progress in thin film composite membrane: A review. *Desalination,* Volume 287, pp. 190-199.

Lind, M. et al., 2009. Influence of zeolite crystal size on zeolite-polyamide thin film nanocomposite membranes. *Langmuir 25,* Volume 25, p. 10139–10145.

Ling, M., Wang, K. & Chung, T., 2010. Highly water-soluble magnetic nanoparticles as novel draw solutes in forward osmosis for water reuse. *Ind. Eng. Chem. Res,* Volume 49, p. 5869–5876.

Liu, S. X. & Kim, J.-T., 2011. Characterization of surface modification of polyethersulfone membrane. *Journal of Adhesion Science and Technology,* 25(1-3), pp. 193-212.

Lutchmiah, K. et al., 2014. Forward osmosis for application in wastewater treatment - A review. *Water Research,* 4 April, Volume 58, pp. 179-197.

Madiwale, S. & Bhojwani, V., 2016. An Overview on Production, Properties, Performance and Emission Analysis of blends of Biodiesel. *Global Colloquium in Recent Advancement and Effectual Researches in Engineering, Science and Technology*, Volume 25, pp. 963-973.

Mah, S.-K., Chang, C. C. H., Wu, T. Y. & Chai, S.-P., 2014. The study of reverse osmosis on glycerin solution filtration: Dead-end and crossflow filtrations, transport mechanism, rejection and permeability investigations. *Desalination,* Volume 352, pp. 66-81.

Mallakpour, S. & Zadehnazari, A., 2013. Effect of amino acid-functionalization on the interfacial adhesion and behavior of multi-walled carbon nanotubes/poly (amide-imide) nanocomposites containing thiazole side unit. *Journal of Polymer Research,* Volume 20, pp. 192-204.

McCutcheon, J. R. & Elimelech, M., 2003. Influence of concentrative and dilutive internal concentration polarization on flux behavior in forword osmosis. *Journal of Membrane Science,* Volume 284, pp. 237-247.

National Renewable Energy Laboratory (NREL), 2005. *Biodiesel–Clean, Green Diesel Fuel,* Colorado: U.S. Department of Energy (DOE).

Nguyen Van, T. D., Sufian , S., Mansor, N. & Yahya, N., 2014. Characterization of Carbon Nanofibers Treated with Thermal Nitrogen as a Catalyst Support Using Point-of-Zero Charge Analysis. *Journal of Nanomaterials.*

Ozkan, T., Naraghi, M. & Chasiotis, I., 2010. Mechanical properties of vapor grown carbon nanofibers. *Carbon,* 48(1), pp. 239-244.

Phuntsho, S. et al., 2011. A novel low energy fertilizer driven forward osmosis desalination for direct fertigation: Evaluating the performance of fertilizer draw solutions. *Journal of Membrane Science,* 375(1-2), pp. 172-181.

Poveda, R. & Gupta, N., 2016. *Carbon Nanofiber Reinforced Polymer Composites.* 1st ed. s.l.:SpringerBriefs in Materials.

Powalowska, D. S., 2014. The effect of high concentrations of glycerol on the growth, metabolism and adaptation capacity of Clostridium butyricum DSP1. *Electronic Journal of Biotechnology,* 18(2), pp. 128-133.

Qiu, C. et al., 2012. High performance flat sheet forward osmosis membrane with an NF-like selective layer on a woven fabric embedded substrate. *Desalination,* Volume 287, pp. 266-270.

Rahimi, Z., Zinatizadeh, A. & Zinadini, S., 2015. Preparation of high antibiofouling amino functionalized MWCNTs/PES nanocomposite ultrafiltration membrane for application in membrane bioreactor. *Journal of Industrial and Engineering Chemistry,* Volume 29, pp. 366-374.

Rana, S., Alagirusamy, R., Fangueiro, R. & Joshi, M., 2012. Effect of Carbon Nanofiber Functionalization on the In-Plane Mechanical Properties of Carbon/Epoxy Multiscale Composites. *Journal of Applied Polymer Science,* Volume 125, pp. 1951-1958.

Ren, J., O'Grady, B., deJesus, G. & McCutcheon, J., 2016. Sulfonated polysulfone supported high performance thin film composite membranes for forward osmosis. *Polymer,* Volume 103, pp. 486-497.

Roser, M. & Ospina, E. O., 2017. *World Population Growth.* [Online] Available at: https://ourworldindata.org/world-population-growth/#empirical-view [Accessed 18 February 2017].

Sebastian, D., Suelves, I., Moliner, R. & Lazaro, M., 2010. The effect of the functionalization of carbon nanofibers on their electronic conductivity. *Carbon,* 48(15), pp. 4421-4431.

Setiawan, L., Wang, R., Li, K. & Fane, A., 2011. Fabrication of novel poly(amide–imide) forward osmosis hollow fiber membranes with a positively charged nanofiltration-like selective layer. *Journal of Membrane Science,* 369(1-2), pp. 196-205.

Sharif, A. O. et al., 2011. The potential of chemical-osmotic energy for renewable power generation. *Marine and Ocean Technology (MO),* 13 May.pp. 2190-2197.

Shepl, Y. A. et al., 2014. Performance enhancement of TFC RO membrane by using magnesium silicate nanoparticles. *Journal of Membrane Science.*

Sobczuk, T. M., Gonzalez, M. I., Grima, E. M. & Chisti, Y., 2015. Forward osmosis with waste glycerol for concentrating microalgae slurries. *Algal Research,* Volume 8, pp. 168-173.

Son, M. et al., 2016. Thin-film nanocomposite membrane with CNT positioning in support layer for energy harvesting from saline water. *Chemical Engineering Journal,* Volume 284, pp. 68-77.

Tang, C. Y., Kwon, Y.-N. & Leckie, J. O., 2009. Effect of membrane chemistry and coating layer on physiochemical properties of thin film composite polyamide RO and NF membranes I. FTIR and XPS characterization of polyamide and coating layer chemistry. *Desalination,* Volume 242, pp. 149-167.

Tan, H., Aziz, A. A. & Aroua, M., 2013. Glycerol production and its applications as a raw material: A review. *Renewable and Sustainable Energy Reviews,* 10 July, Volume 27, pp. 118-127.

Terry, R., Baker, K. & Rodriguez, N. M., 2009. *Conductive polymeric structures containing graphite nanofibers having graphite parallel to the growth axis.* s.l. Patent No. US 7592389 B2.

THASS - Thermal Analysis & Surface Science GmbH, 2010. *Buoyancy Phenomenon in TGA Systems.* Friedberg: Thermo Electron Corporation.

Tian, M. et al., 2013. Preparation of polyamide thin film composite forward osmosis membranes using electrospun polyvinylidene fluoride (PVDF) nanofibers as substrates. *Separation and Purification Technology,* Volume 118, pp. 727-736.

Torres, S. M., Esteves, C. M., Figueiredo, J. L. & Silva, A. M., 2016. Thin-film composite forward osmosis membranes based on polysulfone supports blended with nanostructured carbon materials. *Journal of Membrane Science,* Volume 520, pp. 326-336.

Touati, K., Tadeo, F. & Schiestel, T., 2014. Impact of Temperature on Power Recovery in Osmotic Power Production by Pressure Retarded Osmosis. *Energy Procedia,* Volume 50, pp. 960-969.

U.S Energy Information Administration, 2017. *Monthly Biodiesel Production Report,* Washington: U.S Department of Energy.

U.S. Energy Information Administration, 2017. Monthly Energy Review. January, p. 242.

U.S. Geological Survey, 2017. *USGS - Water Resources of the United States.* [Online] Available at: https://www2.usgs.gov/water [Accessed 25 February 2017].

Valerio, O. et al., 2015. Improved utilization of crude glycerol from biodiesel industries: Synthesis and characterization of sustainable biobased polyesters. *Industrial Crops and Products,* 16 November, Volume 78, pp. 141-147.

Vatapour, V. et al., 2011. Fabrication and characterization of novel antifouling nanofiltration membrane prepared from oxidized multiwalled carbon nanotube/polyethersulfone nanocomposite. *Journal of Membrane Science,* 375(1-2), pp. 284-294.

Wong, D., 2013. *The Real Price We Pay for Fossil Fuel Energy.* [Online] Available at: http://www.carbon49.com/2013/04/the-real-price-we-pay-for-fossil-fuel-energy [Accessed 18 February 2017].

Yin, J. & Deng, B., 2014. Polymer-matrix nanocomposite membranes for water treatment. *Journal of Membrane Science,* Volume 479, pp. 256-275.

Zhao, S., Zou, L., Tang, C. Y. & Mulcahy, D., 2012. Recent developments in forward osmosis: Opportunities and challenges. *Journal of Membrane Science,* 21 January, Volume 396, pp. 1-21.

Zhou, Z. et al., 2010. Graphitic carbon nanofibers developed from bundles of aligned electrospun polyacrylonitrile nanofibers containing phosphoric acid.. *Polymer,* 51(11), pp. 2360-2367.

APPENDICES

Appendix A: Calculation for The Volume Porosity of Fabricated TFC Membranes

The data obtained and recorded during the porosity testing of fabricated membranes were tabulated below in terms of bone-dried weight, wetted weight and weight change. The following results were tabulated for the controlled membrane as well as membranes with f-CNF loadings of 0.1 wt. %, 0.5 wt. % and 1.0 wt. %. The porosity was calculated based on Equation 3.1 with $\rho_{water} = 1.00\ g/cm^3$ and$\rho_p = 1.27\ g/cm^3$.

Sample calculation:

For membrane with 0.1 wt. % f-CNF loading, sample 1:

$$\text{Volume Porosity, } \varepsilon = \frac{\frac{m_{wet} - m_{dry}}{\rho_{water}}}{\frac{m_{wet} - m_{dry}}{\rho_{water}} + \frac{m_{dry}}{\rho_p}} \times 100$$

$$= \frac{\frac{0.043\ g - 0.011\ g}{1.00\ g/cm^3}}{\frac{0.043\ g - 0.011\ g}{1.00\ g/cm^3} + \frac{0.011\ g}{1.27\ g/cm^3}} \times 100$$

$$= 78.70$$

Table 1: Volume Porosity of Membrane with 0.0 wt. % f-CNF Loading

Membrane with 0.0 wt. % f-CNF loading	Weight of dried membrane, g	Weight of soaked membrane, g	Volume Porosity, ε
Sample 1	0.0127	0.0426	74.92
Sample 2	0.0135	0.0413	72.36
Sample 3	0.0139	0.0438	73.18
Sample 4	0.0136	0.0433	73.52
Average Porosity			73.50

Table 2: Volume Porosity of Membrane with 0.1 wt. % f-CNF Loading

Membrane with 0.1 wt. % f-CNF loading	Weight of dried membrane, g	Weight of soaked membrane, g	Volume Porosity, ε
Sample 1	0.011	0.043	78.70
Sample 2	0.0107	0.0437	79.66
Sample 3	0.0101	0.0397	78.82
Sample 4	0.0097	0.0399	79.81
Average Porosity			79.25

Table 3: Volume Porosity of Membrane with 0.5 wt. % f-CNF Loading

Membrane with 0.5 wt. % f-CNF loading	Weight of dried membrane, g	Weight of soaked membrane, g	Volume Porosity, ε
Sample 1	0.0108	0.0466	80.81
Sample 2	0.0105	0.0439	80.16
Sample 3	0.0116	0.052	81.56
Sample 4	0.0115	0.0493	80.67
Average Porosity			80.80

Table 4: Volume Porosity of Membrane with 1.0 wt. % f-CNF Loading

Membrane with 1.0 wt. % f-CNF loading	Weight of dried membrane, g	Weight of soaked membrane, g	Volume Porosity, ε
Sample 1	0.0155	0.071	81.97
Sample 2	0.0122	0.0566	82.21
Sample 3	0.0126	0.057	81.74
Sample 4	0.0121	0.0568	82.43
Average Porosity			82.09

Appendix B: Calculation for The Water Flux of Fabricated TFC Membranes for FO

The data obtained and recorded during the performance testing of fabricated membranes were tabulated below in terms of the average DI water feed mass change. The following results were obtained by varying two parameters; using membrane with different f-CNF loadings and preparing glycerol draw solution of different concentrations. The water flux was calculated based on Equation 3.2 with $\rho_{water} = 1000\ g/L$, $A_m = 42\ \text{cm}^2$ and $\Delta t = 30$ minutes.

Sample calculation:

For membrane with 0.1 wt.% f-CNF loading and 15 wt. % glycerol draw solution:

$$\text{Water flux, } J_w = \frac{\Delta m}{\rho A_m \Delta t}$$

$$= \frac{0.27743\ \text{g}}{\left(1000\ \frac{\text{g}}{\text{L}}\right)(42\ \text{cm}^2)(30\ \text{min})\left(\frac{1\ \text{h}}{60\ \text{min}}\right)\left(\frac{1\ \text{m}^2}{10000\ \text{cm}^2}\right)}$$

$$= 0.1321\ \text{L/m}^2\text{h}$$

Table 1: Average Mass Change Raw Data for FO

F-CNF Loading	Average Mass Change, Δm (g)		
	15 wt. % Glycerol	30 wt. % Glycerol	50 wt. % Glycerol
0.0 wt. %	0.81875	2.2370	2.46840
0.1 wt. %	0.27743	0.9220	0.98453
0.5 wt. %	0.16844	0.2361	0.46412
1.0 wt. %	0.63889	0.9978	1.35220

Table 2: Calculated Water Flux for FO

F-CNF Loading	Water Flux, J_w ($\text{L m}^2\text{h}^{-1}$)		
	15 wt. % Glycerol	30 wt. % Glycerol	50 wt. % Glycerol
0.0 wt. %	0.3899	1.0652	1.1754
0.1 wt. %	0.1321	0.4390	0.4688
0.5 wt. %	0.0802	0.1124	0.2210
1.0 wt. %	0.3042	0.4751	0.6439

Appendix C: Calculation for The Glycerol Concentration in DI Water For FO

The refractive index obtained and recorded during the performance testing of fabricated membranes were tabulated in Table 1. The following results were obtained by measuring the refractive index of the DI water feed after each FO run with varying membrane and glycerol concentration. The glycerol concentration at the DI water feed side at the end of each run is calculated based on the glycerol calibration curve obtained from Mah, et al., (2014).

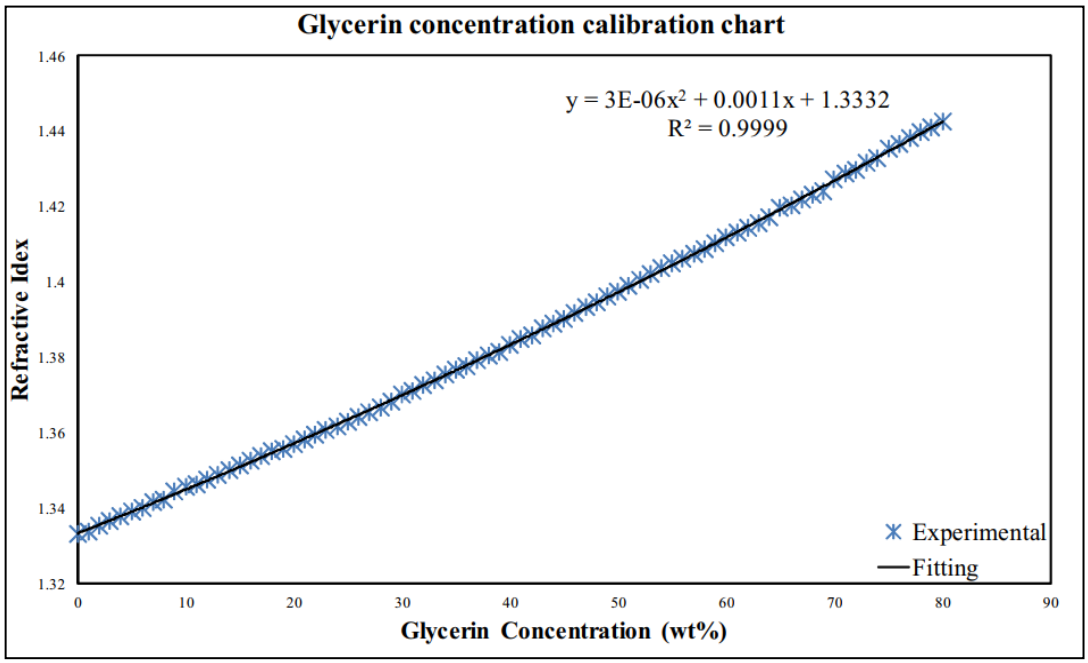

Figure 1: Glycerol Calibration Curve (Mah, et al., 2014)

Sample calculation:

For membrane with 0.1 wt.% f-CNF loading and 30 wt. % glycerol draw solution:

Concentration of glycerol at refractive index of 1.3333, the straight-line equation obtained from the calibration curve above is

$y = (3 \times 10^{-6})x^2 + 0.0011x + 1.3332$

$1.3333 = (3 \times 10^{-6})x^2 + 0.0011x + 1.3332$

$x = 0.0909$ wt. % Glycerol

Hence, at the end of the FO run, 0.0909 wt. % of glycerol was found to have transported itself from the draw side to the feed side.

Table 1: Refractive Index Recorded at The End of Each Run for FO

F-CNF Loading	Refractive Index of DI Water Feed Solution		
	15 wt. % Glycerol	30 wt. % Glycerol	50 wt. % Glycerol
0.0 wt. %	1.3332	1.3332	1.3333
0.1 wt. %	1.3332	1.3333	1.3333
0.5 wt. %	1.3332	1.3333	1.3333
1.0 wt. %	1.3332	1.3333	1.3334

Table 2: Glycerol Concentration of Feed at The End of Each Run for FO

F-CNF Loading	Glycerol Concentration of DI Water Feed Solution (wt. %)		
	15 wt. % Glycerol	30 wt. % Glycerol	50 wt. % Glycerol
0.0 wt. %	0	0	0.0909
0.1 wt. %	0	0.0909	0.0909
0.5 wt. %	0	0.0909	0.0909
1.0 wt. %	0	0.0909	0.1817